

MICRO AND NANOTEXTURED POLYMER FIBERS FOR OPEN MICROFLUIDICS

A THESIS SUBMITTED TO
THE GRADUATE SCHOOL OF ENGINEERING AND SCIENCE
OF BILKENT UNIVERSITY
IN PARTIAL FULFILLMENT OF THE REQUIREMENTS
FOR THE DEGREE OF
MASTER OF SCIENCE
IN
MATERIALS SCIENCE AND NANOTECHNOLOGY

By
Muhammad Yunusa
January, 2016

MICRO AND NANOTEXTURED POLYMER FIBERS
FOR OPEN MICROFLUIDICS

By Muhammad Yunusa

January, 2016

We certify that we have read this thesis and that in our opinion it is fully adequate,
in scope and in quality, as a dissertation for the degree of Master of Science.

Mehmet Bayındır (Advisor)

Çağlar Elbüken

Hatice Duran

Approved for the Graduate School of Engineering and Science:

Levent Onural

Director of the Graduate School

ABSTRACT

MICRO AND NANOTEXTURED POLYMER FIBERS FOR OPEN MICROFLUIDICS

Muhammad Yunusa

M.S. in Materials Science and Nanotechnology

Supervisor: Mehmet Bayındır

January, 2016

Microfluidics is the science of controlling low volumes of fluids in a microchannel. It is used in diverse area of applications such as chemical and biological analysis. Benefits of microfluidics are fast analysis, short reaction times, and portability of device. Current fabrication techniques of lab-on-a-chip microfluidic devices are soft lithography and micromachining. However, these methods suffer from design limitations such as flexibility of product, high cost, integration of external components, and biocompatibility.

Surface textured polymer fibers are utilized as a novel platform for the fabrication of affordable microfluidic devices. Fibers are produced by thermal drawing technique tens of meters-long at a time and comprise twenty continuous and ordered V-grooves channels on their surfaces. Extreme anisotropic wetting behavior due to capillary action along the grooves of fibers is observed after surface modifications with polydopamine (PDA) coating and Ultraviolet/Ozone (UV/O) treatment. Three-dimensional arrays of flexible fibers spontaneously spread liquid on predefined paths without the need of external pumps or actuators. In addition, surface modification with organically modified silica nanoparticles was added on top of the V-grooves to enhance the hydrophobicity of the fiber surfaces. Surface textured fibers are well suited for the fabrication of flexible, robust, lightweight and affordable microfluidic devices which is believed to expand the role of microfluidics in a scope of fields including drug discovery, medical diagnostics and monitoring food and water quality.

Keywords: Microfluidics, Anisotropic wetting, Polymer fiber drawing, Capillary flow, Colorimetric protein assay.

ÖZET

MİKRO VE NANOYAPILI FİBER TABANLI AÇIK MİKROAKIŞKANLAR

Muhammad Yunusa

Malzeme Bilimi ve Nanoteknoloji Yüksek Lisans Tezi

Danışman: Mehmet Bayındır

Ocak, 2016

Mikroakışkanlar, çok küçük hacimlere sahip sıvıları, mikrometrelik kanallarda kontrol etme bilimidir. Mikroakışkanlar, kısa tepkime süresi ile çabuk analiz edilebilme ve taşınabilir özellikleriyle başlıca kimyasal ve biyolojik analizler olmak üzere daha birçok alanda teknolojik olarak uygulama bulmaktadır. Günümüzde mikroakışkan temelli cihazlar, litografi ve mikro-imalat gibi yöntemler ile cip üstü laboratuvar aygıtları olarak üretilmektedir. Ancak söz konusu üretim teknikleri, esneklik, biyolojik uyum, harici bileşenlerle bütünleşme ve üretim maliyetleri gibi yüksek önem arz eden konularda kısıtlamalara sahiptirler.

Bu çalışmada, yüzeyi şekillendirilmiş polimer fiberler, ekonomik açıdan uygun mikroakışkan cihazların üretimi için yeni bir platform olarak sunulmuştur. Isıl fiber çekme metodu kullanılarak üretilen onlarca metre uzunluğundaki fiberler, yüzeylerinde 'V' şeklinde yivlerden oluşan yirmi kanal içermektedir. Fiber yüzeylerinin polidopamin (PDA) ve Ultraviyole/Ozon (UV/O) gibi işleme tekniklerle modifiye edilmesinden sonra fiberlerin üstündeki yivler boyunca kılcal hareketten kaynaklanan yayılma yönüne bağlı olarak sıvı akışkanlığı gözlemlenmiştir. Üç boyutlu esnek fiberlerden oluşan diziler üzerinde, herhangi bir harici pompa veya hareketlendirici mekanizma olmaksızın önceden belirlenmiş kanallarda kendiliğinden

sıvı aktarımı sağlanabilmektedir. Ayrıca, yüzeyi organik olarak modifiye edilmiş nano parçacıklar V yapılı yivlerin üzerinde kullanılarak fiber yüzeylerin hidrofobikliği artırılmıştır. Yüzeyleri şekillendirilmiş fiberlerin, esnek, sağlam, hafif ve ekonomik mikrodamlacık tabanlı aygıtların üretimi için oldukça uygun olduğuna ve mikroakışkan aygıtların kullanım alanlarını yeni ilaç keşifleri, tıbbi tanılama, yiyecek ve su kaynaklarının kalitesinin denetlenmesini de kapsayacak şekilde genişleteceğine inanılmaktadır.

Anahtar Kelimeler: Mikroakışkanlar, Yöne bağlı ıslanma, Polimer fiber çekme, Kılcal akış, Kalorimetrik protein tahlili.

Acknowledgement

First and I would like to thank my academic advisor, Prof. Mehmet Bayındır for his invaluable support and guidance throughout my thesis. He has given me the necessary advice and motivation during the course of my study. I believe his enthusiastic approach to research has myriad contributions to my perspective in science.

I would like to thank Adem Yildirim for all the support he has provided me through this journey. In fact he was not only a friend and teammate to me, but also a role model. I would like to thank my friends and teammates; Fahri Emre Öztürk, Urandelger Tuvshindorj, Mehmet Kanık, and Merve Marçalı. I had a wonderful time working with them. I am grateful to prof. Çağlar Elbüken for his suggestions and invaluable comments that helped improved the quality of my thesis.

I want to express my sincere gratitude to my friends who helped steer the wheel with me all the time and reach out to me whenever I need their assistance. In particular I am grateful to Mustafa Fadlelmula, Abubakar Isa Adamu, Faruk Okur, Abba Usman Saleh, Umar Musa Gishiwa, Girayhan M. Say, Oyewole Benjamin Efunbajo, Bekir Türedi, Ahmet F. Yavuz, Tamer Doğan, and Kivanç Çoban.

I have good time and enjoyed sharing ideas with Bayındır research group members. They were the reason I felt comfortable to conduct my research in a conducive environment. I want to thank Tural Khudiyev, Ozan Aktaş, Erol Özgür, Gökcen Birlik Demirel, Ersin Hüseyinoğlu, Bihter Dağlar, Pınar Beyazkılıç, Osama Tobail, Mostafa El-Ashry, Murat Dere, Neşe Özgür, Emel Gürbüz, Dilara Oksüz, Hale Nur Çoloğlu, Pelin Tören, Orhan Genç, Arbab M. Toufiq, Ahmet Kağan Kolsuz, Reha Özalp, Ahmet Başaran, and Seyit Ali Yaşar.

I would like to thank all the faculty members, students and engineers at UNAM-National Nanotechnology Research Center. This work is partly supported by The Scientific and Technological Research Council of Turkey (TÜBİTAK) under project no: 113A055.

Last but not the least, I want to express my deepest and unlimited gratitude to my family; my father, and my mother, for all their support and steadfast throughout my academics. They have always believe in me and encourage me thoroughly.

To my family

Contents

| | |
|---|-----------|
| Chapter 1 | 21 |
| 1.1. Introduction | 21 |
| 1.2. Materials for Microfluidics Fabrication | 26 |
| 1.2.1. Soft Lithography..... | 27 |
| 1.2.2. Paper-based Microfluidic Devices | 28 |
| 1.3. Anisotropic Wetting in Microchannel | 30 |
| 1.4. Flow Regime in Microchannel | 35 |
| 1.4.1. Fluid Control | 35 |
| 1.5. Cell Biology in Microfluidics..... | 36 |
| 1.5.1. Laminar Flow for Cell Biology | 37 |
| Chapter 2 | 39 |
| 2.1. Thermal Fiber Drawing | 40 |
| 2.1.1. Preform Preparation | 40 |
| 2.1.2. Preform Drawing | 42 |
| Chapter 3 | 46 |
| 3.1. Polydopamine (PDA) Coating of PEI Fibers | 46 |
| 3.2. Extreme Anisotropic Wetting on Free-standing Textured Fibers | 50 |
| 3.2.1. Spontaneous Capillary Flow Calculation | 52 |
| 3.3. Preparation of Fiber Arrays | 53 |
| 3.3.1. Water Spreading Dynamics of Fiber Arrays | 55 |
| 3.4. Three-dimensional Microfluidic Channels..... | 57 |
| 3.4.1. Effects of Channel Length and Shape on Channel Filling Time..... | 60 |

| | |
|---|-----------|
| 3.5. Microfluidics Switch Design | 61 |
| 3.6. Flexibility of the Channels | 62 |
| 3.7. Protein Assay as a Proof of Concept | 64 |
| Chapter 4 | 69 |
| 4.1. Fabrication of Surface Textured Polymer Fibers | 71 |
| 4.2. Introduction of Nano-scale Roughness on the Fiber Surfaces | 74 |
| 4.2.1. Ormosil Nanoparticle Coating..... | 74 |
| 4.3. Surface Characterization of Fiber Arrays | 75 |
| 4.3.1. Comparison of Anisotropic Behavior on Fiber Arrays | 79 |
| 4.4. Droplet Manipulation on Fiber Arrays and Tracks | 82 |
| Chapter 5 | 86 |
| 5.1. Experimental Section | 87 |
| 5.2. Surface Modification of Hierarchical PC Fiber by UV/Ozone | 94 |
| Chapter 6 | 96 |
| 6.1. Conclusion..... | 96 |
| 6.2. Future Work | 97 |
| Bibliography | 99 |

List of Figures

Figure 1: Disposable polymer microfluidic devices. (A) Basketweave pattern of a 3D PDMS microchannel system. (B) Multilayer microchannels replicated in thermoset polyester (TPE). (C) Embossed microstructures in PMMA. (D) PMMA device fabricated using laser ablation (CO2 laser) [1]. 28

Figure 2: A fluidic de-multiplexer. Fluid from a single inlet can deliver fluid to eight combination of outlets by using this device. The device consists of a fluid inlet, eight ‘on’ buttons, and eight circular zones connected to the outlet of each button. (A) Schematic illustration of the layers in the fluidic de-multiplexer. (B) The de-multiplexer can be switched by compressing the ‘on’ buttons before or after the fluid is added to the fluid inlet. Ball-point is used to press the buttons at one minute intervals after adding fluid (1 mM Erioglucine) to the inlet. (C) Pictures of de-multiplexers after compressing different buttons or combinations of buttons by adding fluid to the source. Each picture shows a different device switched on separately [33]. 29

Figure 3: Schematic view of water contact angle and Young’s equation. 31

Figure 4: The two different superhydrophobic models; (a) The Wenzel state in which the liquid wet the entire contour of the solid surface. (b) The Cassie state where the liquid only contacts the peak of the asperities and forms air pockets [88]. 32

Figure 5: Advantages of superhydrophilic-superhydrophobic patterns. Top: A water droplet on a superhydrophilic surface, and a water droplet on a superhydrophobic polymer surface. (A) Pictures showing the difficulty to control the size and geometry of a dye solution when printed on glass, whereas volume independent confinement of the same solution printed on an array of 500 μm superhydrophilic squares separated by 62.5 μm superhydrophobic barriers is realized. (B) Left: Superhydrophilic pattern filled with aqueous dye solution. Right: A water droplet on the superhydrophobic background with array of superhydrophilic spots filled with water. (C) Dye gradient on fluid stripes on a hydrophobic coated slide. (D) Microarray of droplets formed by dipping the patterned substrate (335 μm superhydrophilic squares, 60 μm

superhydrophobic barriers) into water. (E) Fluorescent cells cultured on a patterned substrate (335 μm superhydrophilic squares, 60 μm superhydrophobic barriers) for 48 h. (F) Image of water showing discontinuous dewetting when being moved along a patterned surface (1 mm diameter superhydrophilic circles, 100 μm superhydrophobic barriers) to form droplets only in the superhydrophilic spots [91]. 34

Figure 6: On-chip cell studies. (A) Optical micrograph of a fluorescence activated cell sorter (μFACS) device. (B) Fluorescence micrograph of two cell types [fluorescently labeled human bladder cancer cells (ECV304 cell line) and bovine adrenal capillary endothelial cells] deposited on a tissue culture dish in a polydimethylsiloxane (PDMS). (C) Optical micrograph of a normal red blood cell existing a blockage formed by malaria-infected erythrocytes in a PDMS microchannel. (D) Optical micrograph of a single Jurkat T cell captured in a cell dock [1]. 38

Figure 7: Polymer preform surface modification. (A) Lathe with preform mounted for structuring V-grooves, (B) PEI grooved preform, (C) PC grooved preform, and (D) edge view of PC grooved preform showing V-grooves and hollow core after removing Teflon rod..... 41

Figure 8: Fiber drawing scheme. (A) Stretched PC preform during fiber drawing, (B) Fiber drawing tower. 42

Figure 9: PEI fiber fabricated by thermal drawing method. (A) Photograph of preform after fiber drawing (scale bar: 5 mm). (B) Photograph of drawn microstructured fibers of several meters showing their robustness and flexibility (scale bar: 1 cm). 43

Figure 10: (A) SEM micrograph of a 500 μm diameter and a 200 μm diameter textured polymer fiber showing microscale ordered grooves on their surfaces (scale bar: 100 μm). (B) SEM cross section of ordered micro grooves on textured fibers. Fibers preserve their 20 equilateral V - grooves along their length (scale bar: 50 μm)..... 44

Figure 11: Cross-sectional SEM image of smooth PEI fiber with a diameter of 300 μm . (Scale bar: 100 μm)..... 45

Figure 12: PDA coating and characterization. (A) PDA coating is achieved by dipping the fibers into dopamine solution for a determined time (scale bar: 1 cm). (B) AFM micrographs of uncoated and PDA coated fiber surfaces. After surface modification

| | |
|--|----|
| nanoscale roughness is introduced with PDA coating to the fiber surface (scale bar: 1 μm). (C) C1s XPS spectra of uncoated and PDA coated fibers..... | 47 |
| Figure 13: (a) Absorption spectrum of dopamine solution, which is polymerized for 24 hours, showing the broad absorption of PDA. (b) Transmission spectra of PDA coated and bare PEI film. Film transmission decreased significantly after PDA deposition. | 48 |
| Figure 14: FTIR spectrum of PDA powder, which is polymerized for 24 hours. Inset shows the assigned peaks..... | 49 |
| Figure 15: Exceptional anisotropic wetting of star-shaped fibers. Dyed water is introduced to a free standing PDA coated star-shaped fiber. (A) Each fiber has 20 individual, parallel micro-channels on its surface (scale bar: 3 mm). (B) Close up photograph of the fiber end (scale bar: 100 μm). (C) Cross sectional view of the dyed water introduced fiber (scale bar: 100 μm). (D) The case when the water is introduced from the upper surface. Only the channels that come into contact with the water are filled (scale bar: 100 μm)..... | 50 |
| Figure 16: Colored water droplets (3 μL) on (A) PDA coated smooth and (B) uncoated star-shaped fibers, indicating that for complete wetting of fiber surface both V - groove structure and PDA coating is essential..... | 51 |
| Figure 17: Water contact angles (CA) of bare PEI (A) and PDA coated (B) PEI films. After modification with PDA hydrophobic polymer surface becomes very hydrophilic..... | 52 |
| Figure 18: Geometry of a single groove on a 300 μm diameter fiber filled with water. The groove is an equilateral triangle of side length 40 μm | 53 |
| Figure 19: Extremely anisotropic wetting of star-shaped fibers. (A) Wetting behavior of fiber arrays. Fiber surfaces are prepared by simply aligning the fibers on an adhesive tape. Parallel and perpendicular corresponds to the direction contact angle measurement is taken. When there is no PDA coating, star-shaped fibers are more hydrophobic from smooth fibers due to increased roughness of the PEI surface. After PDA modification of the surfaces, both smooth and star-shaped fibers show increased hydrophilic behavior. However, water is spread to the whole length of the fiber for star-shaped fibers. (B) Contact angle measurements of fiber array surfaces. (C) A fiber | |

| | |
|---|----|
| array comprised of 16 fibers of length 6 cm. Dyed water of different colors is introduced to the surface (scale bar: 2 mm)..... | 55 |
| Figure 20: Spreading rates in fiber arrays with various fiber diameters (500 μm , 300 μm , and 200 μm)..... | 57 |
| Figure 21: Construction of microfluidic networks with star-shaped fibers. (a) Spontaneous wetting is achieved in about 2.5 minutes to the whole length of 15 cm fibers aligned in a curved path (scale bar: 1 cm). Orange arrows show the point of dyed water introduction. (B) Distribution of liquid to multiple channels from single drop. Single fibers of diameter 300 μm spread the dyed water to any direction (scale bar: 5 mm). (C) Connection of microfluidic channels by stacking fiber arrays. Liquid spread on the above array is transferred to the below array (scale bar: 5 mm). (D) Shows a close up view of the connection point. (E) A three-dimensional system comprising of 4 channels crossing one another. At the intersection points, two uncoated larger hydrophobic star-shaped fibers are placed at the both sides of the below channel serve as spacers to prevent contact between below and above channels (bridge geometry). (Scale bar: 5 mm). (F) Shows close-up view of the bridge from a different angle.... | 58 |
| Figure 22: Demonstration of end to end added channels that can transmit water from one to another. Orange arrow shows the point of dyed water introduction. | 59 |
| Figure 23: Water (20 μL) filling times of four different open microfluidic channels. | 60 |
| Figure 24: Switches that control water spreading. Utilizing the observed liquid transfer upon stacked fibers, a simple button mechanism is shown. (A) Initially there is no liquid at the below array, there is no intermixing between above and below arrays (i) (scale bar: 5 mm). (ii) When the above array is pressed down with a tweezer it comes into contact with the below array and spontaneous spreading begins at the below array instantaneously. (iii) After release of the above array it relaxes back to its initial position and there is no further liquid transfer between channels. At the end stage water is distributed to the whole length of the below array. (B) Interplanar button mechanism. This example shows a button for liquid transfer between planes. Spontaneous spreading begins instantaneously by contact with the already wet array (scale bar: 5 mm). | 62 |

Figure 25: Fiber based microfluidics unrestricted with planar based systems. Since fibers are flexible, the observed anisotropic wetting behavior can be achieved on any surface. (A) Spontaneous wetting on fibers of length 15 cm rolled around a glass tube (scale bar: 5 mm). (B) Microfluidic channel array on a flexible surface. The array consists of about 120 microchannels on 12 fibers, uncoated 500 μm star-shaped fibers are added in between the coated 300 μm fibers for avoiding the delivery of liquid to the wrong array (scale bar: 5 mm). 63

Figure 26: An example of a microfluidic channel demonstration on a three-dimensional object which shows fluid climbing a ramp. Orange arrow shows the point of dyed water introduction 64

Figure 27: Protein assays. (A) Demonstration of water transfer from a microfluidic channel to a piece of filter paper. (B) A protein assay composing of three detection zones. Upon addition of HSA immediate color change occurred at all detection zones (scale bar: 1 cm). (C) A protein assay composing of three analysis and control spots and three switches. After activation of all switches color change was observed in analysis spots (scale bar: 5 mm)..... 65

Figure 28: Concentration dependent colorimetric response of the array. All experiments were performed in triplicate. Mean color intensities were calculated by averaging the change in the RGB values (compared to white) of randomly selected pixels. Inset shows the photographs of the color change in the assays after protein introduction. 66

Figure 29: Side view of a gap covered with a piece of paper, similar to the control spots in the protein assay. Although the two channels are connected over the gap with a piece of paper, blue colored water (introduced to the channel at left) did not transfer to the other channel (right channel). 67

Figure 30: Fabrication scheme of V - grooved PEI microfibers and surface modification with nanoparticle coating. (a) Thermal drawing of V - grooved microfibers from the macroscale star-shaped PEI preform. (b) SEM micrograph illustrating cross-sections of (i) 200 μm and 500 μm sized fibers with 20 parallel V-grooves (scale bar: 100 μm), and (ii) 500 μm size fiber showing the textured microgrooves that form microchannels which extend along its entire length (scale bar:

100 μm). (c) SEM micrographs of a coated fiber showing homogeneously coated nanoparticles (scale bars: 15 μm and 1.5 μm (inset)). (d) AFM micrographs of uncoated and nanoparticle coated fibers. Nanoparticle coating introduces a random nanoscale roughness on the ordered microscale roughness of the fiber surfaces (scale bars: 0.5 μm). 72

Figure 31: SEM image of (a) cross-section of smooth PEI fiber with a diameter of 300 μm , (b) 200 μm , 300 μm , and 500 μm of smooth PEI fibers, (c) cross-section of V – grooved fiber of 300 μm diameter, and (d) TEM micrograph of interconnected ormosil colloidal nanoparticles (with sizes of about 10 nm) forming a porous network layer. 73

Figure 32: Schematic illustration of ormosil nanoparticle spray coating on fiber surface. Spray gun is loaded with diluted ormosil solution, and then a surface is brought into close proximity (approximately 30cm away from the gun) with the gun. Ormosil gel was diluted in methanol solution. Pressurized nitrogen gas passes through the gun at 2 bar and the solution is sprayed onto fibers for about 2 – 3 s at ambient atmosphere. The sample is let dried at roomm temperature. 75

Figure 33: Model construction of surfaces for CA measurement on glass substrate using double sided tape (a), and CA values measurement on different substrates including glass, PC film, and PEI film and their coated surfaces (b). 76

Figure 34: (a) Contact angle measurements of fiber array surfaces (with each fiber 8 cm in length and 300 μm in diameter) with 4 μL water droplets. The measurements were taken from parallel and perpendicular directions, which correspond to the directions with respect to the fiber orientation of the surfaces. (b) Photographs showing the wetting behavior on PEI fiber surfaces. (i) The droplet on uncoated smooth fibers is in the Wenzel state, where spaces within the fibers are filled with water as seen in the inset. For nanoparticle coated smooth or uncoated grooved fiber surfaces, the droplets are in an intermediate state between Cassie and Wenzel states. (ii) The smooth fiber surface is wet, but the water cannot penetrate the in-fiber spaces for the array of coated smooth fibers. (iii) For the case of uncoated grooved fibers, water filled the micro-channels within the microscale grooves yet cannot wet the spaces between the fibers as seen from the inset. (iv) The droplet is in the Cassie state on nanoparticle

coated grooved fibers. The water droplet rests on the tips of triangular protrusions on the fibers and water cannot penetrate the grooves or the spaces between fibers. 78

Figure 35: Comparison of groove dimension on the basis of anisotropic behavior. (a) Uncoated 200 μm , 300 μm , and 500 μm grooved PEI fiber arrays, and (b) coated 200 μm , 300 μm , and 500 μm grooved PEI fiber arrays..... 80

Figure 36: (a) Roll-off angle values measured on ormosil coated grooved fiber arrays (FA) formed by fibers with diameters of 500 μm , 300 μm and 200 μm (FA500, FA300 and FA200), and their combinations (FATrack1 and FATrack2). (b) Anisotropy ($\Delta\theta = \theta_{\perp} - \theta_{\parallel}$) of the fiber arrays, showing enhanced anisotropic non-wetting behavior on FATrack1 and FATrack2 surfaces. (c) Photographs of droplets on FATrack1 and FATrack2. (i) FATrack1 is a parabolic array of 500 μm /300 μm /200 μm /300 μm /500 μm fibers. (ii) FATrack2 is a channel composed of 500 μm x2/200 μm x3/500 μm x2 array. (d) The relation between roll-off angle and droplet volume on FATrack2. Roll-off angle decreases with increasing droplet volume in both parallel and perpendicular directions. However, roll-off angle is higher in the perpendicular direction for all droplet volumes, which demonstrates the anisotropic non-wetting behavior of the surface. (e) Roll-off and adhesive properties of nanoparticle coated smooth and grooved fiber surfaces. (i) Anisotropic roll-off in parallel direction on the FA300 surface tilted at 14°. (ii) The droplet remains pinned to a nanoparticle coated fiber surface with 300 μm smooth fibers even when the surface is tilted at 90°. (iii) Pinned droplets on a flexible substrates for conceptual demonstration. 82

Figure 37: Droplet transport and mixing. (a) Snapshots of a 4 μL suspended droplet on the roll-off superhydrophobic fiber surface (array of 300 μm coated grooved fibers). The droplet is transferred from the superhydrophobic surface to the sticky surface (array of nanoparticle coated 300 μm fibers) upon bringing the two surfaces in close proximity. (b) Droplet transportation with fiber surfaces prepared on arbitrary surfaces. (i) An array of 300 μm coated smooth fibers was prepared on the fingertip of a nitrile glove. By gently touching the resting blue dyed water droplet (on the 300 μm nanoparticle coated grooved fiber surface), it was transferred to the fingertip. (ii) The blue droplet was carried on the fingertip and was contacted with the red dyed droplet

| | |
|--|----|
| resting on a sticky surface manually. (iii) The resulting droplet after mixing of the initial red and the blue droplets. | 83 |
| Figure 38: (a) Snapshots of a droplet rolling on the curved fiber track (FAtrack2) taken with a high-speed camera. Water droplet followed the curved path outlined by the fibers at a roll-off angle of around 11°. (b) A droplet based protein assay for colorimetric detection on linear fiber tracks. (i) Dispensing yellow BPB and colorless protein solution (8 μ L and 9 μ L, respectively). (ii) The instant of the droplet collision. (iii) Color change after coalescence of the two droplets. The yellow color of BPB solution changed to blue after mixing with the protein solution..... | 85 |
| Figure 39: Scheme of UV cabinet for UV/Ozone treatment of polycarbonate surfaces. | 88 |
| Figure 40: (a) and (b) X-ray photoelectron spectroscopy (XPS) survey spectra of PC surfaces before and after UV/O treatment for 30 minutes. (c) and (d) high-resolution C1s spectra of the PC surfaces before and after UV/O treatment for 30 minutes. | 89 |
| Figure 41: AFM micrograph of untreated and UV/O treated PC films. The treatment time was 30 minutes. Change in the roughness contour is seen as the surface reconstructed after the treatment. | 90 |
| Figure 42: Contact angle measurements of different type of polymer materials. (a) UV/O treated and (b) untreated surfaces..... | 91 |
| Figure 43: CA comparison between of PC film treated in an ambient atmosphere for 30 min and in excess O ₂ for 10 min. | 92 |
| Figure 44: (a) Exposure time dependent of CA measurement on PC film and (b) Effect of excess oxygen on different polymers..... | 93 |
| Figure 45: CA Measurement in time during treatment of PC with excess oxygen applied. | 94 |
| Figure 46: Multiscale rough PC polymer preform (a, b) and thermally drawn PC fiber with preserved multiscale roughness (c, d). | 95 |

List of Tables

| | |
|---|----|
| Table 1: Infrared bands of PDA powder | 49 |
| Table 2: RGB (Red, green and blue) values collected for 10 individual pixels for each analysis and control spot. RGB color model assigns a numerical value to each of the three primary colors, red, green and blue, in order to define each possible color as a function of the primary colors. The yellow shade of analysis spots and the blue shade of control spots were captured by a conventional scanner and RGB values were extracted by a commercial image editing software..... | 68 |

Chapter 1

Microfluidics

1.1. Introduction

For the past 15 years, significant developments in microfluidics have been achieved analogous to the benefits in miniaturization that microelectronics industry realized [1]. Utilization of minute quantity of sample and reagents in biological and chemical analysis is an important topic attracting scientists nowadays. In microfluidics, fluids at microliter, nanoliter, or picoliter volumes within micrometer-sized channels (ranging from 5 to 500 μm) are manipulated with respect to their physical consequences of microscale fluid dynamics. Also, due to small size, the used of microfabrication techniques adapted from the semiconductor and plastic industries are mandatory. These techniques include photolithography, micromachining, embossing, replica molding, and injection molding [2–11]. Miniaturization of the devices enables for automation of laboratory procedures for disease analysis and genomic applications. Rapidly advancing, lab on a chip has high promising potential in the mainstream of biological and chemical analysis that aims at using minute sample and reagent volume to attain low waste levels and specialty of microscale fluid flow. The smaller dimension of the microchannel is advantageous for reduced reagent handling cost [12]. The ability to produce large quantity of microfluidics device reduces cost. The main benefits regarding the use of microfluidics in biological and chemical analysis include fast analysis, short reaction times, portability of device, and multiplexing capability – parallel processing of samples. Until now, several platforms have been introduced as compact microfluidics that exhibit fast response time, high accuracy, high selectivity and high throughput. But, they are neither affordable nor disposable [1, 8]. Researchers have been working to find the way to make this technology prevalent in medical sector where it is believed to have strong hold. Right after its introduction by Terry et al. in

1979 as silicon-based analysis system, microfluidics has been the issue of modern medicine [11]. Then, in the 1990s, Manz et al. contributed to the advancement of microfluidics application [9]. Also, in the field of molecular biology, the emergence of genomics in 1980s required analytical techniques with high throughput and sensitivity. Microfluidic devices are used as portable diagnostic devices for the early detection of diseases such as diabetes, HIV, cancer, and cardiovascular [13–15]. In biological application they are used in DNA sequencing and immunoassays [4, 16–21]. Other microfluidic applications include microelectronic cooling systems, ink jet printing, and micro-reactors [22–27].

During the early stage of microfluidics technology, silicon, steel and glass were the first materials utilized to build specialized systems that require chemical and thermal stability. Mechanical stability of silicon and glass materials plays very important role in microfluidics in which channels with rigid and strong walls can be useful [8, 30, 31]. However, these material are not biocompatible, they are fragile (especially glass) and susceptible to chemical corrosion and require great labor of production. Microfabrication of microfluidic devices is tedious and consumes huge amount of time. Therefore, inexpensive, biocompatible, high throughput, scalable, and disposable microfluidic devices are highly demanded for biological and chemical analysis. Emergence of polymer materials mainly polydimethylsiloxane (PDMS) as a candidate material for microfluidic devices tackles aforementioned limitations. It promotes design simplicity and addressed much of the problems that early materials failed to provide when utilized in microfluidics. PDMS is the most commonly used material in research laboratories because of its outstanding physical and chemical properties. For instance, PDMS is used in microfluidics channels because it has advantages over glass and silicon such as flexibility, biocompatibility, elasticity, and high optical transparency. PDMS is unreactive and permeable to gases, and can be bonded to glass surfaces. Cells culture and DNA/protein separation are widely studied in PDMS. It is easily integrated with external components such as pumps, mixers, valve, flow sensors, and pneumatic sensors. However, PDMS has disadvantages despite being reliable microfluidics materials. It absorbs organic solvents which can be detrimental in cells study. Other polymer materials of interest are polystyrene (PS),

polycarbonate (PC), polyester and polyurethane (PU) which nowadays attract great attention of researchers due to their characteristic physical and chemical properties especially in cell culture [2, 12].

The state of the art of the existing microfluidics is usually integrated with external components to aid smoother fluid flow in some fluid dynamic regimes. External components that are integrated to microfluidics include pumps, valves, and mixers. These are the basic elements required for local controlled fluid movement inside microchannel. Scaling of forces in microfluidics is vital in order to understand which force is effective in microscale channel during flowing regime. Some forces are more dominant in the micro domain. The influence of different forces such as gravity, surface tension, and pressure varies with the dimension of the microchannel. Pressure force and electromagnetic field force are mainly employ for pumping fluid as they scale favorably in the microfluidics regime.

Scaling of Force field in Microfluidic Channel - Scaling law (Trimmer 1996, Wautelet 2001) explains the effect of these forces as the channel dimension decreases. Surface tension and Van der Waals scale linearly with length, however, are difficult to manipulate. Electrical force and pressure force scale to the square of the length dimension. Gravity and magnetic forces scale to the cube of the length dimension and are insignificant in microscale. Therefore, pressure and electrical forces are more dominant over all other forces in microfluidic regime. Surface property play an important role depending on the nature of material. Surface chemistry is a driving force in manipulating fluid by electrokinetic – electroosmotic flow in capillary electrophoresis, which is based on the movement of bulk solution in a capillary or channel due to the movement of counterions near the surface of the walls of the channels under the influence of an applied electric field.

Pressure driven pump is by far the most commonly used integrated pump in research laboratories. It is a benchtop laboratory equipment attached to microfluidic on a chip to drive fluid move across the channels, and therefore cannot be deploy to field for analysis. This kind of obstacles raise the issue to develop integrated compact

and portable microfluidics which uses nonmechanical pumps to produce steady flows. With this kind of microfluidic system, it is possible to carry out analysis in field or home at any instant. Consequently, new microfluidics architecture for simple yet complex devices utilizing nonmechanical pumps governed by various forces including electrokinetic, capillary action, and centrifugal force have been realized. Thus, the fabrication of open-channel microfluidics becomes possible.

As low-cost competitors of conventional fabrication methods, paper based methods have been developed [32–37]. Paper-based devices utilize capillary wicking to transport fluid through its porous media. Several research groups demonstrated that, using hydrophobic/hydrophilic patterned paper layers, it is possible to construct low-cost disposable devices that can direct liquid flow in three-dimensions [38–40]. However, fabrication of paper devices include tedious photo-lithography and stacking steps. In addition, production of channels with diameters smaller than a millimeter is very challenging due to the rough fibrous structure of the paper (i.e., porous cellular matrix of paper).

Recently, Bayindir research group has developed a new technique for fiber drawing based on thermal iteration. Thermal fiber drawing is a well-established top-down fabrication method which is used for the production of various functional micro and nanostructured fibers [41–44]. Here, we utilize fiber drawing for producing polymer fibers with very regular, aligned microscale surface textures. This approach enabled to introduce intrinsic advantages of fibers including large surface area, flexibility and directionality. Extreme anisotropic spreading behavior due to capillary action along the grooves of fibers is observed after surface modification with polydopamine (PDA). We utilized the fibers as universal microscopic building block to construct three-dimensional open-channel microfluidic devices by simply fixing them to surfaces using double sided tape to form pre-defined architectures. Note that there are examples in the literature that use fiber yarns or fabrics to produce microfluidic channels [45–48]. These studies use bundles of fibers to transport liquids by taking advantage of the porous structure of fiber network in a similar manner to the paper based channels.

In this study, on the other hand, we engineered fiber surfaces to produce well-defined microfluidic channels on individual fibers. We produced on-fiber microfluidic channels in two steps; i) star-shaped very long polymer microfibers are produced by thermal drawing of a surface-structured polyetherimide (PEI) preform, ii) surface of the fibers is coated with PDA in order to provide them hydrophilic surface chemistry and nano-scale roughness over their textured surface topography. The PDA functionalized star-shaped fibers exhibited extreme anisotropic superhydrophilic behavior, which enables confinement of small liquid portions through microgrooves on the fibers which are tens of centimeters in length. Flexibility of the fibers enables production of complex three-dimensional device geometries that can control liquid spreading in both lateral and vertical directions. We first demonstrated preparation of several fiber based microfluidic device components such as open-channels, connections, bridges and switches on both planar and unconventional geometries. We then developed a proof of principle colorimetric protein assay for human serum albumin (HSA) detection. In the second part of this work, anisotropic non-wetting of the structured fiber by functionalizing with organically modified silica nanoparticle was investigated. Therefore, it was proven that structured polymer fiber cannot only be functionalized to be superhydrophilic, but also superhydrophobic in the sense that directional nonwetting is observed akin to extreme anisotropic wetting. It is an intrinsic property of fiber that allows the selective surface modification. The realization of artificial surfaces with anisotropic non-wetting capability is inspiring for the development of self-cleaning surfaces, droplet microfluidics, droplet micro-reactors for precise chemical and/or nanomaterial synthesis, and droplet transportation at precise volumes [49–52]. Functional anisotropic surfaces of different architectures were constructed by fixing the fibers on paperboard, polymer, and glass substrates using double sided adhesive tape. The scalability of the fibers and optional nanoparticle surface modification enable construction of variety of fiber surfaces with different wetting characteristics. We demonstrated droplet transport with sticky hydrophobic (contact angle greater than 90°) and roll-off superhydrophobic (contact angle greater than 150°) surfaces, droplet guiding on track surfaces, and a simple protein assay with colliding droplets as examples of droplet manipulation with alternative surface designs. In the third part of this work, a new approach to

functionalization of PC fiber surface was studied. PC fiber was exposed under Ultraviolet/Ozone (UV/O) thereby altering its surface chemistry to enhance the wetting property to superhydrophilic (contact angle nearly 0°). Lastly, conclusion and future work are discussed.

1.2. Materials for Microfluidics Fabrication

The common fabrication methods of microfluidics include micromachining, photolithography, etching, micro-molding, bonding and laser writing [1]. Early versions of microfluidics were composed of silicon or glass patterned by micromachining [53, 54]. However, these materials have later been tremendously substituted and replaced by polymers due to their optical limitations such as transparency. Particularly, silicon is expensive and opaque [8]. Use of glass in microfluidics as a result of its facile fabrication technique has been around for a decade. It has been utilized in microfluidics due to its well-known fabrication method, surface stability, and chemical stability, and optical transparency. However, high cost of production and limited usage as disposable devices hinder its wide spread utilization in microfluidics [53]. PDMS is the common microfluidics material used for μ total analysis. It is a soft elastomer, inexpensive, flexible, and optically transparent to a wavelength roughly 230nm. Its biocompatibility enables biological studies because it is permeable to water, gases and nontoxic to cell. Another advantages of PDMS over silicon and glass is that, PDMS can be fabricated and bonded to a surface [2]. On the other hand, some cells materials are nourish in different environment and therefore polymers such as poly (methyl methacrylate) (PMMA), SU-8 and PC are preferably used [56–58].

PDMS is very attractive polymer that has essential properties for microfluidic channels. It can be used with aqueous systems of cell biology. It is electrically insulating and its surface can be oxidized to have Si-(OH) groups; thus PDMS is made hydrophilic. The hydrophilic surface of PDMS is suitable for cell adhesion in biological analysis or in fluid transport. These particular characters of PDMS make it

useful for biological studies. Fluid can be manipulated in PDMS microchannel depending on the design introduced during fabrication [57].

1.2.1. Soft Lithography

A term invented by Whitesides and coworkers, soft lithography in PDMS is one of the important contributions in microfluidics technology as a method of fabricating prototype devices [8]. This technique consists of replica molding of elastomeric material (PDMS) for the fabrication of microfluidics [4, 59]. It is also used for patterning using PDMS stamps onto a surface. Lithography of silicon wafer is involved in this method to pattern features using photoresist (SU-8), then PDMS molds are replicated with feature of sizes limited to 8 μm . Thin membranes patterned PDMS can easily be stacked to form 3D microfluidic systems (Figure 1A) [60, 61]. Replica molding incorporated with PDMS by pouring prepolymer (PDMS) directly onto a patterned silicon master and curing at moderate temperature (60° C for approximately 2h) to copy the desired architecture. Closed microchannel is designed by conformal sealing on any preferred material's surface [62, 63]. Soft lithography of PDMS has advantages including low-cost, fast processing (typically less than one day), multilayer fabrication of 3D devices, reusability, and suitability for cellular applications [64, 65]. The flexibility nature of PDMS is an intrinsic property that makes it viable for installation of fluidic interfaces from the macro-world to the microfluidic systems [66–68]. There are some drawbacks of PDMS which are limited compatibility with organic solvents, difficulties in controlling surface properties and permeability for carrying out in-channel oxygen-sensitive polymerization reactions [69, 70]. Roll et al. have demonstrated that cross-linked perfluoropolyether elastomers can be used instead of PDMS. Perfluoropolyether elastomers have properties akin to PDMS but do not absorb many organic solvents as does PDMS [69]. Also, other techniques are developed to design polymer materials for microfluidic applications including embossing and laser ablation (Figure 1B, C, and D).

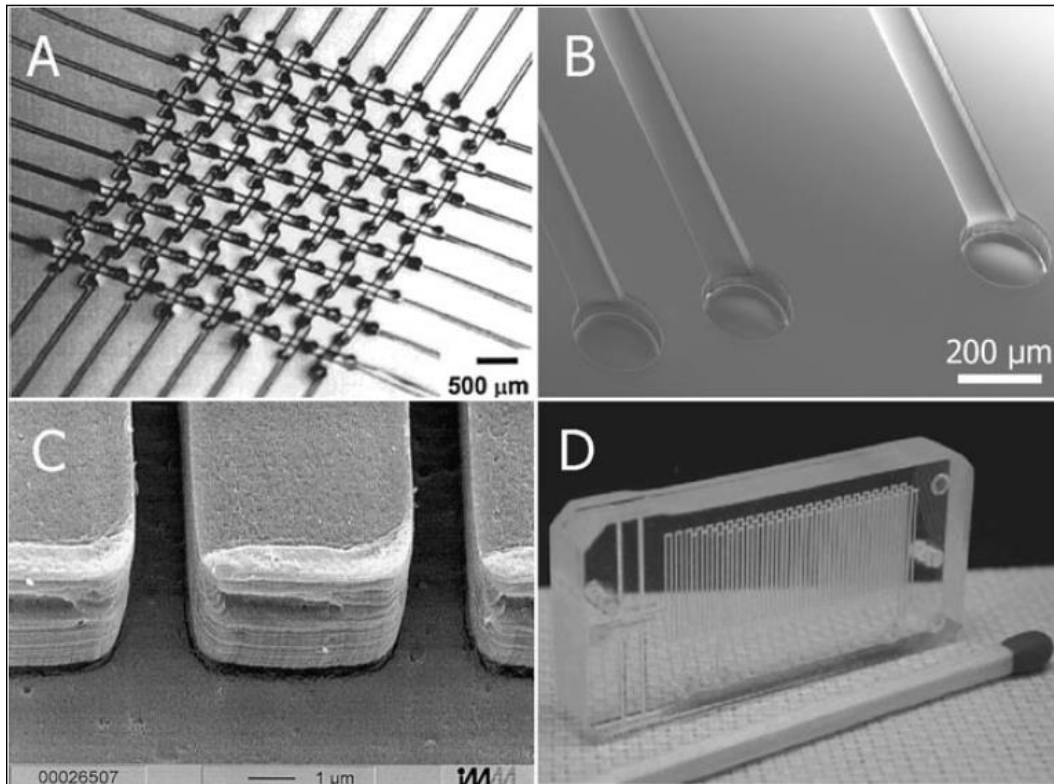


Figure 1: Disposable polymer microfluidic devices. (A) Basketweave pattern of a 3D PDMS microchannel system. (B) Multilayer microchannels replicated in thermoset polyester (TPE). (C) Embossed microstructures in PMMA. (D) PMMA device fabricated using laser ablation (CO₂ laser) [1].

1.2.2. Paper-based Microfluidic Devices

Due to the increasing demand of inexpensive, easy-to-use, and disposable microfluidic systems [32–37], paper-based analytical devices (PAD) (e.g., medical toolkit) are invented to foster early disease detection in developing countries [38–40]. PADs are made from paper material and then patterned into hydrophilic channels bounded by hydrophobic polymer with specific geometry. The channels of the device will be filled with fluid in a sequence predetermined by the design. Control of fluid over flow direction is programmable in which the device structure and its function are determined by the user after fabrication is complete. With programmable μ PAD, the user can select a desire channel of the device to be filled with fluid. A single device can multitask at a time according to the preferential frame of control. Figure 2A and B

illustrates the fabrication steps of paper-based microfluidic device (fluidic de-multiplexer). Simply pressing the connection zone (ON button) with standard ballpoint pen, fluid flows through the channels. The fluid de-multiplexer directed fluid from a single inlet through any combination of outlets. Tuning of specific channels within a time frame for analysis is demonstrated as seen in Figure 2C.

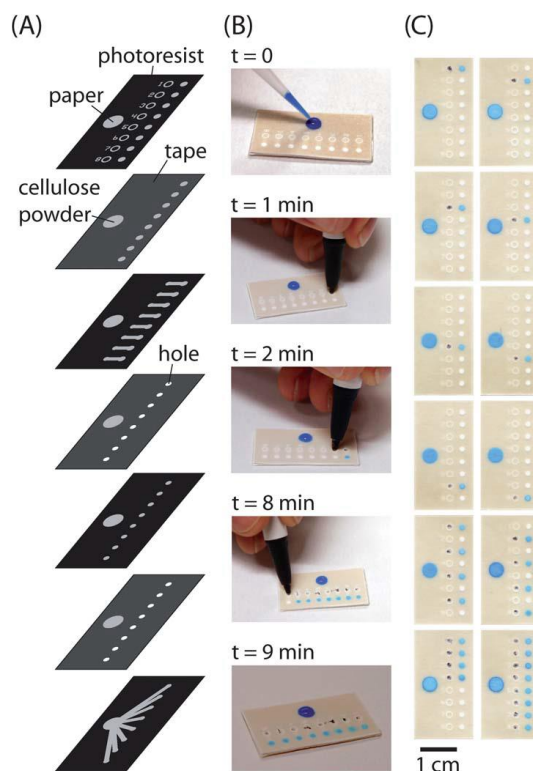


Figure 2: A fluidic de-multiplexer. Fluid from a single inlet can deliver fluid to eight combination of outlets by using this device. The device consists of a fluid inlet, eight ‘on’ buttons, and eight circular zones connected to the outlet of each button. (A) Schematic illustration of the layers in the fluidic de-multiplexer. (B) The de-multiplexer can be switched by compressing the ‘on’ buttons before or after the fluid is added to the fluid inlet. Ball-point is used to press the buttons at one minute intervals after adding fluid (1 mM Erioglucine) to the inlet. (C) Pictures of de-multiplexers after compressing different buttons or combinations of buttons by adding fluid to the source. Each picture shows a different device switched on separately [33].

1.3. Anisotropic Wetting in Microchannel

Anisotropic textured surfaces experience direction-dependent wetting properties which are merely observed on animals and natural bodies [72–75]. Surface wetting is characterized by understanding how liquid makes contact angle upon surfaces [76, 77]. Liquid wetting on solids depends on surface chemistry and surface roughness [76]. Through evolution and species selection, biological surfaces developed beneficial wetting properties such as superhydrophobic and superhydrophilic [52, 79, 80]. Special surface chemistry and surface geometry are the combined effect of wetting found in certain plants and animals [72, 73, 75]. Superhydrophobic, superhydrophilic and superoleophobic microchannels can be designed on any surface for microfluidics applications and self-alignment of microchips [81–84]. For instance, superhydrophobic surface of lotus leave enable self-cleaning [83]. Similarly, butterfly wings [84], moth eyes [85], and desert beetle [86] exhibit distinct wetting properties that can be mimicked to design microfluidics, biomedical devices, and other surface functional smart devices. Extensive research has been conducted to scrutinize biomimetic surface and their application in modern technology [87]. By principle, the contact angle (CA) of a material surfaces either increases or decreases with structural roughness. The roughness ascribed can be isotropic or anisotropic depending on the surface property required for different applications. Microstructured grooves and patterns are the common architecture used to induce directional wetting. The CA of a normal surface is a measure of its surface wettability. Young’s equation defined the CA of any normal surface in equation 1 below:

$$\cos \theta_c = \frac{\gamma_{SG} - \gamma_{SL}}{\gamma_{LG}} \quad (1)$$

Where γ_{SG} , γ_{SL} , and γ_{LG} are the surface tension of solid/gas, solid/liquid, and liquid/gas respectively. In Figure 3, CA measurement on a normal smooth surface is shown.

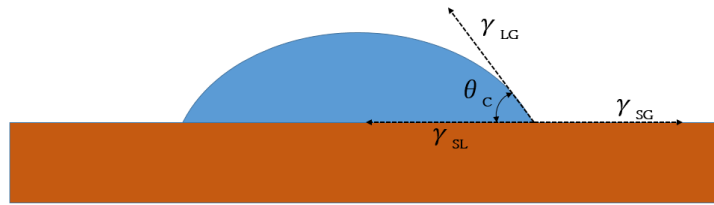


Figure 3: Schematic view of water contact angle and Young's equation.

Normal surfaces are classified as hydrophilic when the angle (θ_c) of the surface is independent of the droplet size and directly related to the $CA < 90^\circ$, and hydrophobic when $CA > 90^\circ$. Even though normal surfaces appear to be macroscopically smooth, they have some micro, nano, and/or molecular roughness scale. The young's equation does not hold when the surface roughness increases due to the existence of microscale geometries which protrude on the materials to alter the total contact area between solid and liquid. Therefore, wetting of the rough surfaces are described by two different wetting models developed by Wenzel and Cassie-Baxter (Figure 4). In the Wenzel model, the surface is completely wetted and water fills the rough space of the surface, whereas in the Cassie-Baxter model, the droplet wets the surface partially and air pockets form between the surface and water droplet such that the contact line is minimum [77, 78].

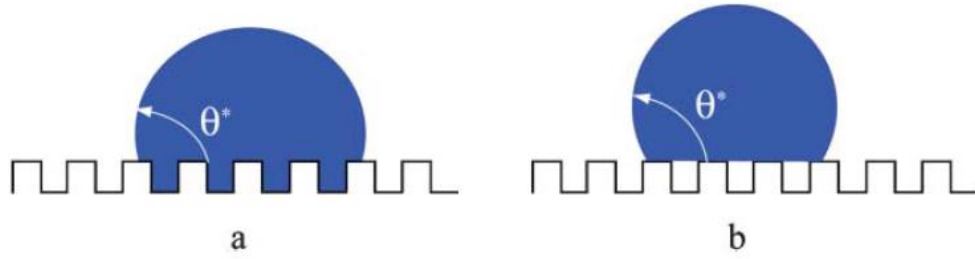


Figure 4: The two different superhydrophobic models; (a) The Wenzel state in which the liquid wet the entire contour of the solid surface. (b) The Cassie state where the liquid only contacts the peak of the asperities and forms air pockets [88].

The Wenzel model equation is written as:

$$\cos \theta_W = r \cos \theta_C \quad (2)$$

Where θ_W is Wenzel's CA on the rough surface, r is the roughness parameter: actual area divided by projected area of the surface and θ_C is Young's CA (contact angle of smooth material of same surface). The Cassie-Baxter model equation is written as:

$$\cos \theta_{CB} = -1 + \phi(1 + \cos \theta_C) \quad (3)$$

Where θ_{CB} is Cassie-Baxter's CA, ϕ is fraction of wetted area to whole area and θ_C is Young's CA (contact angle of smooth material of same surface). In Cassie State, water droplet roll-off from surface with CA $> 150^\circ$. On the other hand, in Wenzel state, water pinned to the surface [89]. Superhydrophobic describes the state of water droplet when CA $> 150^\circ$ and superhydrophilic is when the CA approaches 0° .

In 2007, McCarthy and Gao reinforced a theory proposed by Pease (1945) to question the ideas of both Wenzel and Cassie models [90]. They contended the underlying phenomenon of wetting by trying to prove that the CA of droplets on rough surface within the contact line were identical to those of smooth surfaces. This theory

goes against Wenzel and Cassie theories that are modelled based on the contact area and the area fractions on rough surface. According to McCarthy's theory, the contact line and the kinetics of droplet movement dictate the wettability. This affirms Bartell's and Extrand's works in trying to prove that the three - phase structure at the contact line controls the CA and not the liquid - solid interface.

Unique wetting properties arise from combination of superhydrophobic and superhydrophilic patterned regions as illustrated in Figure 5. Control of surfaces geometry enables easy positioning of liquid as depicted in Figure 5A. The combination of hydrophobic and hydrophilic wetting region is the reason of the selective wettability. Fluid can spread spontaneously within micropatterns and filled a specific spot without the need for surfactants (Figure 5B). Remarkable surface control is also demonstrated by the superhydrophilic patterns to confine fluid in microchannels due to surface tension as seen in Figure 5C. Droplets can be placed in close proximity on a surface without rupturing. The droplets positioning is an advantage for biological assay for minute reagent deposition (Figure 5D). Bioadhesion can be controlled by using the air-grid in Cassie-Baxter state (Figure 5E). Extreme difference in water CAs between superhydrophilic and superhydrophobic region leads to discontinuous dewetting without wetting the superhydrophobic background and passively dispensing aqueous solution into the superhydrophilic region as observed in Figure 5F [91].

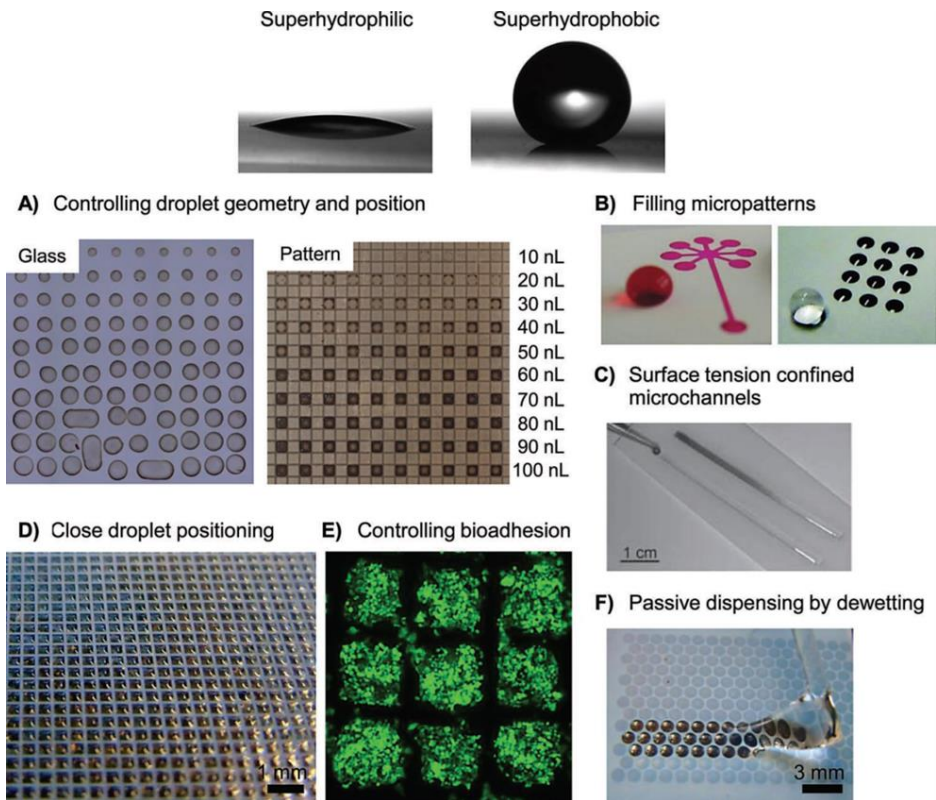


Figure 5: Advantages of superhydrophilic-superhydrophobic patterns. Top: A water droplet on a superhydrophilic surface, and a water droplet on a superhydrophobic polymer surface. (A) Pictures showing the difficulty to control the size and geometry of a dye solution when printed on glass, whereas volume independent confinement of the same solution printed on an array of $500\ \mu\text{m}$ superhydrophilic squares separated by $62.5\ \mu\text{m}$ superhydrophobic barriers is realized. (B) Left: Superhydrophilic pattern filled with aqueous dye solution. Right: A water droplet on the superhydrophobic background with array of superhydrophilic spots filled with water. (C) Dye gradient on fluid stripes on a hydrophobic coated slide. (D) Microarray of droplets formed by dipping the patterned substrate ($335\ \mu\text{m}$ superhydrophilic squares, $60\ \mu\text{m}$ superhydrophobic barriers) into water. (E) Fluorescent cells cultured on a patterned substrate ($335\ \mu\text{m}$ superhydrophilic squares, $60\ \mu\text{m}$ superhydrophobic barriers) for 48 h. (F) Image of water showing discontinuous dewetting when being moved along a patterned surface ($1\ \text{mm}$ diameter superhydrophilic circles, $100\ \mu\text{m}$ superhydrophobic barriers) to form droplets only in the superhydrophilic spots [91].

1.4. Flow Regime in Microchannel

One of the most important characteristic phenomena of fluid flow in microchannel, laminar flow-occur when two streams of fluid come together in microchannel, they flow in parallel without turbulence and diffusion of molecules occur across the interface between the fluids which results in mixing [8]. This type of flow requires the advancement of specific components to accomplish mixing in many situations. Components including pumps, valves, and mixers, have been developed to generate and handle fluid flow in microchannel [2]. The ratio of inertial to viscous forces on fluids is represented by the Reynolds number (Re) - a dimensionless number used in studying microfluidics [8]. Re is defined by the equation below:

$$\text{Re} = \frac{\rho v d}{\mu} \quad (4)$$

Where ρ is the density of fluid (g/cm^3), v is the velocity of the fluid (cm/s), and d is the hydraulic diameter (cm) of the channel. Fluid flow in microchannel is characterized by the dimensionless number Re. When the Re of a fluid is below ~ 2000 , the flow is laminar, whereas above 2000 the flow is turbulent. Fluids which do not mix, flow side-by-side in the microchannel by simply diffusing at their interfaces [93, 94].

1.4.1. Fluid Control

Some of the common fluid flow mechanisms which substantially play important role in controlling fluid motion in microchannels are pressure-driven and electrokinetic flow [1, 2]. In pressure-driven flow, the flow rate Q (m^3/s) is given by the equation;

$$Q = \frac{dP}{R} \quad (5)$$

Where dP is the change in pressure across the channel (Pa), and R is the channel resistance ($\text{Pa} \cdot \text{s}/\text{m}^2$). By applying vacuum at the outlet and opening the inlet to atmospheric pressure, pressure drop can be created. Electrokinetic flow is based on the molecule movement due to their charges in an electric field. Electrokinetic encompasses two components: electrophoresis, which is the consequence of the accelerating force due to the charge of a molecule in an electric field balanced compensated by the frictional force, and electroosmosis that creates a homogeneous flow of fluid down the channel. Small channels have advantage of high surface-to-volume ratio in terms of electrokinetic flow. They give out heat more than large channels [2]. Use of other principles for fluid flow in microchannels has been described. Capillary action is one of the schemes introduced with plasma-oxidized PDMS to deposit immunoglobulins onto a surface [95, 96]. In non-PDMS-based systems, gradient in temperature [96], patterning of self-assembled monolayers with distinct surface free energies [97], capillary action [98], and gradient in surface pressure [99], are the mechanisms used to direct fluid flow.

1.5. Cell Biology in Microfluidics

A vast applications of microfluidics devices in cell biology has been spotted recently, especially in the area of single cell analysis, DNA sequencing, separation, and so on. Initially, capillary electrophoresis (CE) based DNA analysis on-chip is utilized to separate oligonucleotide and sizing of longer DNA fragments [1, 12, 101–103]. The greatest benefit of performing cell study in microchannel is the faster process time realized than in the traditional slab-gel processes. On-chip DNA screening is faster and high throughput technique. For instance, DNA sizing on-chip microfluidics is typically 10 times faster than using capillary electrophoresis and 100 times faster than the traditional slab-gel platform [103]. Glass devices are used to perform DNA on-chip analysis with a sieving matrix of polyacrylamide in microchannel. There are several steps to follow when analyzing a DNA on-chip. First and foremost is the cell lysis - breaking down of cell by enzymic or osmotic mechanism. Then follow by

isolation of solid phase - tediously time consuming step. DNA amplification is very significant application of microfluidics. Basically, polymerase chain reaction (PCR) on-chip amplification decreases thermal cycling time which leads to the accomplishment of a shorter overall reaction time. There are various approaches including simple silicon microreaction chamber and a continuous flow PCR with capillary electrophoresis (CE) separation on-chip [105–109]. Leu et al., reported a fully automated and integrated microfluidic system capable of performing all the steps necessary for single cell study, starting from sample preparation to electrochemical via DNA hybridization [109]. With just 1 mL sample of blood introduced on the chip, full detailed analysis is conducted. One of the most outstanding features of the device is that all the necessary component required for fluid manipulation are already integrated [1].

1.5.1. Laminar Flow for Cell Biology

Fluid flow in microchannel is normally laminar flow, and this enables the deposition of cells and proteins on a solid surface [111–113]. This trick is employed to deliver ions and molecules to different parts of living cell with high precision in the subcellular level [113]. A solution containing mitochondrial dyes contacted different regions of a cell, and the movement of the various populations of mitochondria was monitored. It was observed that after 2.5 hour they thoroughly mixed Laminar flow was used to answer the fundamental questions of how signal transmission occurs in a cell upon stimulation by a ligand [12, 115]. Another technique called flow cytometry is adopted for clinical and disease diagnostic, cell screening, and antibody labelled bead assay. Hydrodynamic focusing together with T-channel design that utilized EOF to direct fluid flow for cell sorting (Figure 6A). Another advantage of microfluidics is that, single cell capture is very handy with high precision. It is demonstrated to have deposited multiple types of cells over a surface with controlled location [1, 116]. This widens the horizon for fundamental studies in cell biology (Figure 6B).

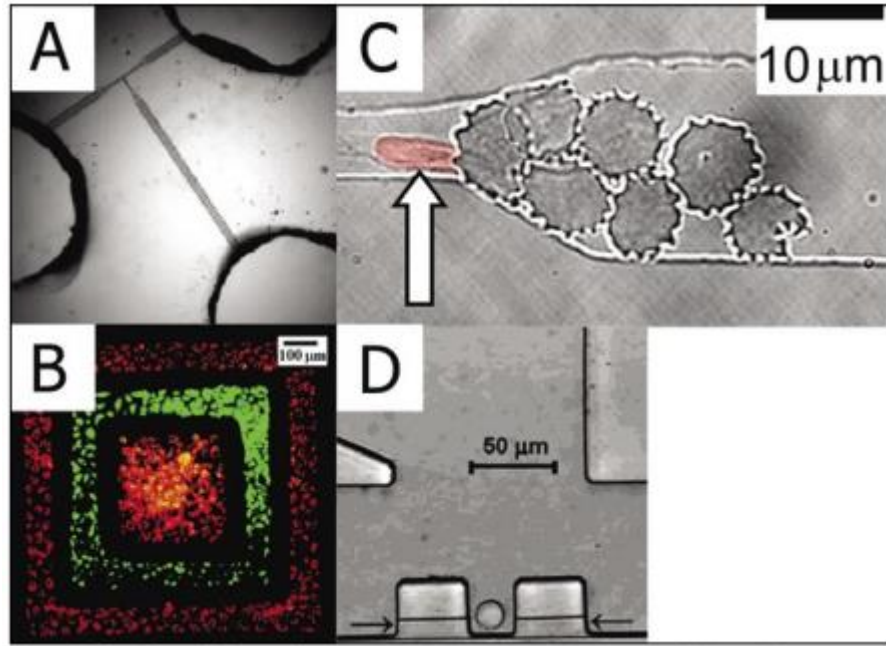


Figure 6: On-chip cell studies. (A) Optical micrograph of a fluorescence activated cell sorter (μ FACS) device. (B) Fluorescence micrograph of two cell types [fluorescently labeled human bladder cancer cells (ECV304 cell line) and bovine adrenal capillary endothelial cells] deposited on a tissue culture dish in a polydimethylsiloxane (PDMS). (C) Optical micrograph of a normal red blood cell existing a blockage formed by malaria-infected erythrocytes in a PDMS microchannel. (D) Optical micrograph of a single Jurkat T cell captured in a cell dock [1].

Chapter 2

Fabrication of Anisotropic Polymer Fiber

Microfluidic channels that use capillary wicking or directional wetting to control liquid flow are promising alternatives to conventional systems that require external pumps, which limits the simplicity and integrity of the system and thus restricts its use in a number of applications [73, 117–121]. In these channels, liquid flow is controlled by anisotropic (i.e. directional) surface structures (e.g. grooves, pillars and nanowires) or surface chemistry (e.g. hydrophilic/hydrophobic patterns) [70, 74, 122–127]. Such systems are widespread and have been fabricated on a variety of surfaces including glass, silicon and polymers. Current fabrication methods of both physically and chemically patterned surfaces are dominantly based on micro-fabrication techniques such as photolithography, laser-writing and plasma etching [83]. Although these techniques have shown to be very successful for shaping material at the microscale, they are impractical for fabrication of affordable microfluidic systems. In addition, fabrication of three-dimensional architectures, which is particularly important for compact and multicomponent microfluidic devices, is challenging with lithography based methods. In this chapter, the fabrication of polymer fibers of PEI and PC is discussed. Thermal reduction method was utilized to draw the fibers with variable diameters.

2.1. Thermal Fiber Drawing

Thermal fiber drawing is a well-established top-down fabrication method which is used for the production of various functional micro and nanostructured fibers. This simple and robust technique enables the drawing and maintaining well defined material geometries along the length of the fiber. In this work, we utilized fiber drawing method to fabricate and modify fiber surface by introducing V-grooves in order to obtain enhanced anisotropic wetting on the fiber surfaces. This is the first application of fiber drawing technique for the fabrication of surface modified fibers to the extent of our knowledge. High throughput of the fiber is the novelty of this method and the ability to structure the macroscopic fiber preform with a specific geometry such as the V-grooves.

2.1.1. Preform Preparation

Initially cleaned and kept in vacuum at 120 °C for a day, PEI film (AJEDIUM; 100 μm thickness and 35 cm width, RESIN – ULTEM 1000-1000) was tightly rolled around a Teflon rod under a clean pressure flow hood attaining a cylindrical PEI rod of 3 cm in diameter and 20 cm in length. The rolled PEI film and the Teflon rod were introduced into a consolidator (furnace) to fuse the PEI film thermally (*i. e.* consolidated) above its glass transition temperature, T_g (216 °C) under vacuum condition at 8×10^{-3} torr. Two heating regimes were applied to obtain a hollow core solid PEI preform. In the first regime, the rolled PEI film and the Teflon were heated to 180 °C at a rate of 15 °C min⁻¹ and kept at this temperature for 4 h. In the second regime, the temperature was increased to 257 °C at a rate of 2 °C min⁻¹ and kept in this temperature for 45 minutes to achieve consolidation. Finally, the inner Teflon rod was removed and we obtained a hollow core PEI preform. In order to introduce the V-groove structure, the

hollow core preform was mechanically shaped in lathe by rotating the preform at some angle and chipping away the material (Figure 7A). The dimension of the groove on the preform formed by the lathe determines the final fiber dimension. 20 continuous equilateral V-grooves that look like star-shape on the preform surface were structured (Figure 7B, C and D). The same procedure is applied during preparation of PC preform which is identical to the PEI preform. However, PC has T_g of $147\text{ }^\circ\text{C}$ which leads to difference in consolidation temperature regime. During the first heating regime, rolled PC film and the Teflon rod were heated to $140\text{ }^\circ\text{C}$ at a rate of $15\text{ }^\circ\text{C min}^{-1}$ and kept at this temperature for 4 h. In the second regime, the temperature was increased to $186\text{ }^\circ\text{C}$ at a rate of $2\text{ }^\circ\text{C min}^{-1}$ and kept in this temperature for 30 minutes.

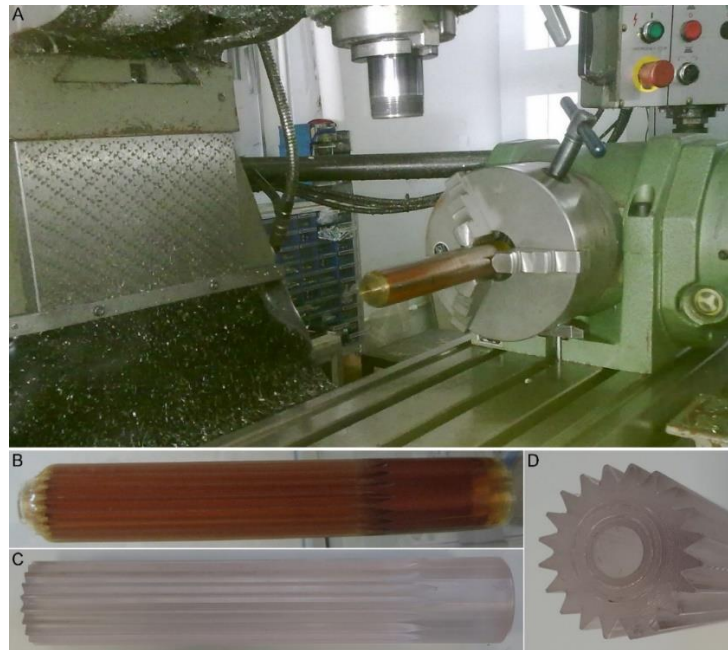


Figure 7: Polymer preform surface modification. (A) Lathe with preform mounted for structuring V-grooves, (B) PEI grooved preform, (C) PC grooved preform, and (D) edge view of PC grooved preform showing V-grooves and hollow core after removing Teflon rod.

2.1.2. Preform Drawing

After obtaining V-grooves on the polymer macroscopic preform, the preform was extended to a length of tens of meters, and was scaled down to smaller diameters in the range of micron via thermal fiber drawing. The macroscopic V-grooved preform was fed into a furnace vertically with a constant speed of 8 mm/min. The furnace was heated to a high temperature (approximately 305 °C for PEI and/or 230 °C for PC preform) and then a load is attached to the end of the preform to induce mechanical stress. The lower part of the preform dropped without rupturing as it softened as seen in Figure 8A. Consequently, fiber of reduced diameter of the initial preform was drawn by adjusting the stress level in the lower region of the using a constant speed motor (Figure 8B).

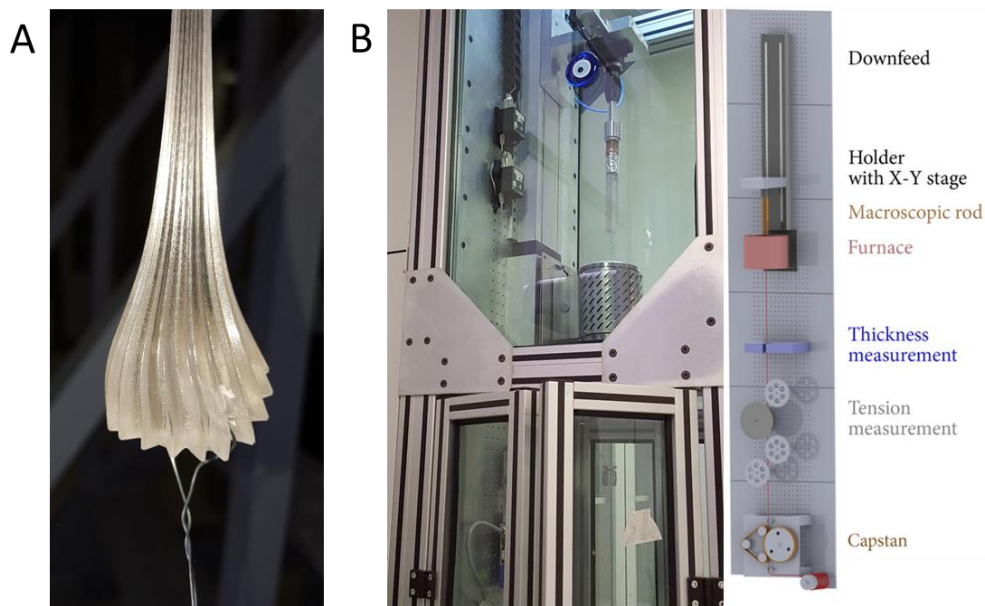


Figure 8: Fiber drawing scheme. (A) Stretched PC preform during fiber drawing, (B) Fiber drawing tower.

Precise control over temperature and the capstan enables drawing fiber with larger range in diameter. These two parameters can be manipulated and monitored by laser thickness measuring device. Therefore, the fibers have uniform diameter after scaling

down its dimension. Fiber with diameter as small as 200 μm was produced by increasing the capstan speed. It is worth noting that the initial shape of the preform with V-grooves was preserved down to micrometer without any interruption and surface damages. After the drawing process, the remaining part of the preform showed the diameter reduction area which appeared to be conical (Figure 9A). PEI fibers with several meters in length and few hundred microns in diameters were produced and rolled in bundle as shown in Figure 9B.

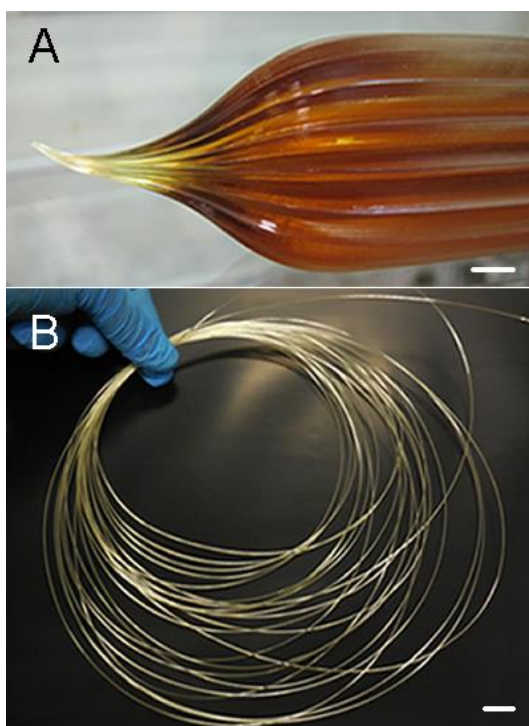


Figure 9: PEI fiber fabricated by thermal drawing method. (A) Photograph of preform after fiber drawing (scale bar: 5 mm). (B) Photograph of drawn microstructured fibers of several meters showing their robustness and flexibility (scale bar: 1 cm).

The surface texture of the microfibers was investigated by using SEM (Figure 10). The image in Figure 10A reveals 20 continuous perfectly aligned equilateral V-grooves on the fibers. It was observed that even after 150 fold size reduction from 3 cm (diameter of the preform) to 200 μm (thinnest fiber produced in this study), V-

groove with width of only 30 microns, was preserved. A cross-section of 300 μm fiber with the groove structures that extend along the length of the fiber is illustrated (Figure 10B).

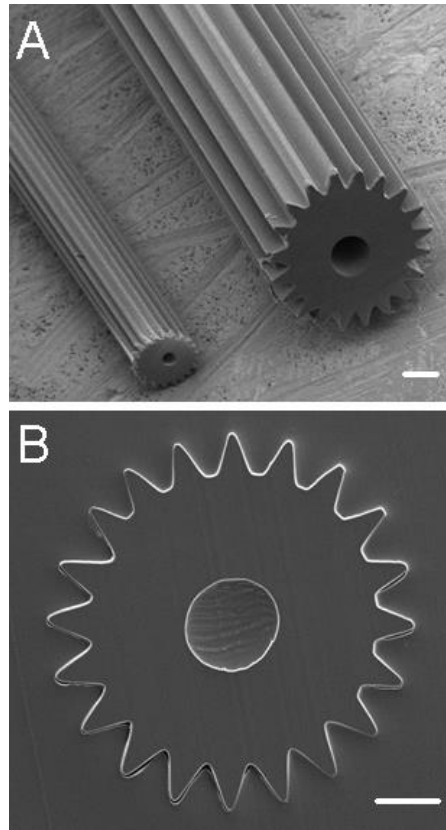


Figure 10: (A) SEM micrograph of a 500 μm diameter and a 200 μm diameter textured polymer fiber showing microscale ordered grooves on their surfaces (scale bar: 100 μm). (B) SEM cross section of ordered micro grooves on textured fibers. Fibers preserve their 20 equilateral V - grooves along their length (scale bar: 50 μm).

To distinguish the effect of geometry of the grooved fibers, fiber with smooth surfaces using a non-structured preform was produced Figure 11. This SEM image shows the smooth surface of the PEI fiber of which surface property varies as explained in the next chapters.

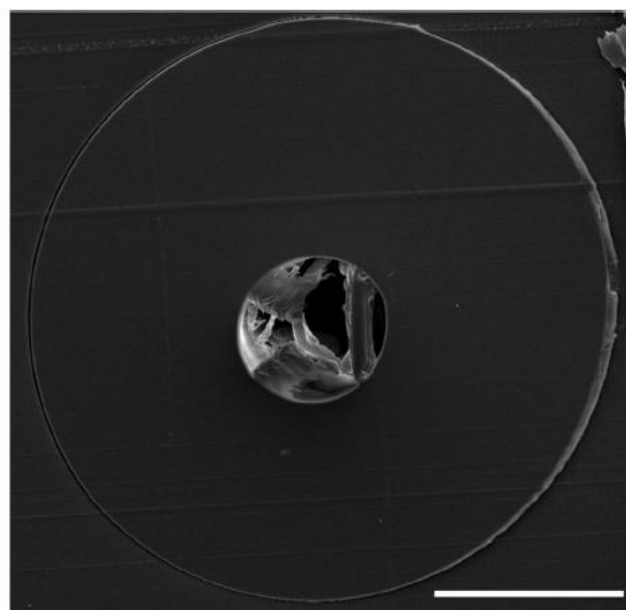


Figure 11: Cross-sectional SEM image of smooth PEI fiber with a diameter of 300 μm . (Scale bar: 100 μm).

Chapter 3

Modification of Surface Textured Polymer Fibers for Microfluidic

3.1. Polydopamine (PDA) Coating of PEI Fibers

PEI Fibers were coated with PDA by dipping into dopamine solution in order to make their hydrophobic surface to hydrophilic (Figure 12A). Surface topography images of uncoated and PDA coated smooth fibers indicates the formation of PDA nanoparticles after surface modification (Figure 12B). Chemical structure of the formed polymer (i.e. melanin like polymer synthesized using dopamine, commonly referred as polydopamine (PDA) on the surface of the fibers was investigated using XPS, FT-IR and UV-Vis absorption spectroscopies [128, 129]. Figure 12C shows the carbon 1s XPS spectra of PDA coated and uncoated PEI fibers.

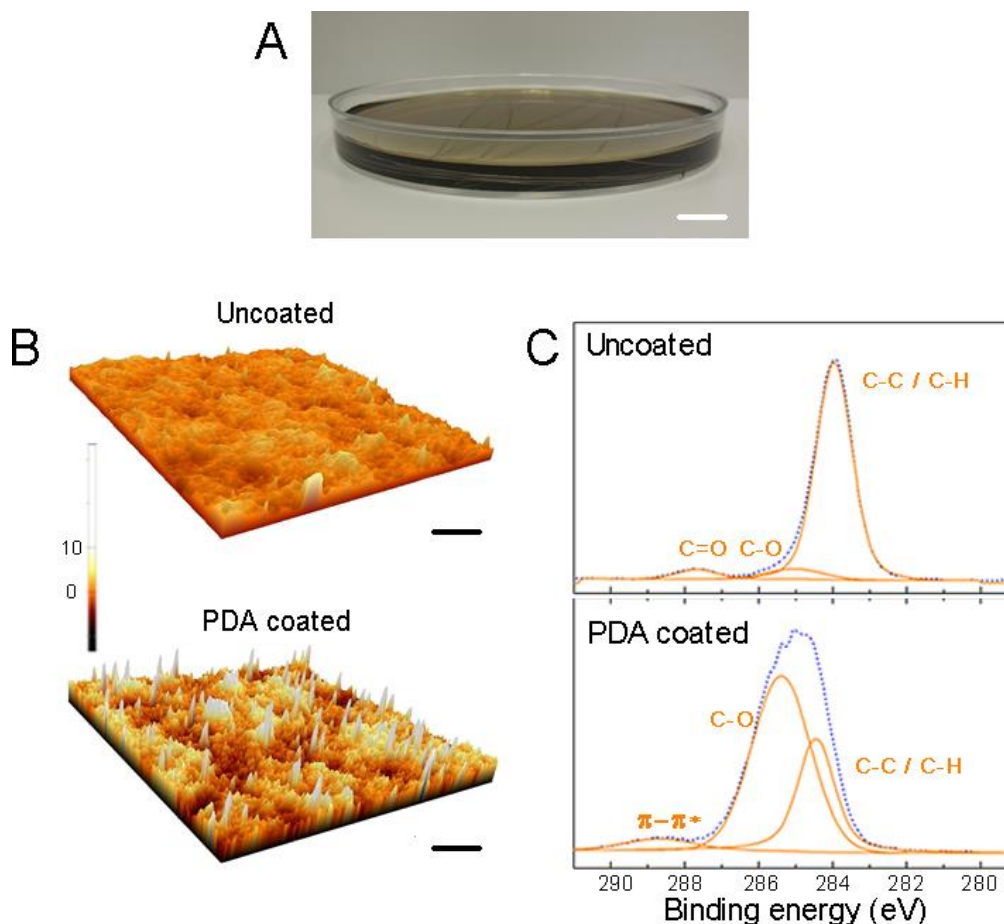


Figure 12: PDA coating and characterization. (A) PDA coating is achieved by dipping the fibers into dopamine solution for a determined time (scale bar: 1 cm). (B) AFM micrographs of uncoated and PDA coated fiber surfaces. After surface modification nanoscale roughness is introduced with PDA coating to the fiber surface (scale bar: 1 μm). (C) C1s XPS spectra of uncoated and PDA coated fibers.

For uncoated fibers, very weak C-O peak was observed. After PDA modification this peak becomes much more intense which suggests the presence of PDA on the surface which is in accordance with previous works [130, 131]. UV-Vis absorption spectra of the 24 h polymerized DA solution shows the typical broad band absorption of PDA (Figure 13a) [131]. The transmission of PEI film significantly reduced after coating with PDA (24 h) due to the broad band light absorption of PDA (Figure 13b).

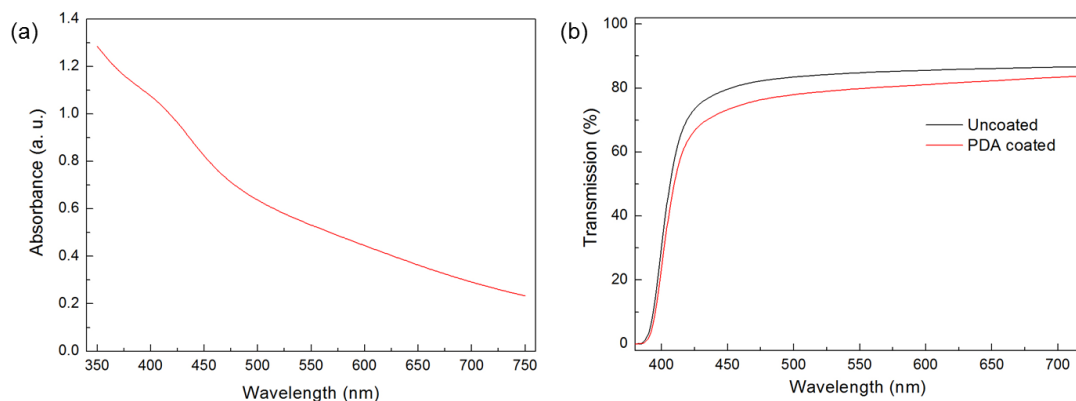


Figure 13: (a) Absorption spectrum of dopamine solution, which is polymerized for 24 hours, showing the broad absorption of PDA. (b) Transmission spectra of PDA coated and bare PEI film. Film transmission decreased significantly after PDA deposition.

FT-IR spectrum of PDA (24 h polymerized) powder shows absorption bands of indoline, indole, carbonyl, amino and hydroxyl groups of PDA which is also in accordance with previous reports (Figure 14 and Table 1) [131, 132]. Note that the exact chemical structure (it is assumed that PDA is composed of covalently linked dihydroxyindole, indole, and dopamine units) or microstructure (e.g. linear polymers, cyclic oligomers, physical aggregates or combinations of these structures) of PDA is still not fully resolved [132]; therefore we cannot conclusively determine the exact structure of the synthesized polymer in our experimental conditions. Nevertheless, our chemical analysis indicates a PDA polymer deposited onto the fiber surfaces.

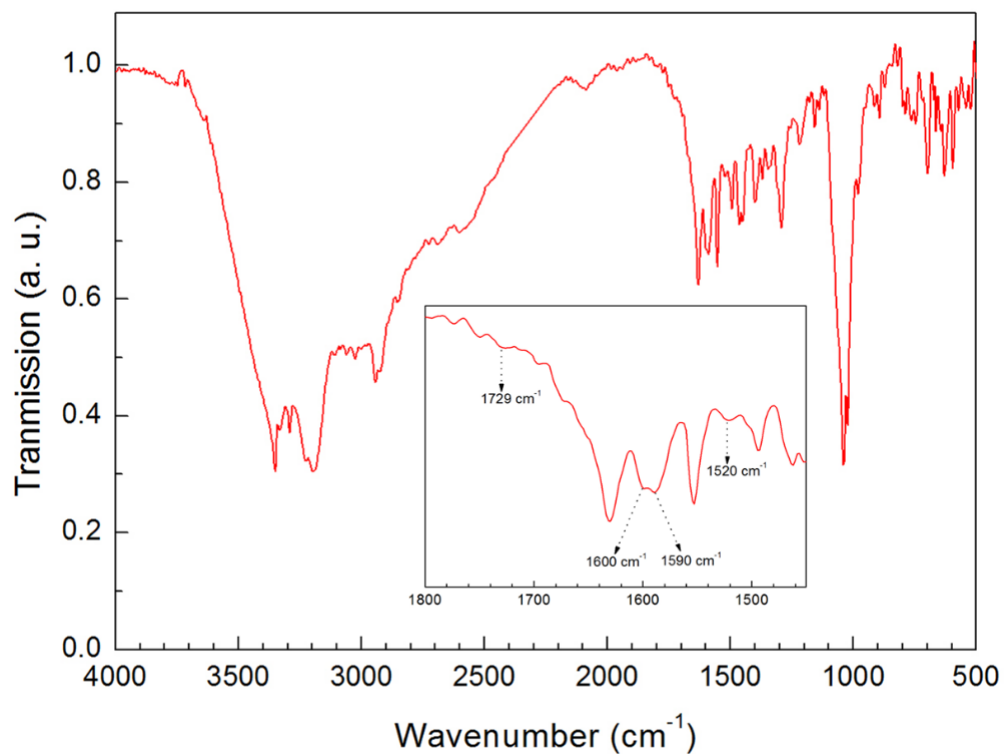


Figure 14: FTIR spectrum of PDA powder, which is polymerized for 24 hours. Inset shows the assigned peaks.

Table 1: Infrared bands of PDA powder

| Wavenumber (cm ⁻¹) | Assignment |
|--------------------------------|-------------------------|
| 3000 - 3500 broad | □(O-H), □(N-H) |
| 1728 weak, shoulder | □(C=O) |
| 1600 | □ _{ring} (C-N) |
| 1590 | □ _{ring} (C=C) |
| 1520 weak | □ _{ring} (C=N) |
| | |

3.2. Extreme Anisotropic Wetting on Free-standing Textured Fibers

Single free-standing PDA coated star-shaped fiber can transport water along the micron sized channels to its entire length in a few seconds when a water droplet was introduced from the middle of the fiber (Figure 15A). This extreme directional wetting property was not observed on PDA coated smooth fibers or on uncoated star-shaped fibers (Figure 16) which indicates that the three scale roughness and hydrophilic surface chemistry is essential to provide total wetting of the fiber surface. Figure 3.4B and C show the edge of the fiber with a diameter of 500 μm whose surface grooves were filled with blue-colored water. In addition, we observed that microgrooves transport the water along the fiber but not to their neighbor grooves (Figure 15B, C and D). Therefore, it is possible to select liquid transport channels by adjusting the droplet size and contact area.

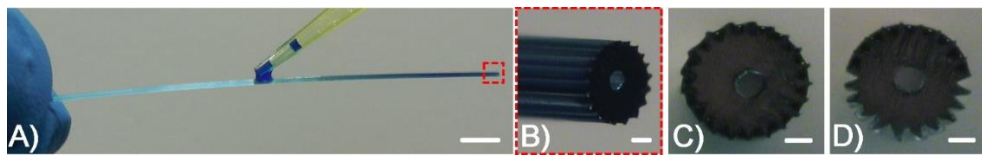


Figure 15: Exceptional anisotropic wetting of star-shaped fibers. Dyed water is introduced to a free standing PDA coated star-shaped fiber. (A) Each fiber has 20 individual, parallel micro-channels on its surface (scale bar: 3 mm). (B) Close up photograph of the fiber end (scale bar: 100 μm). (C) Cross sectional view of the dyed water introduced fiber (scale bar: 100 μm). (D) The case when the water is introduced from the upper surface. Only the channels that come into contact with the water are filled (scale bar: 100 μm).

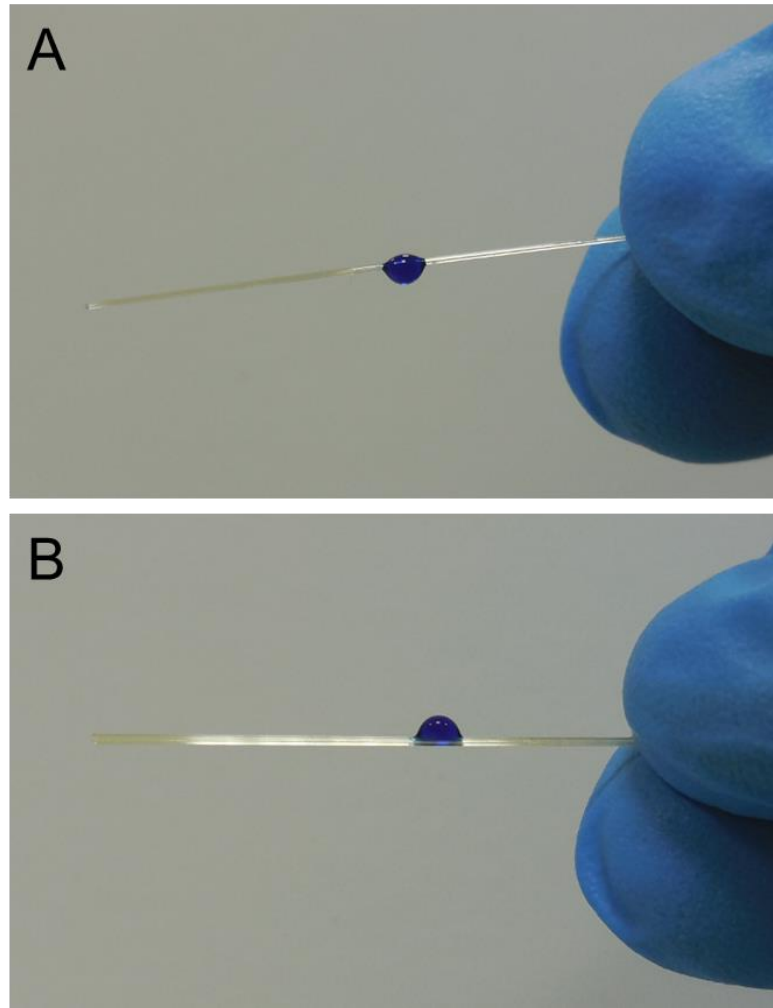


Figure 16: Colored water droplets (3 μL) on (A) PDA coated smooth and (B) uncoated star-shaped fibers, indicating that for complete wetting of fiber surface both V - groove structure and PDA coating is essential.

In order to better understand the extreme anisotropic wetting behavior of the grooved fiber surface, we applied spontaneous capillary flow equation (Equation 6) [117]. PEI is a hydrophobic material with a water contact angle of 97° and after modification with PDA, surface becomes hydrophilic with a water contact angle of 32° (Figure 17).

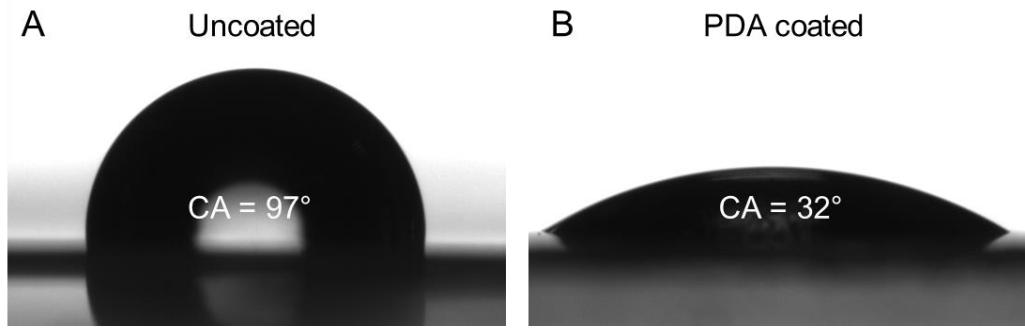


Figure 17: Water contact angles (CA) of bare PEI (A) and PDA coated (B) PEI films. After modification with PDA hydrophobic polymer surface becomes very hydrophilic.

3.2.1. Spontaneous Capillary Flow Calculation

The spontaneous capillary flow equation is applied on V-groove geometry of star-shaped fibers [117]. Figure 18 shows a groove of 300 μm diameter fiber filled with water. The ratio of free perimeter (liquid air contact line length) ‘ P_f ’ to wet perimeter (liquid solid contact line length) ‘ P_w ’ gives the contact angle limit ‘ θ ’ for spontaneous wetting (*i.e.* contact angle value of the smooth surfaced material that would allow spontaneous wetting at the studied geometry).

$$\frac{P_f}{P_w} < \cos \theta \quad (6)$$

$$\frac{P_f}{P_w} = \frac{L}{2L} \quad (7)$$

$$\theta < 60^\circ \quad (8)$$

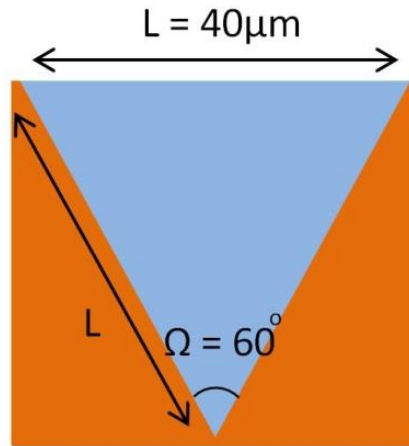


Figure 18: Geometry of a single groove on a 300 μm diameter fiber filled with water. The groove is an equilateral triangle of side length 40 μm .

Equations 6, 7, and 8 yield contact angle limit of about 60° for spontaneous spreading on our grooved geometry (Figure 18). Therefore capillary action is favorable in PDA coated star-shaped fibers (which have CA of 0° below the calculated limit of 60° for groove geometry) but not in uncoated ones. This observations strongly supports our experimental result. Equation 6 helps us in understanding the contribution of micro V-grooves by observing extreme anisotropic wetting properties of star-shaped fibers [134–136].

3.3. Preparation of Fiber Arrays

After demonstrating the extreme wettability on free-standing fibers, we prepared several fiber arrays by fixing them to paperboards using a double sided adhesive tape and characterized their wetting properties (Figure 19A). We measured the water contact angles of the surfaces in both parallel (*i. e.* contact line is parallel to the fiber orientation) and perpendicular (*i. e.* perpendicular to the fiber orientation) directions (Figure 19B). Uncoated arrays of both smooth and star-shaped fibers demonstrated improved hydrophobicity compared to the PEI film due to the single or double micro scale roughness of these surfaces. On the other hand, after PDA functionalization,

fibers become very hydrophilic. However, the effect is exceptional in the case of PDA coated star-shaped fiber array; contact angle values reach 0° in both directions. The extreme anisotropic superhydrophilic behavior of the textured fiber array was also visualized in Figure 19C. It is important to note that, 8 μL of dyed water droplets spread to the 7 cm long fiber array within only 5 seconds. Also, similar to the on-fiber micro channels, these macroscopic channels transport the liquid along the fiber but not to the neighbor fibers which avoids intermixing. In addition, we investigated the spreading rate of water on 6 cm long fiber arrays consisting of four fibers, with each array consisting of different sized fibers (200 μm , 300 μm and 500 μm). We observed that filling time decrease with increasing fiber size. Further, spreading distance (L) is accurately proportional to square root of time (\sqrt{t}), which is in accordance with previous reports that investigate spreading dynamics on V - grooves.

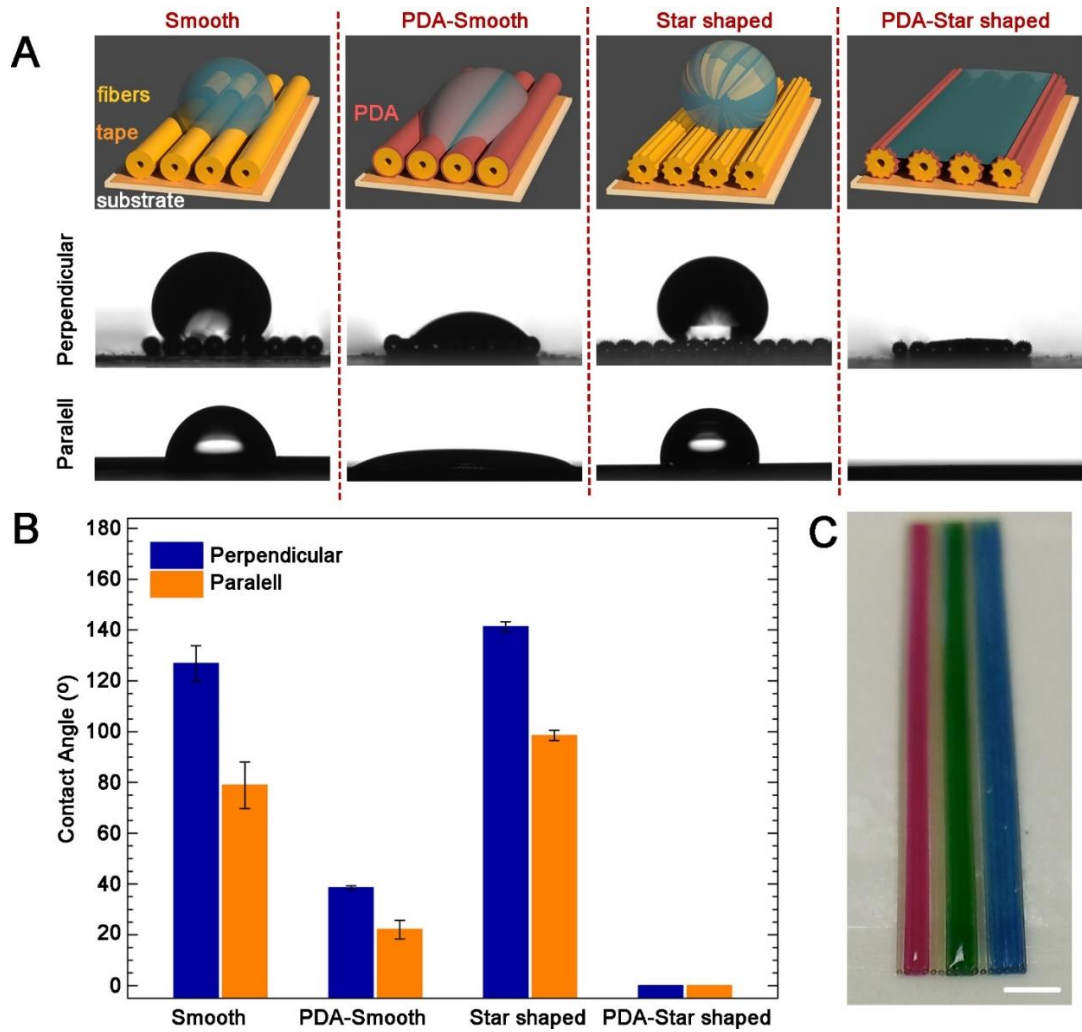


Figure 19: Extremely anisotropic wetting of star-shaped fibers. (A) Wetting behavior of fiber arrays. Fiber surfaces are prepared by simply aligning the fibers on an adhesive tape. Parallel and perpendicular corresponds to the direction contact angle measurement is taken. When there is no PDA coating, star-shaped fibers are more hydrophobic from smooth fibers due to increased roughness of the PEI surface. After PDA modification of the surfaces, both smooth and star-shaped fibers show increased hydrophilic behavior. However, water is spread to the whole length of the fiber for star-shaped fibers. (B) Contact angle measurements of fiber array surfaces. (C) A fiber array comprised of 16 fibers of length 6 cm. Dyed water of different colors is introduced to the surface (scale bar: 2 mm).

3.3.1. Water Spreading Dynamics of Fiber Arrays

The rate of capillary wicking in cylindrical geometries can be explained with Washburn's law [136]. Washburn's model estimates wicking distance to be

proportional with the square root of time. The V - groove geometry of the fibers in this study are not consistent with the assumptions under which Washburn's law is derived. Additionally, the model takes only closed-channels into consideration; either single cylindrical channels or porous bodies, therefore it would not apply for open-channel groove geometry of the fibers in this study.

However, a similar approach to open triangular geometry of the grooves yields results perfectly analogous to Washburn's equation. In the case of spreading to a triangular groove from a reservoir, the height of the liquid in the groove is approximated to be constant and the relationship between spreading distance and time is described with a square root law. Experiments with various liquids demonstrated that spreading distance 'L' is accurately proportional to square root of time ' \sqrt{t} ' for open triangular geometries [135, 136].

To see if these arguments hold for an array of star-shaped fibers, we measured spreading of liquid versus time for arrays of 500 μm , 300 μm , and 200 μm star-shaped fibers. Dyed water was introduced to the array from one end, and video of the liquid spreading was recorded with a standard digital camera (Nikon Coolpix S6400). Then the position of liquid front was measured and plotted as a function of square root of time (Figure 20). On each of the three arrays, there is a linear relationship between 'L' and ' \sqrt{t} ' with R-Square (R^2) values larger than 0.99. Therefore, spreading in star-shaped fibers agree well with previously described models for triangular or V grooves. Further, spreading speed increases with increasing fiber diameter (thus with increasing side lengths of V - grooves), which is also consistent with previous reports [134, 136].

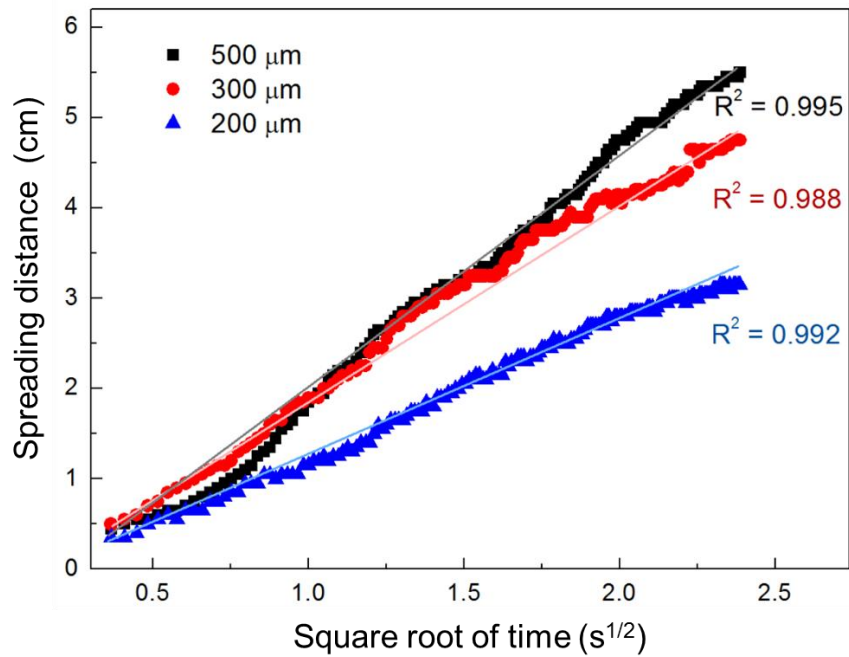


Figure 20: Spreading rates in fiber arrays with various fiber diameters (500 μm , 300 μm , and 200 μm).

3.4. Three-dimensional Microfluidic Channels

Open microfluidic channels that can control liquid flow in both lateral and vertical directions can be easily prepared using PDA coated star-shaped fibers owing to their flexibility. For instance, Figure 21A shows a curved 15 cm long open microfluidic channel which consists of five 300 μm sized fibers that successfully direct the flow of 40 μL of red colored water in its predefined path. Water filled the channel approximately in 2.5 minutes without any external influence.

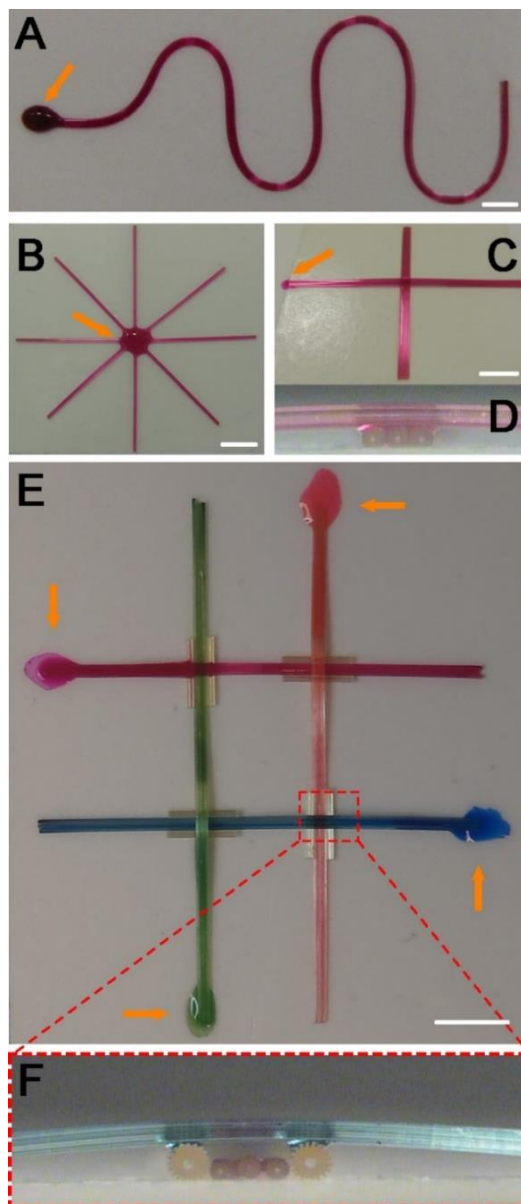


Figure 21: Construction of microfluidic networks with star-shaped fibers. (a) Spontaneous wetting is achieved in about 2.5 minutes to the whole length of 15 cm fibers aligned in a curved path (scale bar: 1 cm). Orange arrows show the point of dyed water introduction. (B) Distribution of liquid to multiple channels from single drop. Single fibers of diameter 300 μm spread the dyed water to any direction (scale bar: 5 mm). (C) Connection of microfluidic channels by stacking fiber arrays. Liquid spread on the above array is transferred to the below array (scale bar: 5 mm). (D) Shows a close up view of the connection point. (E) A three-dimensional system comprising of 4 channels crossing one another. At the intersection points, two uncoated larger hydrophobic star-shaped fibers are placed at the both sides of the below channel serve as spacers to prevent contact between below and above channels (bridge geometry). (Scale bar: 5 mm). (F) Shows close-up view of the bridge from a different angle.

The observed longer filling time for this curved channel, compared to 7 cm long fiber array mentioned above is due to its higher fiber length and curved shape. Controlling liquid spreading from a reservoir to several channels or one channel to another is needed to construct multichannel microfluidic devices. Figure 21B shows distribution of water from a reservoir to eight different channels which are composed of single 500 μm sized fibers.

In addition, we showed that using PDA-star shaped fibers, it is possible to design connection architectures. For example, when water is introduced from one end of the upper channel of two cross over channels, top channel transfers some of the water to the bottom channel (Figure 21C). The close up image of this connection (Figure 21D) demonstrates the water transfer between close contacts stacked channels. Introducing a 200 μm gap between top and bottom channels with the addition of spacers (uncoated 500 μm fibers) prevented the mixing of upper and lower liquid flows. This enables us to construct ‘bridge’ architectures that are capable of transporting liquid streams crossover another. Three-dimensional array composing of 4 channels that cross one another are constructed (Figure 3.12E). At the bridging junction, no liquid streams intermixed or intercede each other (Figure 21F). Also, we demonstrated end to end added channels can transmit water from one point to another (Figure 22).

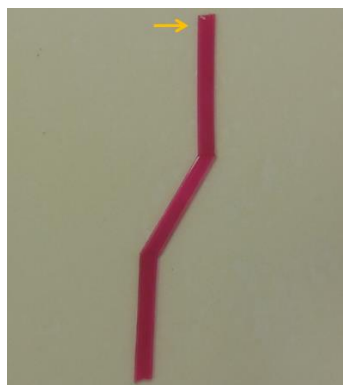


Figure 22: Demonstration of end to end added channels that can transmit water from one to another. Orange arrow shows the point of dyed water introduction.

3.4.1. Effects of Channel Length and Shape on Channel Filling Time

In order to investigate the effect of different parameter on channel filling time, we prepared four different surfaces; a 5 cm long straight fiber array, a 10 cm long straight fiber array, a 10 cm long bended fiber array with two turns, and a 15 cm long bended fiber array with four turns. We measured the water filling times of straight fiber arrays (5 and 10 cm), bended fiber array with two turns (10 cm), and bended fiber array with four turns (15 cm), which are 7 seconds, 16 seconds, 35 seconds and 2.5 minutes, respectively (Figure 23). Based on these results, we can conclude that depending on the fiber length and array shape array filling time might change from a few seconds to a few minutes. In general, with the increasing fiber length, the number of bends, and curvature radius of bends, filling time increases significantly.



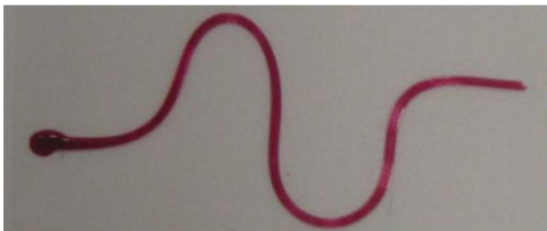
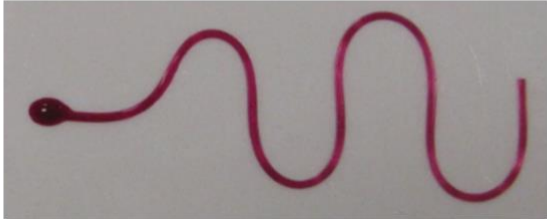
| Array | | Filling Time (s) |
|----------------|--|------------------|
| 5 cm straight |  | 7 |
| 10 cm straight |  | 16 |
| 10 cm curved |  | 35 |
| 15 cm curved |  | 150 |

Figure 23: Water (20 μ L) filling times of four different open microfluidic channels.

3.5. Microfluidics Switch Design

Switch architectures give the user ability of on-demand liquid transport; *i. e.* which and when the channels should be activated [33]. Here, we designed two different switch geometries (Figure 24). The first switch geometry is the same with the bridge geometry discussed above. We simply pressed the bridge using a sharp tip (tweezer) and provided contact between top and bottom channels, which results in immediate filling of the below channel (Figure 24A). In the second design, we constructed free-standing channels just a few millimeters above the fixed bottom channels (Figure 24B). We first fill the free-standing channels and then activate the below channels one at a time by simply bending the free-standing channels and providing a contact between top and bottom channels. All of the three switches operated successfully.

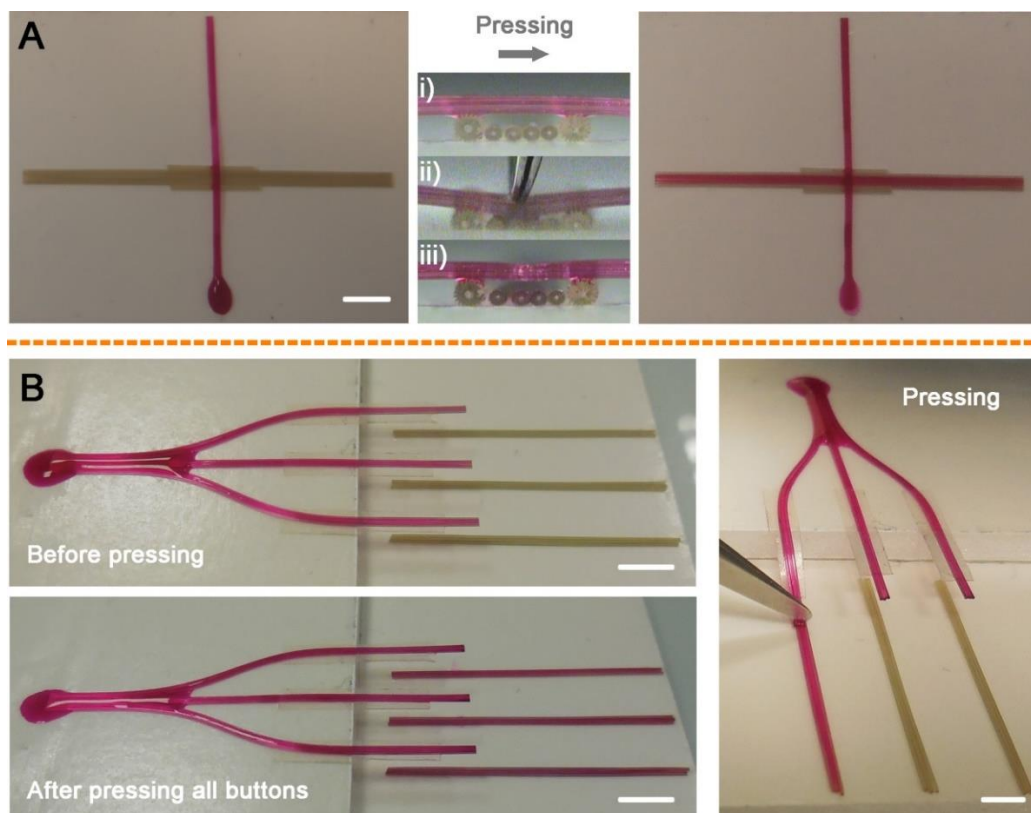


Figure 24: Switches that control water spreading. Utilizing the observed liquid transfer upon stacked fibers, a simple button mechanism is shown. (A) Initially there is no liquid at the below array, there is no intermixing between above and below arrays (i) (scale bar: 5 mm). (ii) When the above array is pressed down with a tweezer it comes into contact with the below array and spontaneous spreading begins at the below array instantaneously. (iii) After release of the above array it relaxes back to its initial position and there is no further liquid transfer between channels. At the end stage water is distributed to the whole length of the below array. (B) Interplanar button mechanism. This example shows a button for liquid transfer between planes. Spontaneous spreading begins instantaneously by contact with the already wet array (scale bar: 5 mm).

3.6. Flexibility of the Channels

Flexibility of the PEI fibers enables us to construct microfluidic channels on complex three-dimensional objects. Figure 25A shows the 15 cm long rolled microfluidic channel (comprising of four 200 μm thick PDA star-shaped fibers) around a glass rod. The array can transport 50 μL of colored water along the channel approximately in 6 minutes. This example demonstrates that surface textured fiber based open

microfluidic channels can also operate against gravitational force. Furthermore, microfluidic channels can be prepared on flexible substrates which can operate under bending. For instance, Figure 25B shows three bended microfluidic channels, prepared on a polycarbonate film, which are filled with differently colored water portions.

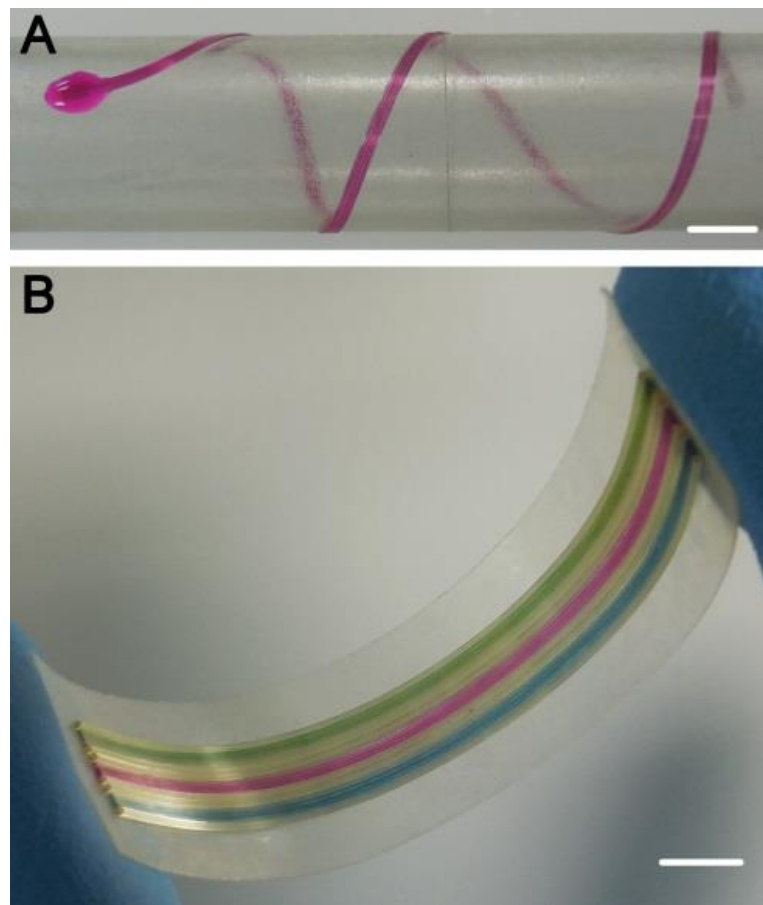


Figure 25: Fiber based microfluidics unrestricted with planar based systems. Since fibers are flexible, the observed anisotropic wetting behavior can be achieved on any surface. (A) Spontaneous wetting on fibers of length 15 cm rolled around a glass tube (scale bar: 5 mm). (B) Microfluidic channel array on a flexible surface. The array consists of about 120 microchannels on 12 fibers, uncoated 500 μm star-shaped fibers are added in between the coated 300 μm fibers for avoiding the delivery of liquid to the wrong array (scale bar: 5 mm).

Another example of a microfluidic channel demonstration on a three-dimensional object was given in Figure 26 which shows liquid climbing a ramp.

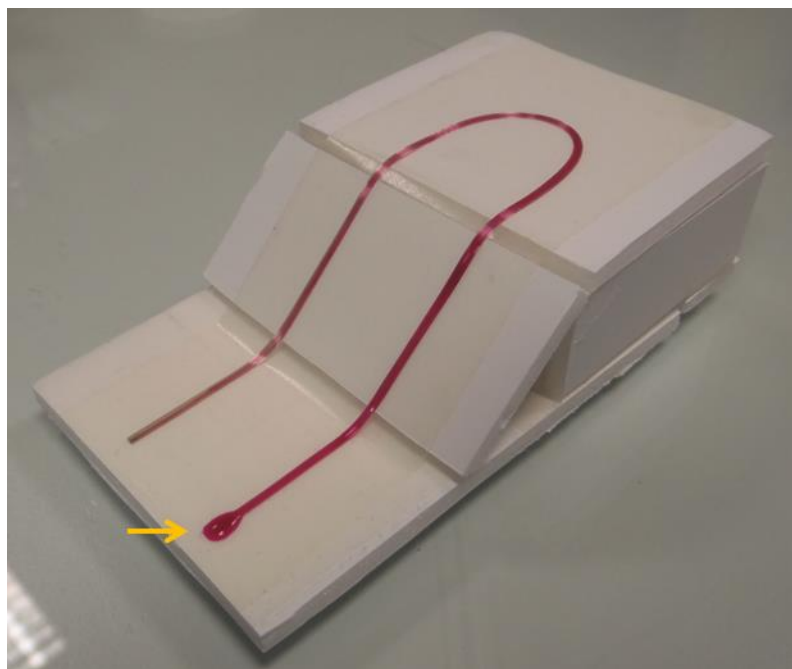


Figure 26: An example of a microfluidic channel demonstration on a three-dimensional object which shows fluid climbing a ramp. Orange arrow shows the point of dyed water introduction

3.7. Protein Assay as a Proof of Concept

As a proof of concept demonstration that our method is suitable to fabricate disposable and low-cost medical test kits, we prepared a protein assay for detection of human serum albumin (HSA) which is the most abundant protein in human blood. The assay is based on the color change of the bromophenol blue (BPB) dye in the presence of HSA. We used filter paper as detection zones, where it is possible to observe the color change upon protein addition, as paper is an intrinsically hydrophilic and macroporous material that can absorb definite volume of water depending on its size [38]. In a simple experiment, we demonstrated that paper in contact with the fiber microfluidic channels can easily wick the liquid on the channels (Figure 27A).

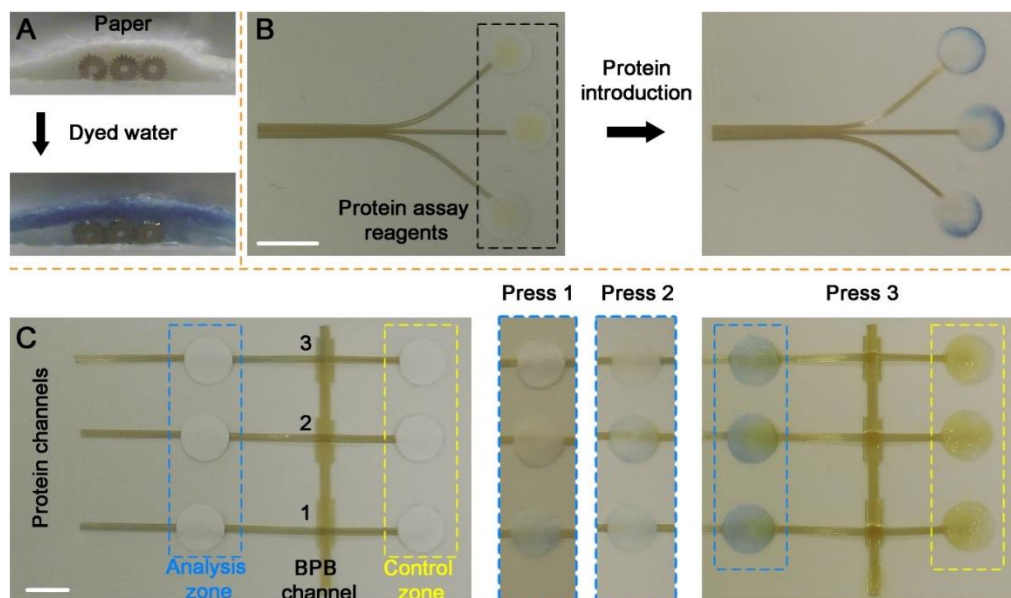


Figure 27: Protein assays. (A) Demonstration of water transfer from a microfluidic channel to a piece of filter paper. (B) A protein assay composing of three detection zones. Upon addition of HSA immediate color change occurred at all detection zones (scale bar: 1 cm). (C) A protein assay composing of three analysis and control spots and three switches. After activation of all switches color change was observed in analysis spots (scale bar: 5 mm).

In the first colorimetric assay (Figure 27B), we constructed a microfluidic channel (composing of six 300 μm diameter fibers) which is then divided into three sub-channels and connected to circular filter paper pieces (6 mm in diameter) at the end of each channel. Then, 2 μL of protein assay reagents (0.1 mg mL^{-1} BPB in glycine buffer (10 mM) at pH 2.3) were dropped onto the paper detection zones and dried under ambient air. After addition of 20 μL of HSA solution (5 mg mL^{-1} in PBS, pH 7.4) to the main microfluidic channel, color of the detection zones changed from light yellow to blue, within a minute. After this simple demonstration, we designed a more complex protein assay which consists of 1 BPB channel, 3 protein channels, 3 switches, 3 detection zones and 3 control zones (Figure 27C). In this design, one can select the channel on which the experiment will be performed. It is important to note that, after activating the switches, both control and detection zones are filled with BPB solution; on the other hand protein solution only fills the detection zones. Initially, the BPB channel was filled with 50 μL of BPB solution. Then, we added 4 μL of HSA solution (10 mg mL^{-1}) to the first channel and activate the first switch. Immediately after

pushing the switch we observed a blue color in detection zone (color of BPB in the presence of HSA) and light yellow color in the control zone.

In addition, a quantitative HSA analysis was demonstrated (Figure 28) using the assay. We observed that assay can easily identify HSA concentrations of between 0.2 and 5 mg mL⁻¹.

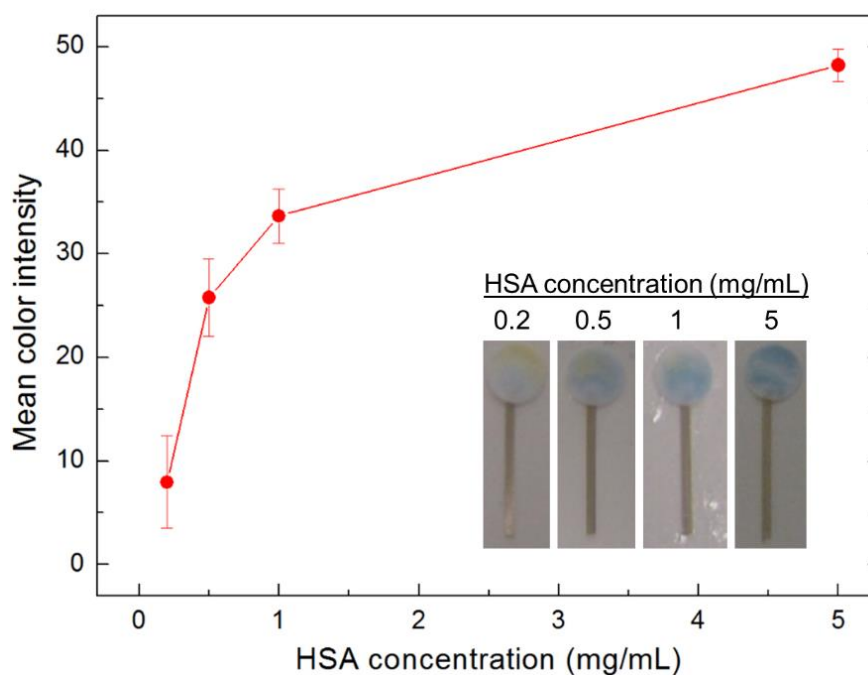


Figure 28: Concentration dependent colorimetric response of the array. All experiments were performed in triplicate. Mean color intensities were calculated by averaging the change in the RGB values (compared to white) of randomly selected pixels. Inset shows the photographs of the color change in the assays after protein introduction.

It essential to note the mechanism of collection fluid as a reservoir by the paper. The protein solution can only fills the detection zones because there is a gap on the fiber channel under the control spots (Figure 29).

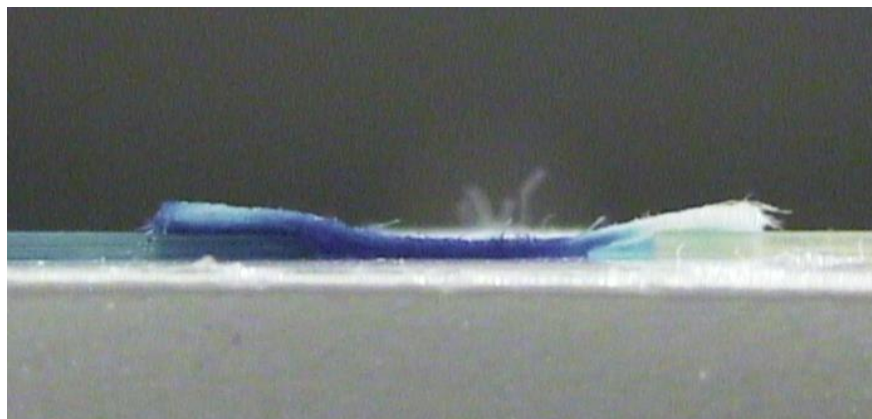


Figure 29: Side view of a gap covered with a piece of paper, similar to the control spots in the protein assay. Although the two channels are connected over the gap with a piece of paper, blue colored water (introduced to the channel at left) did not transfer to the other channel (right channel).

Although the two channels are connected over the gap with a piece of paper, protein solution was not transferred to the control channel since this small amount of (4 μL) protein solution is completely absorbed by the paper. We repeated this procedure for the other two channels and observed that all channels worked properly; the color changes of analysis and control spots are clearly distinguishable (Table 2).

Table 2: RGB (Red, green and blue) values collected for 10 individual pixels for each analysis and control spot. RGB color model assigns a numerical value to each of the three primary colors, red, green and blue, in order to define each possible color as a function of the primary colors. The yellow shade of analysis spots and the blue shade of control spots were captured by a conventional scanner and RGB values were extracted by a commercial image editing software.

| Analysis1 | R | G | B | Analysis2 | R | G | B | Analysis3 | R | G | B |
|------------------|----------|----------|----------|------------------|----------|----------|----------|------------------|----------|----------|----------|
| Pixel #1 | 237 | 242 | 201 | Pixel #1 | 231 | 232 | 162 | Pixel #1 | 214 | 224 | 189 |
| Pixel #2 | 233 | 239 | 229 | Pixel #2 | 226 | 233 | 200 | Pixel #2 | 219 | 232 | 225 |
| Pixel #3 | 212 | 230 | 242 | Pixel #3 | 210 | 226 | 215 | Pixel #3 | 213 | 230 | 237 |
| Pixel #4 | 212 | 231 | 245 | Pixel #4 | 202 | 221 | 228 | Pixel #4 | 207 | 225 | 239 |
| Pixel #5 | 210 | 228 | 252 | Pixel #5 | 194 | 220 | 237 | Pixel #5 | 202 | 227 | 247 |
| Pixel #6 | 212 | 227 | 255 | Pixel #6 | 211 | 219 | 255 | Pixel #6 | 201 | 223 | 246 |
| Pixel #7 | 223 | 240 | 250 | Pixel #7 | 201 | 224 | 238 | Pixel #7 | 201 | 222 | 241 |
| Pixel #8 | 212 | 230 | 242 | Pixel #8 | 206 | 221 | 228 | Pixel #8 | 213 | 230 | 237 |
| Pixel #9 | 214 | 234 | 245 | Pixel #9 | 209 | 231 | 244 | Pixel #9 | 201 | 220 | 235 |
| Pixel #10 | 213 | 224 | 246 | Pixel #10 | 207 | 234 | 251 | Pixel #10 | 191 | 217 | 250 |
| | | | | | | | | | | | |
| Control1 | R | G | B | Control2 | R | G | B | Control3 | R | G | B |
| Pixel #1 | 254 | 253 | 248 | Pixel #1 | 250 | 250 | 198 | Pixel #1 | 249 | 250 | 242 |
| Pixel #2 | 255 | 255 | 250 | Pixel #2 | 254 | 253 | 205 | Pixel #2 | 252 | 254 | 232 |
| Pixel #3 | 254 | 253 | 223 | Pixel #3 | 253 | 247 | 197 | Pixel #3 | 254 | 255 | 237 |
| Pixel #4 | 254 | 254 | 220 | Pixel #4 | 250 | 238 | 188 | Pixel #4 | 253 | 250 | 215 |
| Pixel #5 | 254 | 250 | 221 | Pixel #5 | 245 | 237 | 188 | Pixel #5 | 254 | 254 | 220 |
| Pixel #6 | 254 | 250 | 221 | Pixel #6 | 253 | 254 | 214 | Pixel #6 | 254 | 253 | 223 |
| Pixel #7 | 255 | 255 | 234 | Pixel #7 | 254 | 249 | 207 | Pixel #7 | 255 | 255 | 231 |
| Pixel #8 | 255 | 255 | 229 | Pixel #8 | 255 | 250 | 202 | Pixel #8 | 255 | 255 | 231 |
| Pixel #9 | 254 | 254 | 216 | Pixel #9 | 255 | 250 | 212 | Pixel #9 | 254 | 252 | 227 |
| Pixel#10 | 245 | 241 | 206 | Pixel#10 | 255 | 253 | 214 | Pixel#10 | 253 | 255 | 233 |

Chapter 4

Anisotropic Fibers for Non-wetting Surfaces

Anisotropic non-wetting is the tendency of drops to move along a single preferred direction on a surface without wetting it [70, 72, 119]. This unidirectional droplet repellency occurs on many natural surfaces for various purposes; for instance, autonomous self-cleaning of lotus leaves, radial outward propulsion of droplet on butterfly wings, aquatic locomotion of water-strider legs, and efficient rain water collection on rice and bamboo leaves [85, 86, 138–141]. This remarkable display of droplet guidance on biological surfaces is achieved using advanced surface features including ordered microscale morphology, high surface roughness at the micro- and nanoscales, and a hydrophobic surface chemistry [141]. The realization of artificial surfaces with anisotropic non-wetting capability is inspiring for the development of self-cleaning surfaces, droplet microfluidics, droplet micro-reactors for precise chemical and/or nanomaterial synthesis, and droplet transport at precise volumes [49–51]. Several methods have been developed to fabricate functional anisotropic surfaces. For example, photolithography is utilized to pattern re-entrant structures such as microgrooves and pillars on various materials (e.g., silicon and polymer) [119, 143] and UV treatment on stretched polydimethylsiloxane (PDMS) surfaces which upon releasing forms microscale ripple (wrinkle) pattern [124, 144]. Other techniques of interest are polymer imprinting [144], plasma etching [145], electrospinning [146], and femtosecond laser micromachining [148, 149]. In addition, fibers are interesting alternative materials for harnessing liquid-solid interactions. Tubular or ribbon shaped micro-fibers were fabricated for microfluidic applications using thiol click chemistry and surface modification with reactive groups [150, 151]. However, there are some

limitations posed to the global utilization of these methods such as cost-effectiveness, feasibility in large scale production, flexibility of the product, and applicability to large area. Thus, demand for facile and robust fabrication techniques to address these limitations has increased in recent years.

In the previous chapter, mass production of surface textured polymer micro-fibers that have perfectly aligned micro-structures on their surfaces using a well-established thermal drawing method was reported [151]. Moreover, in this chapter, surface textured polycarbonate (PC) fibers that are identical to the PEI textured fibers is presented to highlight the novelty of thermal drawing technique. With this technique, we are not restricted to material choices, and therefore several engineering polymers can be produced. In addition, we demonstrated the preparation of large-area anisotropic non-wetting polymer surfaces using hierarchy structural roughness on both the PEI and PC fibers with hydrophobic surface chemistry and nanometer scale roughness. The hydrophobic surface chemistry and nanometer scale roughness was introduced over the micro-scale V - grooves on the fibers by coating with organically modified silica (ormosil) nanoparticles [152]. Functional anisotropic surfaces of different architectures were constructed by fixing the fibers on paperboard, polymer, and glass substrates using double sided adhesive tape.

The scalability of the fibers and optional nanoparticle surface modification enable construction of variety of fiber surfaces with different wetting characteristics. The wetting phenomena on the fibers correlate well with the classical wetting theory of surfaces. Wenzel model explains the homogeneous wetting regime on rough surface when liquid is in intimate contact with a solid surface. Roughness increases the surface area of a solid which enhances hydrophobicity. Also, Wenzel droplets are found to be highly pinned. The geometry of any ascribed roughness on a solid surface increases the hydrophobic nature of the surface. Even though surface chemistry plays a crucial role in wetting, it cannot generate contact angle (CA) as high as 160° without the existence of surface roughness. We demonstrated droplet transport using sticky hydrophobic and roll-off superhydrophobic surfaces, droplet guiding on track surfaces,

and a simple protein assay with colliding droplets as examples of droplet manipulation with alternative surface designs for microfluidics application.

4.1. Fabrication of Surface Textured Polymer Fibers

Star-shaped fibers were produced from V - grooved preform by thermal drawing method under appropriate mechanical stress and temperature profiles. Polymer Fibers are thermally drawn at elevated temperature - higher than their glass transition (T_g) [41–44, 154]. In-situ diameter control of fiber is achieved by precisely tuning mechanical stress (*i. e.*, increasing or decreasing the motor speed. PEI or PC fibers of several meters length which preserved the V - grooves at varying diameters (ranging from 200 μm to 500 μm) were produced (Figure 30a). SEM images of the PEI fibers show the star-shaped cross sections and parallel grooves of the fibers with 200 μm and 500 μm diameters in Figure 30b-i and ii. Even the smallest fiber of 200 μm size preserved the V - grooves at the micro-scale; the groove widths and heights are about 30 and 20 microns, respectively, at a 150-fold size reduction of the preform.

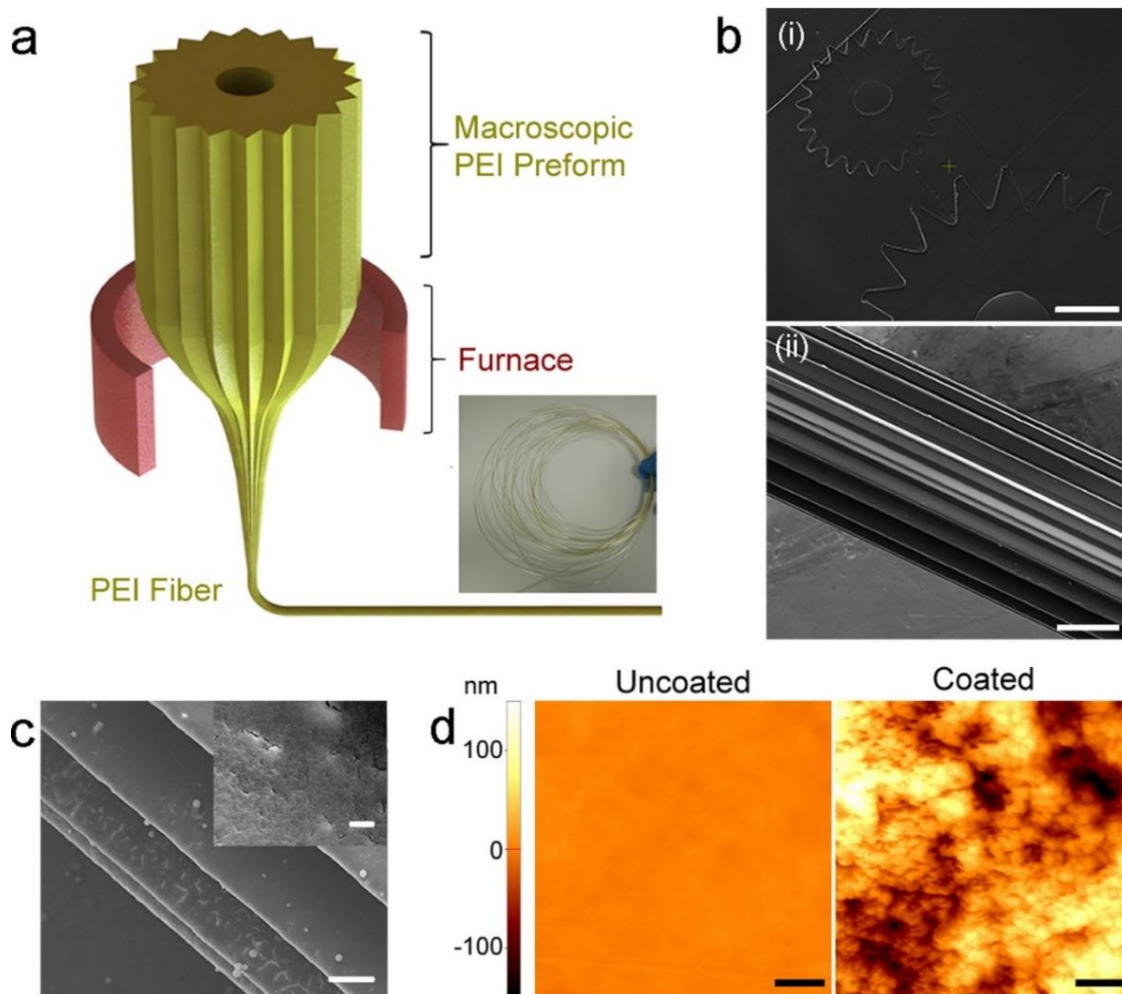


Figure 30: Fabrication scheme of V - grooved PEI microfibers and surface modification with nanoparticle coating. (a) Thermal drawing of V - grooved microfibers from the macroscale star-shaped PEI preform. (b) SEM micrograph illustrating cross-sections of (i) 200 μm and 500 μm sized fibers with 20 parallel V-grooves (scale bar: 100 μm), and (ii) 500 μm size fiber showing the textured microgrooves that form microchannels which extend along its entire length (scale bar: 100 μm). (c) SEM micrographs of a coated fiber showing homogeneously coated nanoparticles (scale bars: 15 μm and 1.5 μm (inset)). (d) AFM micrographs of uncoated and nanoparticle coated fibers. Nanoparticle coating introduces a random nanoscale roughness on the ordered microscale roughness of the fiber surfaces (scale bars: 0.5 μm).

PEI fibers with smooth surfaces were fabricated to compare the groove effect on wettability of the fibers Figure 31a and b. The fiber drawing method is facile and applicable to many engineering polymers. Also, see Figure 31c for SEM image of V-grooved PC fibers similar to PEI fibers.

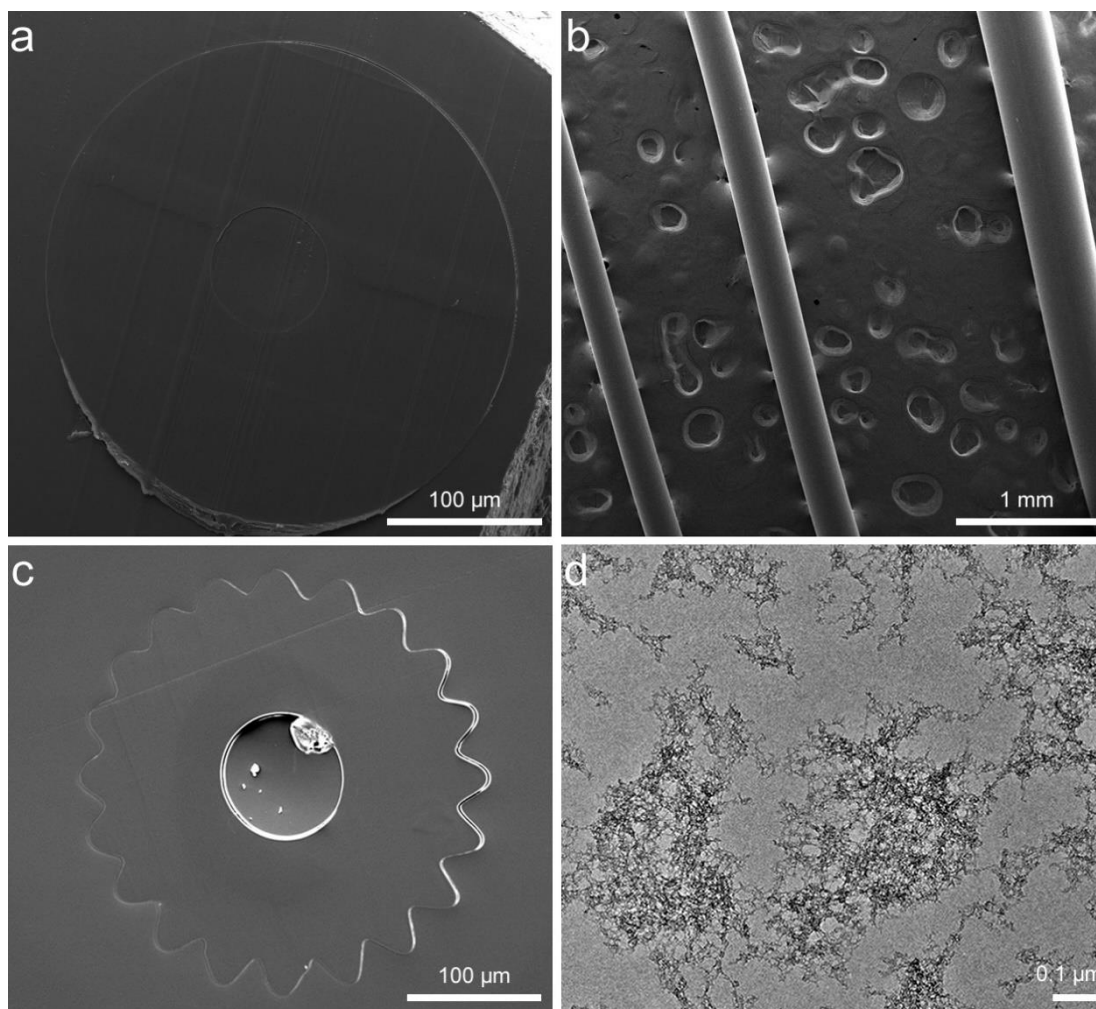


Figure 31: SEM image of (a) cross-section of smooth PEI fiber with a diameter of 300 μm , (b) 200 μm , 300 μm , and 500 μm of smooth PEI fibers, (c) cross-section of V – grooved fiber of 300 μm diameter, and (d) TEM micrograph of interconnected ormosil colloidal nanoparticles (with sizes of about 10 nm) forming a porous network layer.

4.2. Introduction of Nano-scale Roughness on the Fiber Surfaces

Ormosil colloidal nanoparticles were prepared according to previous study by Adem et al. [152]. Initially, 1 mL MTMS was dissolved in 2 mL DMSO, and then 0.5 mL of oxalic acid solution (10 mM) was slowly added to the mixture and stirred for 30 min. Then 0.42 mL of ammonia solution (25%) and 0.19 mL of water in 5 mL of DMSO were added, and the solution was stirred for 15 min again. In the end, the solution was left for gelation at 25 °C. The gel is typically formed in about one hour. Approximately 20 mL of methanol was added onto the prepared gel and incubated for at least 6 hours at 25 °C to remove the DMSO and unreacted chemicals. This procedure was repeated 4 times to ensure complete removal of DMSO and chemical residues. Methanol (12 mL) was added onto the gel and sonicated using an ultrasonic homogenizer for 45 s at 20 W power to obtain ormosil colloid which is suitable for nanoporous thin film deposition.

4.2.1. Ormosil Nanoparticle Coating

Hydrophobic ormosil nanoparticles were spray-coated on the fiber surfaces to introduce an additional nano-scale roughness using spray gun Lotus BD-132A; nozzle diameter 0.3 mm, and fluid cup capacity 7cc filled with ormosil nanoparticle solution. Coating time was 2–3s with pressurized nitrogen gas passing through the gun at 2 bar (Figure 32). After coating the fibers, they were left to dry at room temperature. The ormosil colloidal nano-particles were homogeneously distributed, forming a continuous porous layer within the asperities as seen in the SEM micrographs (Figure 30c). Transmission electron microscope (TEM) imaging shows that ormosil colloidal nano-particles (with sizes around 10 nm) interconnect to constitute a porous network (Figure 31d). Surface roughness (RMS) of PEI smooth fiber increased from 3 nm to about 50 nm when coated with ormosil as measured from AFM micrographs (Figure

30d). After spray coating, a hierarchical surface structure with micro-scale grooves and nanoparticles were established on the fiber surface.

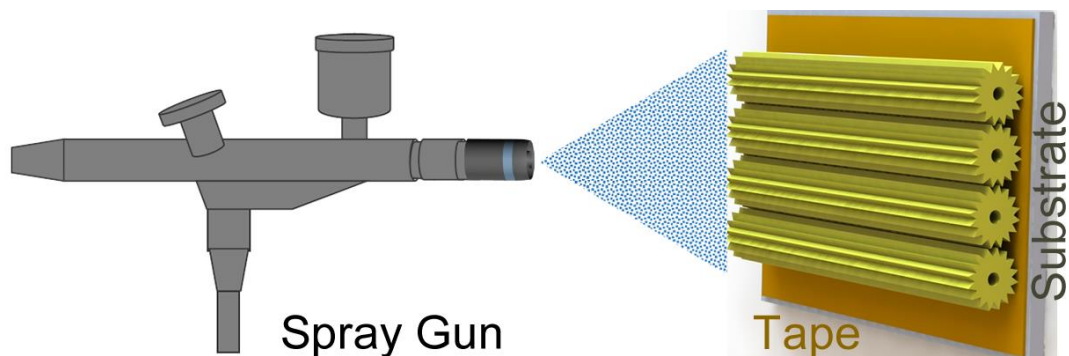


Figure 32: Schematic illustration of ormosil nanoparticle spray coating on fiber surface. Spray gun is loaded with diluted ormosil solution, and then a surface is brought into close proximity (approximately 30cm away from the gun) with the gun. Ormosil gel was diluted in methanol solution. Pressurized nitrogen gas passes through the gun at 2 bar and the solution is sprayed onto fibers for about 2 – 3 s at ambient atmosphere. The sample is let dried at room temperature.

4.3. Surface Characterization of Fiber Arrays

Arrays of fibers with different surface properties were prepared to study anisotropic wetting/non-wetting behavior of the fibers. Uncoated smooth, uncoated grooved, nanoparticle coated smooth, and nanoparticle coated grooved fibers of PEI and PC (each 8 cm in length and 300 μm in diameter) were fixed firmly on glass substrates using a double sided adhesive tape to form surfaces (Figure 33a).

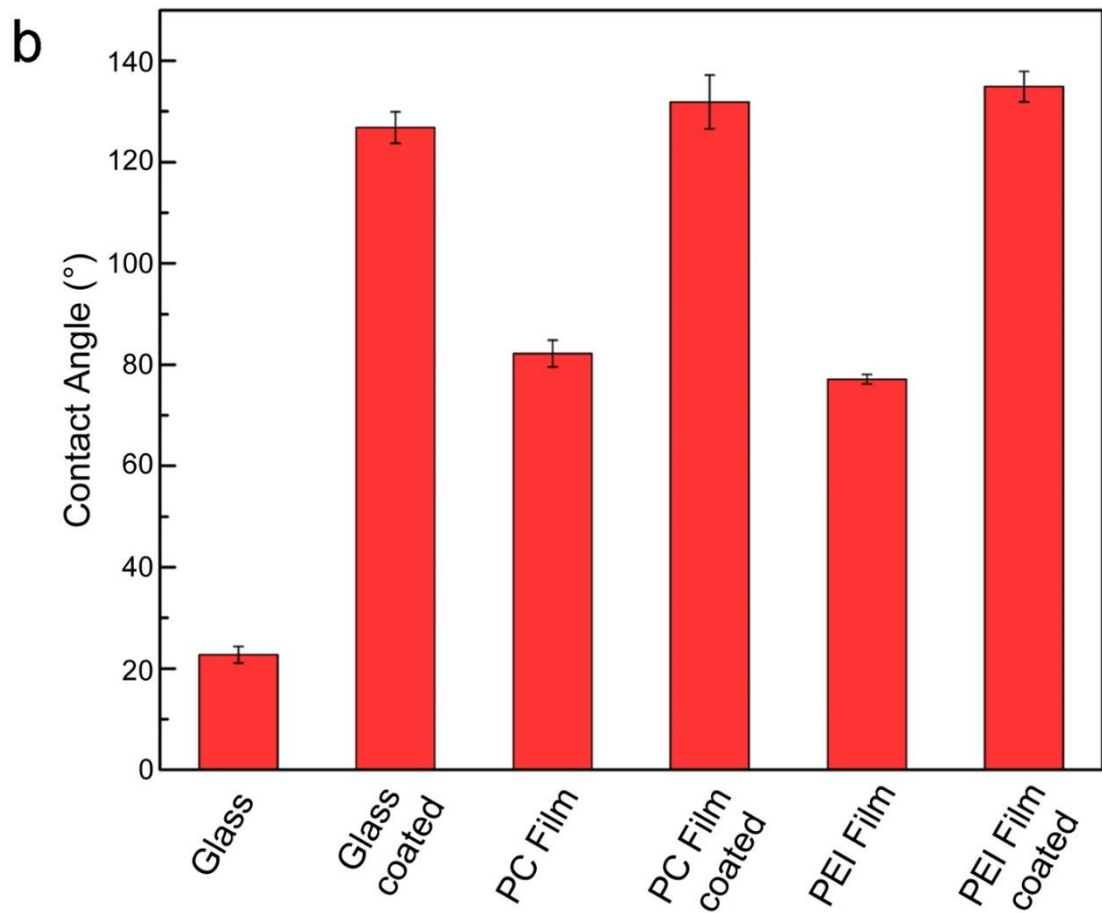
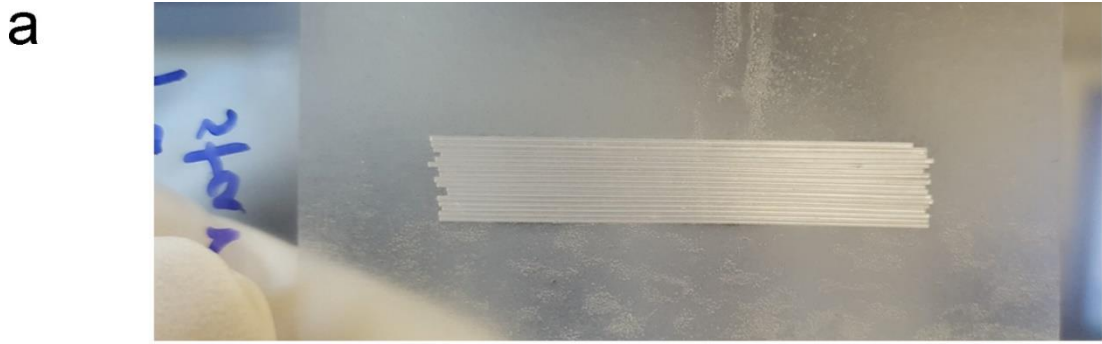


Figure 33: Model construction of surfaces for CA measurement on glass substrate using double sided tape (a), and CA values measurement on different substrates including glass, PC film, and PEI film and their coated surfaces (b).

Static CA of water droplets ($4 \mu\text{L}$) were measured from directions parallel and perpendicular to fibers' orientation at ambient environment (Figure 34a). Wenzel, Cassie, and intermediate state of wettings were observed on the fiber surfaces [76, 77].

Water droplet resting on the uncoated smooth PEI fiber surfaces was in Wenzel state and fills the spaces between the fibers (Figure 34b-i). After surface modification with ormosil coatings, fiber surfaces gained additional nano-scale roughness, and the CA values increased in both parallel and perpendicular directions. Even though the smooth PEI fiber surface was coated, the droplet resting on the surface was neither in Wenzel state nor in Cassie state (Figure 34b-ii). The droplet exist in the intermediate state. The uncoated grooved PEI fiber surface has two very ordered roughness scales ascribed by the parallel grooves and the fibers and therefore hydrophobicity is enhanced on this surface compared to the coated and uncoated smooth PEI surfaces. Also, CA was increased in both parallel and perpendicular directions because of the groove morphology. On the uncoated grooved surface, water cannot fill the spaces between the fibers, but can penetrate the micro-grooves structures on the fibers (Figure 34b-iii). However, the nanoparticle coated grooved fibers demonstrated hydrophobicity with enhanced CA in both parallel and perpendicular directions due to the introduced nano-scale roughness apart from their surface chemistry. Composite of liquid/air/solid is realized with a droplet resting on the surface with pseudo spherical shape. Air is trapped beneath the droplet and minimizing the contact area between solid and liquid. It is observed that water neither fill the space between the fibers nor penetrate the grooves of the fiber due to the combined effect of surface chemistry and multi-scale roughness (Figure 34b-iv). In addition, evident of the contribution of nanoroughness was provided to show the effectiveness of nanoparticle coating on the fiber grooves by measuring CA of glass substrate, uncoated and coated polymer (PC and PEI) films as reference (Figure 33b). The superhydrophobicity on the coated fibers is arised by nano-scale roughness introduced by the coatings and fiber surface chemistry. It is also directional so that droplets roll easily in one direction similar to the anisotropic non-wetting behavior of rice leaves.

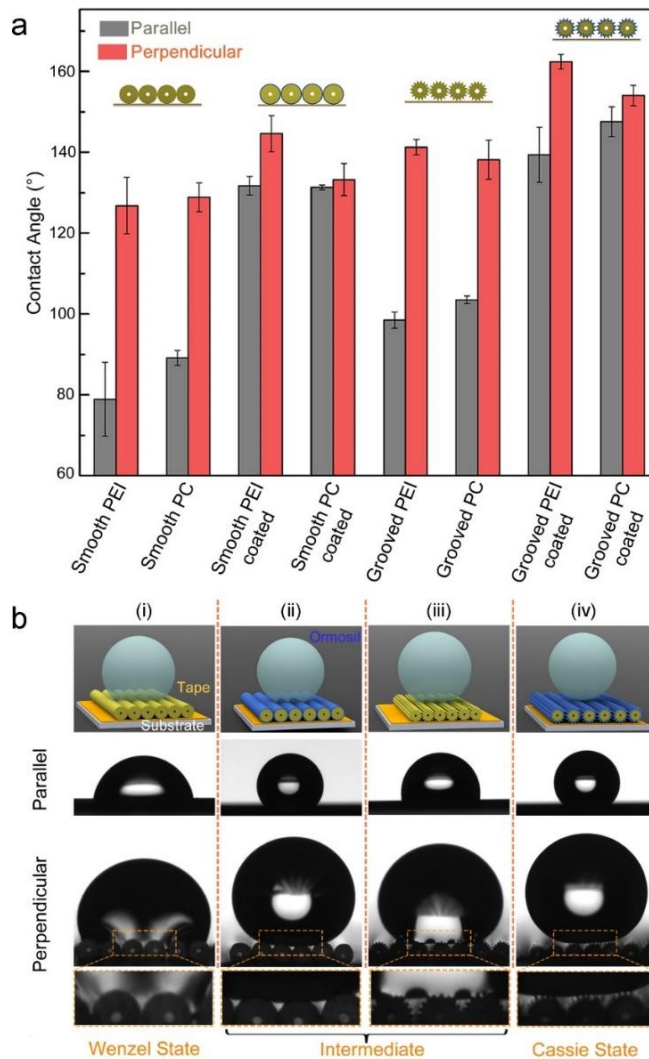


Figure 34: (a) Contact angle measurements of fiber array surfaces (with each fiber 8 cm in length and 300 μm in diameter) with 4 μL water droplets. The measurements were taken from parallel and perpendicular directions, which correspond to the directions with respect to the fiber orientation of the surfaces. (b) Photographs showing the wetting behavior on PEI fiber surfaces. (i) The droplet on uncoated smooth fibers is in the Wenzel state, where spaces within the fibers are filled with water as seen in the inset. For nanoparticle coated smooth or uncoated grooved fiber surfaces, the droplets are in an intermediate state between Cassie and Wenzel states. (ii) The smooth fiber surface is wet, but the water cannot penetrate the in-fiber spaces for the array of coated smooth fibers. (iii) For the case of uncoated grooved fibers, water filled the micro-channels within the microscale grooves yet cannot wet the spaces between the fibers as seen from the inset. (iv) The droplet is in the Cassie state on nanoparticle coated grooved fibers. The water droplet rests on the tips of triangular protrusions on the fibers and water cannot penetrate the grooves or the spaces between fibers.

4.3.1. Comparison of Anisotropic Behavior on Fiber Arrays

The fibers (grooved or smooth) are principally a roughness scale with pristine anisotropic behavior when they form an array. The aligned fibers and parallel grooves introduce a very ordered roughness hierarchy. The uncoated smooth PEI and PC fiber surfaces exhibit CA difference of 48° and 39° respectively. By definition, CA difference is the change in the parallel and perpendicular CA measured on the fiber surfaces. The CA difference reveals the anisotropic wetting property of the fibers due to the very ordered surface topography induced by the parallel aligned grooves on the fiber. Relative to the smooth fibers, anisotropy was observed on the grooved PEI and PC fibers with greater CA. When compared to the grooved fiber, water droplet spreads isotropically on the bare PEI and PC films. Moreover, in expense of the nanoroughness introduced by coating, the anisotropy of the coated grooved PC and PEI diminished and the difference of CA in parallel and perpendicular direction reduced tremendously. On the basis of wetting resistance considering a drop resting on the coated grooved PEI and PC fiber arrays, relatively the highest CA of 162° was observed on the coated grooved PEI fiber compared to 154° on coated grooved PC fiber array (Figure 34a). In addition to the magnified wetting property of the surfaces, a substantial anisotropy is revealed alongside directional superhydrophobicity. In the sense of anisotropy, the coated grooved PEI fiber revealed greater tendency of directional nonwetting within the entire range of the fiber arrays and therefore it is preferably utilized in the proceeding part of the work that followed.

Variation in groove dimension does not affect the surface wetting property of the fibers dramatically. Combination of microgroove with nanoparticle improve the nonwetting behavior significantly. When the fibers are not coated with nanoparticle, the contribution to hydrophobicity is mainly from the intrinsic surface chemistry of the polymer fiber and the grooves. Dimension of the fibers varies on polymer fibers with different diameters as a result of the reduction factor of the original preform during drawing. For example, fiber with $500\ \mu\text{m}$ diameters have grooves with $50\ \mu\text{m}$ height and $70\ \mu\text{m}$ distance between grooves. Fibers with $300\ \mu\text{m}$ size have grooves

with 30 μm height and 50 μm distance apart. CA of the uncoated grooved PEI surfaces reveals that, variation in the groove dimension does not affect the CA significantly (Figure 35a). However, for coated grooved PEI fibers, the anisotropy is greater on both 200 and 300 μm size fibers than on 500 μm size fibers (Figure 35b).

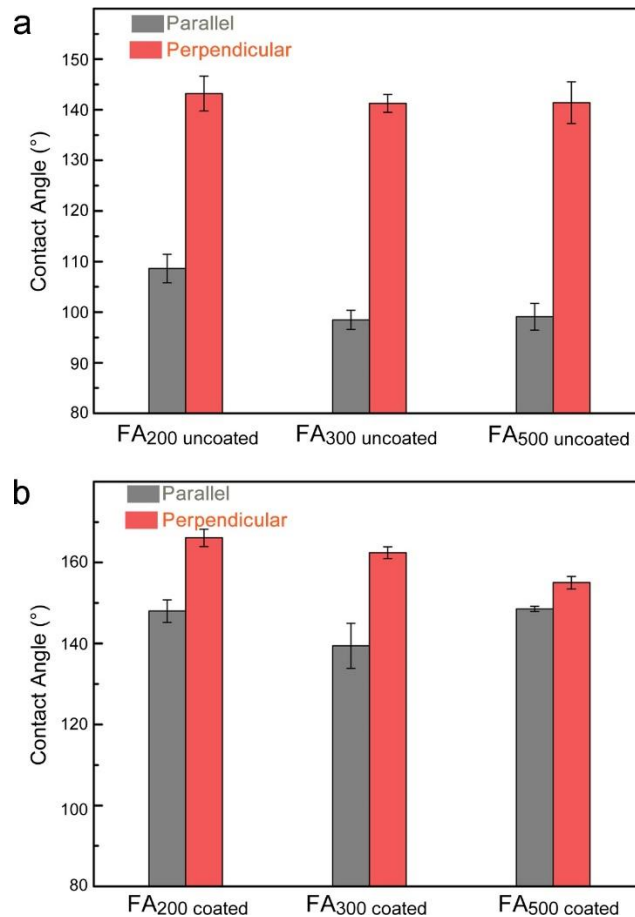


Figure 35: Comparison of groove dimension on the basis of anisotropic behavior. (a) Uncoated 200 μm , 300 μm , and 500 μm grooved PEI fiber arrays, and (b) coated 200 μm , 300 μm , and 500 μm grooved PEI fiber arrays.

We investigated rice leaf-like directional roll-off of water droplets from the fiber surfaces with roll-off angle measurements from parallel and perpendicular directions using 8 μL of water droplets. Surfaces and tracks with a variety of topographies were designed by employing nanoparticle coated grooved fibers with varying diameters (200 μm , 300 μm and 500 μm) as building blocks. Initially, three different fiber arrays

of 200 μm , 300 μm and 500 μm sized grooved fibers coated with ormosil nanoparticles were constructed and labeled as FA_{500} , FA_{300} , and FA_{200} (Figure 36a). All of these three surfaces were slightly anisotropic with a roll-off angle differences around 5° between parallel and perpendicular directions. This difference in roll-off angle ($\Delta\theta = SA_{\perp} - SA_{\parallel}$) is referred to as the anisotropy of the surfaces, and is shown for each surface in Figure 36b. To improve the anisotropic roll-off behavior, combinations of different sized fibers were used to obtain surfaces that demonstrate greater anisotropic non-wetting behavior. The fibers with 500 μm , 300 μm and 200 μm sizes were used to prepare a parabolic fiber array (track), which is labeled as ' $\text{FA}_{\text{Track1}}$ ' (Figure 36c-i). This surface pattern demonstrated a greatly enhanced anisotropic behavior with anisotropy of about 20° . Another track pattern (labeled as ' $\text{FA}_{\text{Track2}}$ ') was prepared using 500 μm and 200 μm sized fibers (Figure 36c-ii). The anisotropy was about 20° for this surface. In addition, we studied the effect of water droplet size on anisotropic roll-off behavior using $\text{FA}_{\text{Track2}}$ (Figure 36d). Both the roll-off angle and the $\Delta\theta$ decrease with increasing droplet volume. The ordered hierarchical roughness of the fibers and the grooves become less effective with increasing droplet volumes. However, the roll-off value is smaller in parallel direction for all droplet volumes, which demonstrates that anisotropic non-wetting behavior is retained. On the other hand, when droplet volume is too small, it pinned to the surface. For instance, droplet of 2 μL size pinned to the surface in perpendicular direction but not in the parallel direction. Furthermore, we compared the roll-off phenomenon on nanoparticle coated smooth and grooved fibers to clarify the surface behavior difference contributed by the on-fiber groove structures. Figure 36e-i and ii show a droplet rolling off a 300 μm coated grooved fiber surface at a roll-off angle of 14° , and a droplet pinned to a coated smooth fiber surface at a tilting angle of 90° . Red colored water droplets are distributed on a flexible substrate as an array (Figure 36e-iii).

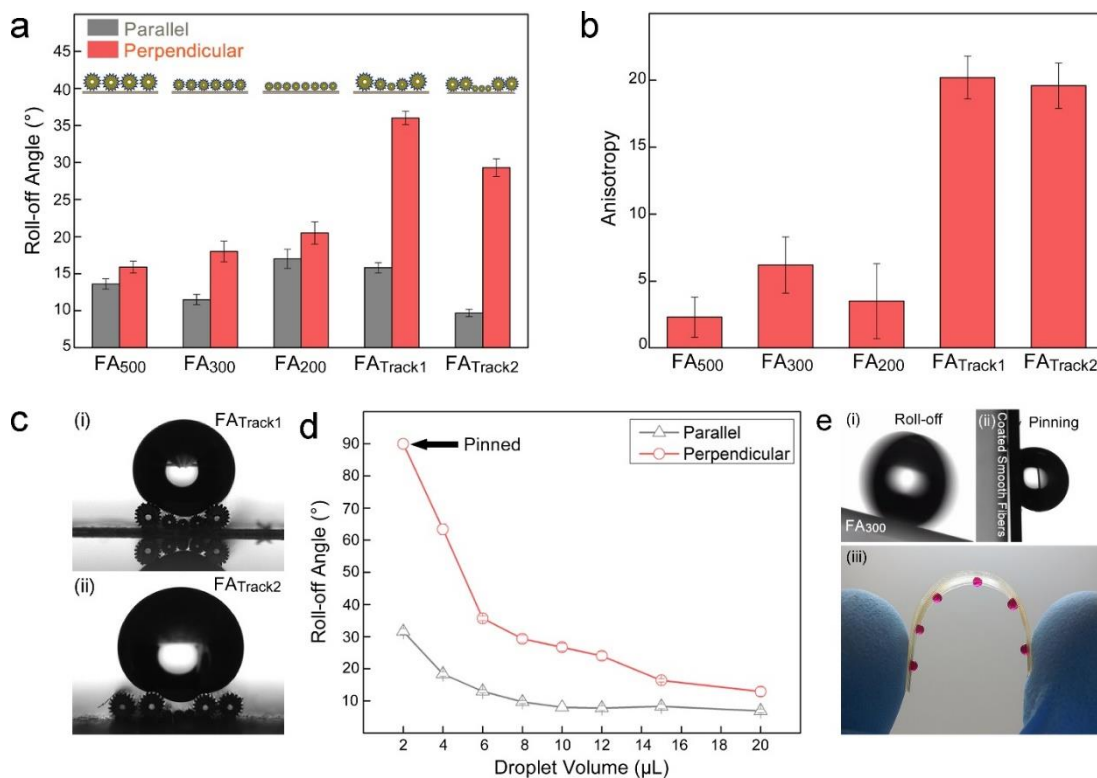


Figure 36: (a) Roll-off angle values measured on ormosil coated grooved fiber arrays (FA) formed by fibers with diameters of 500 μm , 300 μm and 200 μm (FA500, FA300 and FA200), and their combinations (FATrack1 and FATrack2). (b) Anisotropy ($\Delta\theta = \text{SA}_{\perp} - \text{SA}_{\parallel}$) of the fiber arrays, showing enhanced anisotropic non-wetting behavior on FATrack1 and FATrack2 surfaces. (c) Photographs of droplets on FATrack1 and FATrack2. (i) FATrack1 is a parabolic array of 500 μm /300 μm /200 μm /300 μm /500 μm fibers. (ii) FATrack2 is a channel composed of 500 μm x2/200 μm x3/500 μm x2 array. (d) The relation between roll-off angle and droplet volume on FATrack2. Roll-off angle decreases with increasing droplet volume in both parallel and perpendicular directions. However, roll-off angle is higher in the perpendicular direction for all droplet volumes, which demonstrates the anisotropic non-wetting behavior of the surface. (e) Roll-off and adhesive properties of nanoparticle coated smooth and grooved fiber surfaces. (i) Anisotropic roll-off in parallel direction on the FA300 surface tilted at 14°. (ii) The droplet remains pinned to a nanoparticle coated fiber surface with 300 μm smooth fibers even when the surface is tilted at 90°. (iii) Pinned droplets on a flexible substrates for conceptual demonstration.

4.4. Droplet Manipulation on Fiber Arrays and Tracks

Using the surface textured fibers as building blocks, we prepared surfaces for micro-droplet transport, guiding, and mixing. Figure 4.8 shows the transport of water droplets and their controlled mixing using arrays of textured fibers. In Figure 37a, steps of

droplet transport from a roll-off superhydrophobic surface (array of 300 μm coated grooved fibers) to a sticky hydrophobic surface (array of 300 μm coated smooth fibers) was demonstrated. When the droplet sitting on the roll-off surface was gently squeezed with the upper sticky hydrophobic surface, it pinned to the sticky surface after relaxation. Since the fibers are flexible, it is possible to prepare fiber arrays on arbitrary surfaces. For instance, Figure 37b demonstrates controlled water droplet mixing using a sticky hydrophobic fiber array constructed on the fingertip of a nitrile glove. A person wearing this glove can manually transport a water droplet (blue) sitting on a roll-off superhydrophobic surface to the array of sticky hydrophobic fibers on her/his finger (Figure 37b-i). The droplet can be carried on the fingertip and merged with another droplet (red) by gently touching the second droplet (Figure 37b-ii and iii).

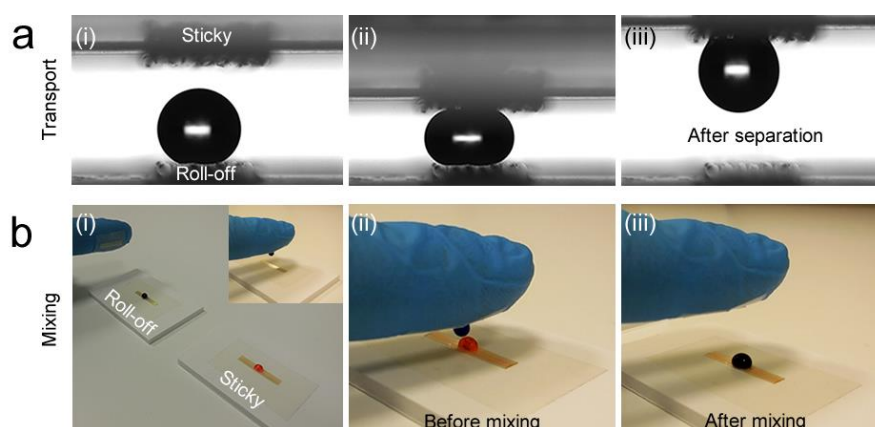


Figure 37: Droplet transport and mixing. (a) Snapshots of a 4 μL suspended droplet on the roll-off superhydrophobic fiber surface (array of 300 μm coated grooved fibers). The droplet is transferred from the superhydrophobic surface to the sticky surface (array of nanoparticle coated 300 μm fibers) upon bringing the two surfaces in close proximity. (b) Droplet transportation with fiber surfaces prepared on arbitrary surfaces. (i) An array of 300 μm coated smooth fibers was prepared on the fingertip of a nitrile glove. By gently touching the resting blue dyed water droplet (on the 300 μm nanoparticle coated grooved fiber surface), it was transferred to the fingertip. (ii) The blue droplet was carried on the fingertip and was contacted with the red dyed droplet resting on a sticky surface manually. (iii) The resulting droplet after mixing of the initial red and the blue droplets.

We constructed a curved 8 cm long $\text{FA}_{\text{track2}}$ path to demonstrate droplet manipulation for open microfluidic channels. Water droplets (8 μL) were guided

successfully along the curved path by tilting the surface to about 10° . Snapshots in Figure 38a show the positions of the water droplet at different time intervals on the track. The water droplet was guided within the channel without leaving the designed path until the end of the track.

Lastly, we demonstrate a proof of principle protein assay based on droplet coalescence on a linear track with one side slightly raised to make an angle of 11° with the substrate. A $9\ \mu\text{L}$ colorless droplet of human serum albumin (HSA) protein solution ($5\ \text{mg mL}^{-1}$ in PBS, pH 7.4) was rolled from the slope formed by the track and collided with the $8\ \mu\text{L}$ yellow droplet of bromophenol blue (BPB) dye ($0.1\ \text{mg mL}^{-1}$ BPB in glycine buffer (10 mM) at pH 2.3), as shown in Figure 38b-i and ii. The droplets coalesced into a larger droplet (mixture of HAS and BPB solutions) on the track. A color change of the resulting droplet was detected immediately, and yellow color of BPB changed to blue completely in 8 seconds after the coalescence (Figure 38b-iii).

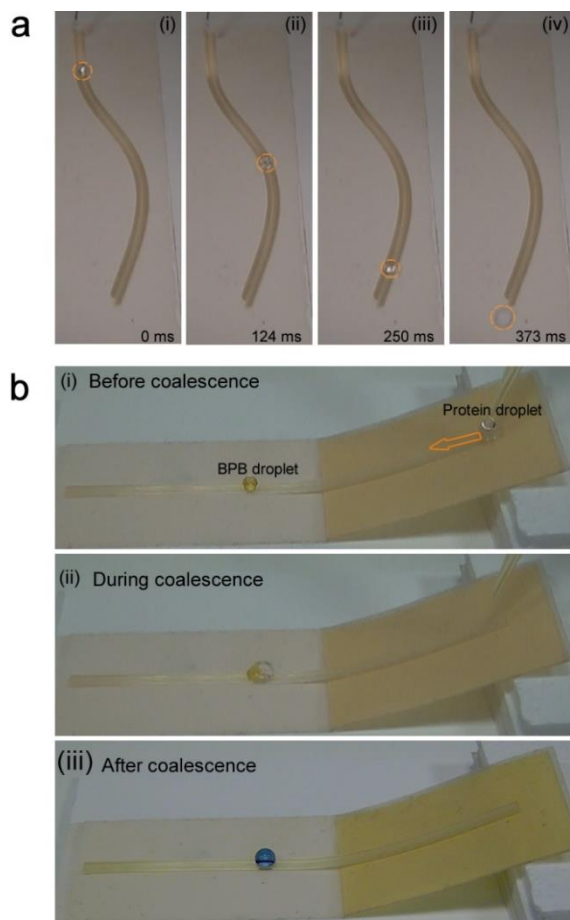


Figure 38: (a) Snapshots of a droplet rolling on the curved fiber track (FAtrack2) taken with a high-speed camera. Water droplet followed the curved path outlined by the fibers at a roll-off angle of around 11° . (b) A droplet based protein assay for colorimetric detection on linear fiber tracks. (i) Dispensing yellow BPB and colorless protein solution ($8 \mu\text{L}$ and $9 \mu\text{L}$, respectively). (ii) The instant of the droplet collision. (iii) Color change after coalescence of the two droplets. The yellow color of BPB solution changed to blue after mixing with the protein solution.

Chapter 5

Surface Treatment by UV/Ozone

Among various surfaces modification methods, UV/Ozone is a powerful source for modifying surface properties of diverse materials. This method has been explored for more than a decade in the electronic industries to clean contamination on materials including glass, silicon, metal, and polymer. UV/Ozone can be adapted to deliberately modify materials for surface functional applications. It is easy and fast to clean or modify surfaces through UV/Ozone exposure. Samples are irradiated with UV light from a medium pressure mercury lamp which generate ozone. The UV light generated are of two different wavelengths, 185 and 254 nm respectively. In general, the exposure time is between seconds to several minutes. In 1972, Bolon and Kunz reported the use of UV light to depolymerize a variety of photoresist polymer [154]. The UV 185 nm wavelength is absorbed by oxygen and thus ozone is generated. UV 185 nm wavelength is very crucial in the disintegration process. However, the UV 254 nm wavelength is not absorbed by oxygen, rather it is absorbed mostly by hydrocarbons and ozone. In principle, the absorption of 254 nm UV by ozone is responsible for the annihilation of ozone in the chamber during the experiment. Therefore, ozone is being formed and destroyed at the continuously. Atomic oxygen which is a very strong oxidizing agent is an intermediate product of both generation and annihilation processes of ozone [156, 157].

This technique is currently being used to remove organic impurities from surface. Hence, in this chapter, we utilized UV/Ozone treatment to enhance surface wettability of polycarbonate (PC) polymer films and fiber. It is very important to reduce the contact angle of the PC surface to improve adhesion ability of biological materials. PC is chemically inert which makes it suitable for biological study. It has low surface

energy. The effect of UV light on PC is investigated by AFM, XPS, and contact angle (CA). The use of UV/Ozone treatment helps reduce the modification time of polymer fiber for directional nonwetting surfaces. In chapter 3 and 4, we employed PDA and ormosil to achieve enhanced surface properties on the fiber. We obtained superhydrophilic and superhydrophobic surfaces after the surfaces are modified. Here, by exposing the polymer surfaces to UV light the loosely bonded impurities are removed and functional hydrophilic groups are created. UV light activates the surface of the polymer and then create new functional groups such as OH, and –OOH [158–165].

5.1. Experimental Section

Thermoplastic polycarbonates (AJEDIUM; 100 μm thickness and 35 cm width, RESIN – ULTEM 1000-1000) were cut into small pieces 4X4 cm and washed in ultrasonic bath for 5 minutes in isopropanol. The polymer films were mounted on a glass slide by using double sided tape. Polycarbonate samples were placed in the UV cabinet (NOVASCAN PSD-UV - Benchtop UV-Ozone Cleaner) for exposure at a distance approximately 2 cm away from the UV lamp (Figure 39).

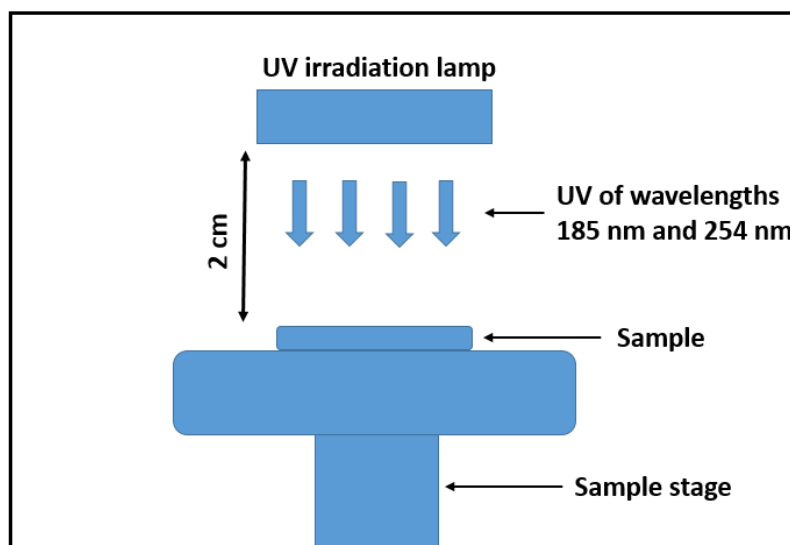


Figure 39: Scheme of UV cabinet for UV/Ozone treatment of polycarbonate surfaces.

In the UV cabinet described above, PC polymer films were positioned right under the UV irradiation for surface treatment. Chemical modification of the PC surfaces is the reason for the improve wettability. The surfaces behave differently due to higher surface energy. It is observed that the chemistry of the surface changes since the UV irradiation generates atomic oxygen which oxidizing agent.

In order to investigate the basics of the chemistry behind the hydrophilic modification in elaborative way, the untreated and UV/O treated surfaces were analyzed using X-Ray photoelectron spectroscopy (XPS). Survey analysis showed that untreated PC surface structure was composed of approximately 12% oxygen, 86% carbon, and 2% nitrogen. However, chemical composition of PC surfaces that were treated with UV/O for 30 minutes was approximated to 34% oxygen, 63% carbon, and 3% nitrogen, respectively (Figure 40a and b). This result indicates that as a result of UV irradiation, some of the generated atomic oxygen chemically bind to carbon and form carbon-oxygen moieties with higher binding energies. Figure 40c and d show the high resolution C1s spectra of the untreated and 30 minute UV/O treated PC surfaces. Peaks at 285 and 286.5 eV correspond to the C-H/C-C and C-O-H groups and the very low intensity satellite π - π^* interaction (291.0 eV). In Figure 40d, decrease in C-H bond intensities is seen upon treatment revealing the formation of C=O group which has

hydrophilic property. The formation of this hydrophilic group is attributed to the breaking down of the bonds between C-C and C-H owing to the irradiated UV that generated ozone which was also destroyed at high photon energy. The available oxygen source during this process is air.

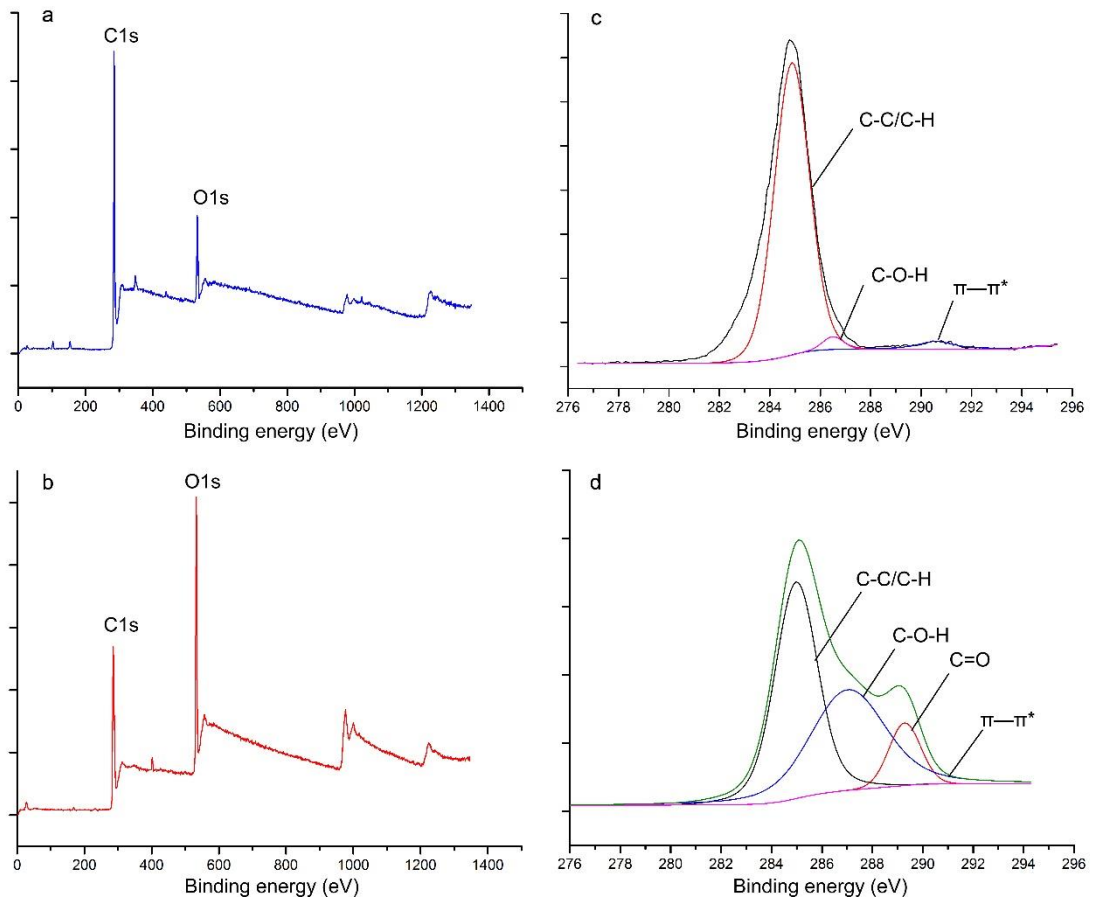


Figure 40: (a) and (b) X-ray photoelectron spectroscopy (XPS) survey spectra of PC surfaces before and after UV/O treatment for 30 minutes. (c) and (d) high-resolution C1s spectra of the PC surfaces before and after UV/O treatment for 30 minutes.

Roughness of the PC surface does not change significantly. It appears there exist surface reconstruction after the PC films were treated with UV/O (Figure 41). It is worth to note that up until now the surface are treated in an ambient atmosphere. Even the oxygen that are used up during the process is the atmospheric oxygen. The combined chemical and physical properties makes the PC films more hydrophilic. With regard to the fact that, hydrophilicity of a surface increases with structural effect.

The roughness level of UV/O treated and untreated PC film was measured by using tapping mode in Atomic Force Microscope (AFM). Calculated roughness is a measure of the Root Means Square (RMS) of the surfaces presented in Figure 41, which is 5.08 and 4.31 nm for the untreated and treated films respectively.

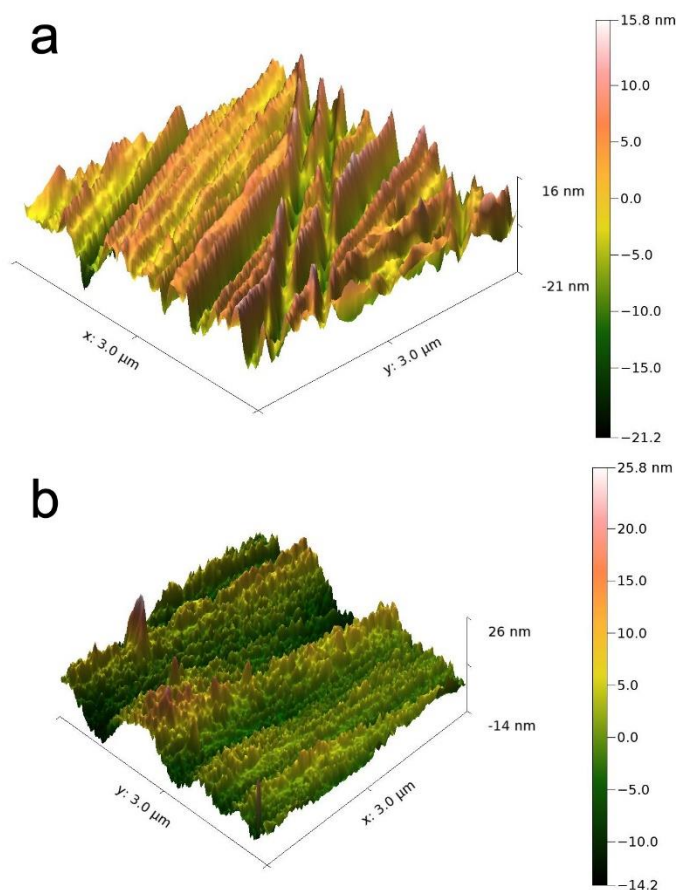


Figure 41: AFM micrograph of untreated and UV/O treated PC films. The treatment time was 30 minutes. Change in the roughness contour is seen as the surface reconstructed after the treatment.

To ascertain the change in surface energy of the materials after UV/O treatments, a static contact angle (WCA) of the surface was measured using contact angle meter (OCA 30, Dataphysics). 4 μL water droplets were used for the measurements and the contact angle were analyzed with Laplace-Young fitting. It turned out that the surface CA diminishes as the surface was chemically modified. CA of 19° was recorded for 30 minute treatment of PC film in Figure 42a, whereas the CA of untreated PC film

was 83° (Figure 42b). CA of several polymer films were also measured to discern more insight on how UV/O treatment affect the surface property of PC polymer. PC polymer is proven to be UV/O sensitive with substantial reduction in contact angle similar to other polymers such as PEI, polyethersulfone (PES), and polyester (PEST).

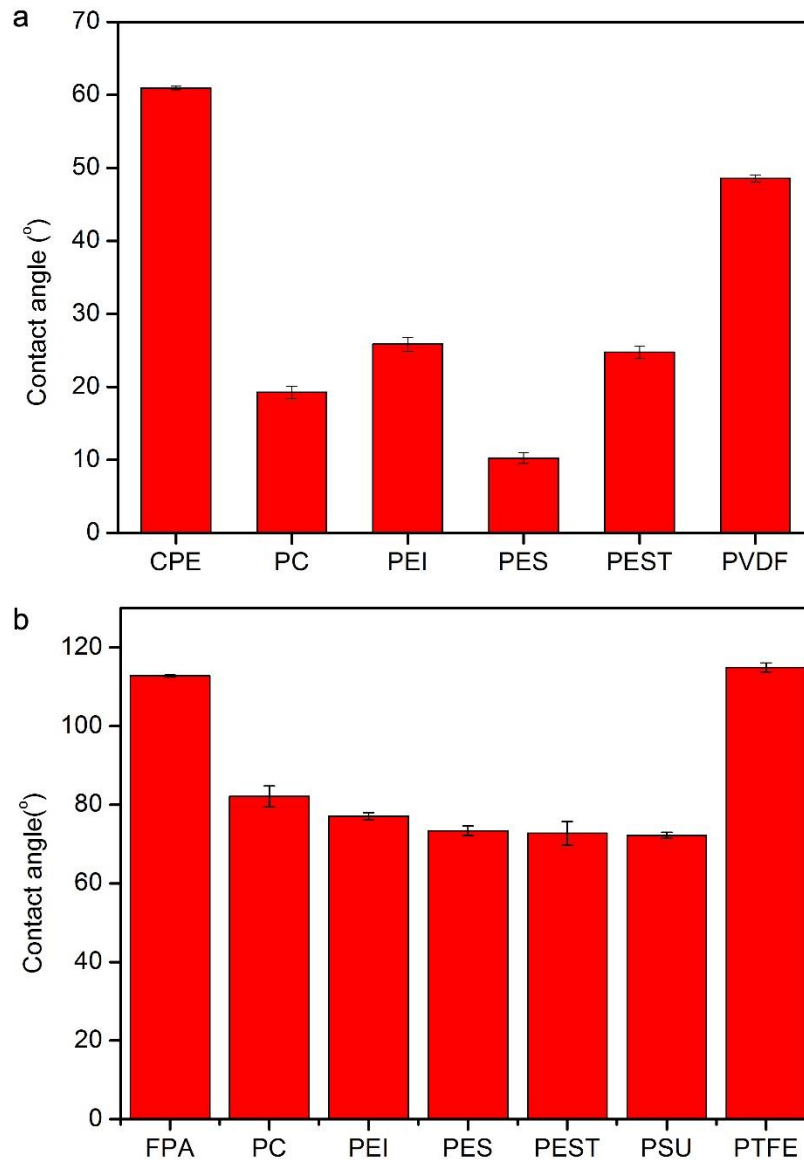


Figure 42: Contact angle measurements of different type of polymer materials. (a) UV/O treated and (b) untreated surfaces.

Addition of oxygen in excess reduces the treatment time sharply to almost 2/3 of the initial exposure time. For instance, 19° of CA was achieved in 30 minutes

treatment. However, CA of 22° could also be achieved only in 10 minutes when there is excess oxygen in the chamber to facilitate the ozone generation. Excess oxygen is delivered through a hose to the chamber at a 2 bar pressure prior to experiment. Since there are more oxygen supply during the reaction in the chamber, more interaction of oxygen and UV light takes place. A comparison CA measurement between ambient air treatment and excess oxygen treatment is presented in Figure 43.

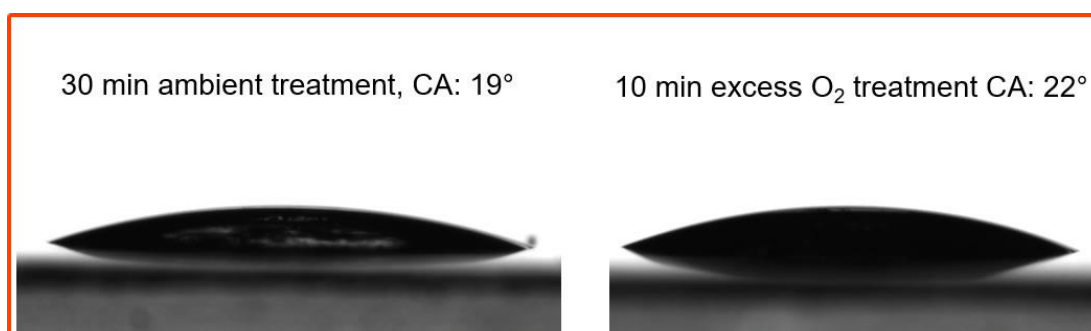


Figure 43: CA comparison between of PC film treated in an ambient atmosphere for 30 min and in excess O₂ for 10 min.

Effect of UV/O treatment under ambient temperature is studied by conducting series of experiment at different time intervals. It is observed that CA suddenly drops to a critical value during the first minute of UV exposure and then level to a steady range. Under atmospheric condition, the critical time to reach CA less than 20° was about 15 minutes. After this time interval, the polymer surface as saturated with the necessary hydrophilic groups responsible for the reduced CA. So, 15 minute was the optimum time to treat PC polymer film. Figure 44a shows the time dependent CA measurement of PC film at ambient condition. In addition, effect of excess oxygen on different polymer materials during treatment is presented in Figure 44b. Nearly zero CA was observed on PC, PES, and PSU were treated excess oxygen for 30 minutes. The surfaces of these polymers are superhydrophilic after the treatment. Liquid readily spread on them due to their higher surface energy.

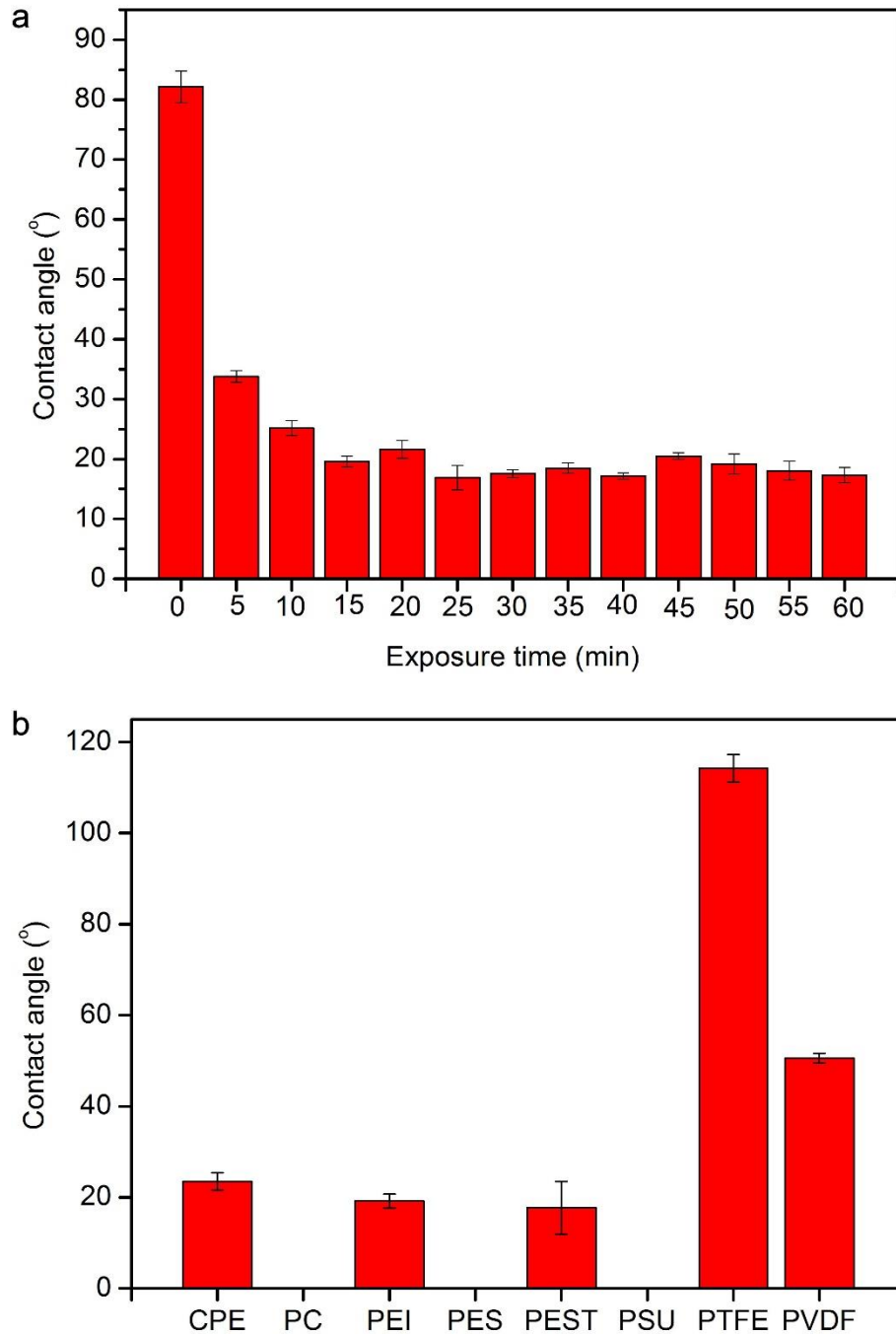


Figure 44: (a) Exposure time dependent of CA measurement on PC film and (b) Effect of excess oxygen on different polymers.

To determine the minimum time require to make the PC films superhydrophilic, CA measurement with increasing time interval was measured and in every successive experiment addition oxygen was flowed in to facilitate the interaction with the irradiated UV light (Figure 45).

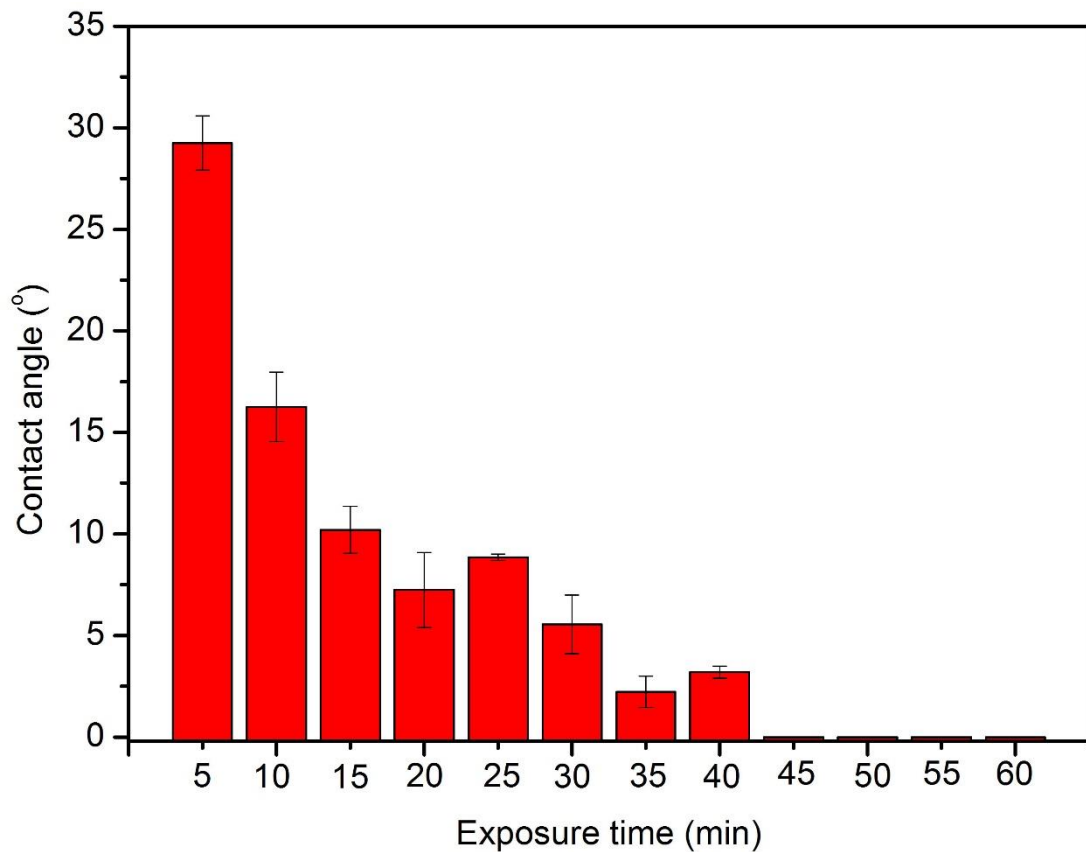


Figure 45: CA Measurement in time during treatment of PC with excess oxygen applied.

5.2. Surface Modification of Hierarchical PC Fiber by UV/Ozone

Polymer fibers have greater tendency to be employed for microfluidics and functional applications. This chapter is devoted to the design of fiber with unique structure comprising three scale roughness. We fabricated PC polymer fiber composed of multiscale V-grooves to enhance its intrinsic wetting behavior. A special tool box was used to structure the preform similar to the grooved fibers used in the preceding chapters. Only that in this case two stages of grooving in lathe was performed. CA on the multistructured fiber was high, but water droplet pinned to the surface. The

reported fiber has the highest CA value intrinsically. In Figure 46, SEM images of the multiscale rough fibers are shown.

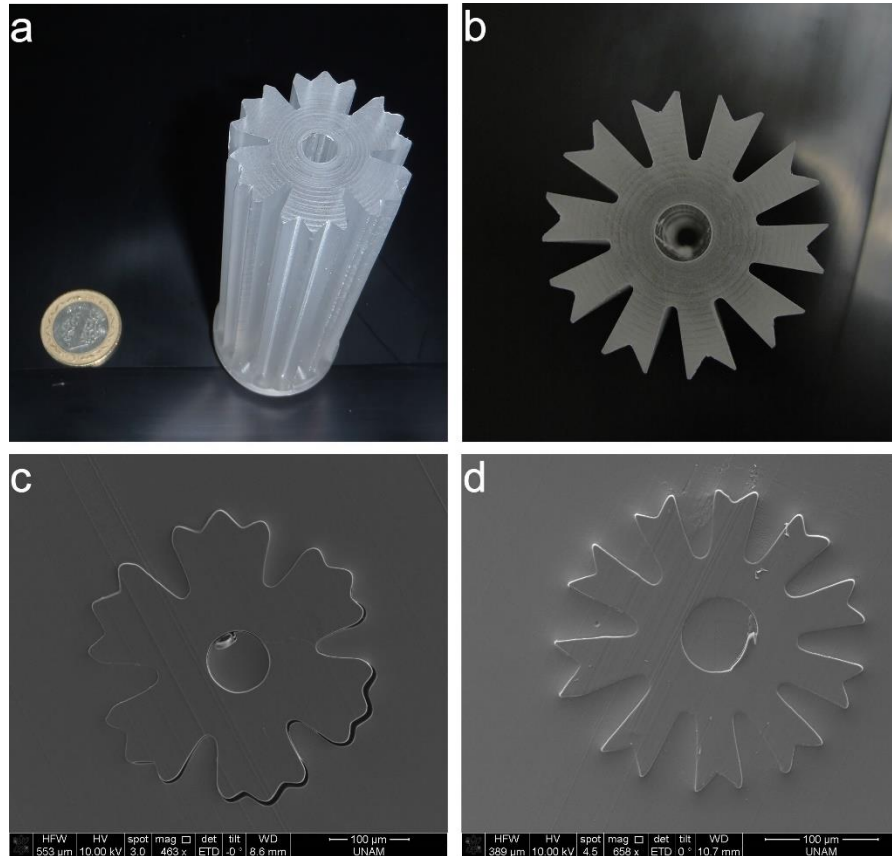


Figure 46: Multiscale rough PC polymer preform (a, b) and thermally drawn PC fiber with preserved multiscale roughness (c, d).

The intrinsic water CA on the multiscale fiber was about 150° . Although the surface has higher CA, when UV/O treatment was applied, the droplets spread entirely on the surface with nearly 0° CA. The reason underlying the perfect wetting on the fiber is the chemical modification by UV irradiation. Nevertheless, the V-grooves on the surface play a crucial role in the wetting behavior. Depending on the desire application, the grooves can be modified for optimal adhesion property for DNA hybridization and/or bacterial localization.

Chapter 6

Conclusions

6.1. Conclusion

We demonstrated that PDA functionalized surface textured polymer fibers can be utilized as universal building blocks to produce microfluidic devices that are; i) not restricted to conventional planar geometries, ii) mechanically flexible and robust, and iii) easily adaptable for new designs. Each of the 20 micro-channels on the star-shaped fibers was spontaneously filled with water upon contact due to capillary action, which enables free-standing microfluidics on the fibers. Several microfluidic device components including channels, connections, bridges and switches were designed by arrays of star-shaped fibers, which enable three-dimensional and programmable control over liquid flow. Furthermore, we fabricated two diagnostic devices which can give colorimetric response in the presence of HSA. We believe that this high throughput, low cost and simple method can be used in designing disposable microfluidic devices for early stage diagnosis and point-of-care analysis, as well as proving to be a novel fabrication scheme for further possibilities that require tuning of liquid behavior on large-areas and flexible systems.

Consequently, we demonstrated simple fabrication of rice leaf-like anisotropic non-wetting surfaces using surface textured polymer fibers. A high throughput and inexpensive thermal drawing method was applied to produce several meters long fibers with perfectly aligned parallel microscale triangular grooves. Fiber pieces of varying lengths were fixed on substrates using double sided tape to realize anisotropic surfaces.

Nanoscale random roughness was added to the ordered microscale topography of the surfaces by spray coating a hydrophobic nanoparticle solution. The anisotropic wetting/non-wetting characteristics of the surfaces were investigated with contact and roll-off angle measurements in both parallel and perpendicular directions to the fibers' orientation. On the nanoparticle coated fiber surfaces, the very ordered microscale roughness of the fibers introduce anisotropy, whereas the nanoscale random roughness ensures the non-wetting. We then, investigated the chemistry of UV/Ozone treated surfaces and apply this technique to modify multiscale rough fiber. We have confirmed the chemical contribution of a surface to wetting. The relation between surface structure and surface chemistry was reported in this work. By the use of the hierarchically structured polymer fibers as building blocks to prepare several track designs, we showed the promising potential of the surface textured fibers for droplet transportation, mixing, guiding, and droplet based chemical reactions. We believe that this research could pave the way for promising potential applications such as directional self-cleaning surfaces, droplet microfluidics, fog collection, droplet transport, droplet mixing, and non-wetting textiles.

6.2. Future Work

Capillary wicking was shown to be the driving force to spread liquid on the fibers. It was demonstrated that the V – grooved fibers can be used for anisotropic manipulation of fluid in microchannel after surface modification. However, the grooves are open to the atmospheric environment where evaporation of fluid is a concern. To eliminate this effect, instead of grooving the fiber from its surface, microgrooves can be inscribed in the hollow core of the fiber preform. With this approach, fiber based closed-channel microfluidics that transport fluid internally can be achieved and the evaporation effect would be eliminated. Furthermore, a governing equation which includes gravity and evaporation effects can be modelled for the V – grooved fiber.

In addition, hierarchical V - grooved polycarbonate fibers with three scale of roughness is obtainable as shown in chapter 5. It is believed that with optimal design,

the grooved fibers can be used for superhydrophobic surfaces with intrinsic contact angle greater $> 150^\circ$. On the other hand, when modified by UV/Ozone the hierarchical structured fibers can be used for DNA hybridization and cell trapping assay. In terms of microfluidics design, the hierarchical fiber can be more effective for close-channel fiber application than the single scale grooved fibers. Multiplexing using V – groove compartment can be realized to deliver different solution through the fiber hollow core. Closed-channel grooved fibers can be integrated in designing better microfluidic devices that benefit from capillary wicking.

Bibliography

- [1] G. S. Fiorini and D. T. Chiu, “Disposable microfluidic devices: Fabrication, function, and application,” *BioTechniques*, vol. 38, no. 3. pp. 429–446, 2005.
- [2] S. K. Sia and G. M. Whitesides, “Microfluidic devices fabricated in poly(dimethylsiloxane) for biological studies,” *Electrophoresis*, vol. 24, no. 21, pp. 3563–3576, 2003.
- [3] M. J. Jebrail, M. S. Bartsch, and K. D. Patel, “Digital microfluidics: a versatile tool for applications in chemistry, biology and medicine,” *Lab Chip*, vol. 12, no. 14, p. 2452, 2012.
- [4] D. R. Meldrum and M. R. Holl, “Microscale bioanalytical systems,” *Science (80-.)*, vol. 297, no. 5584, pp. 1197–1198, 2002.
- [5] S.-Y. Teh, R. Lin, L.-H. Hung, and A. P. Lee, “Droplet microfluidics,” *Lab Chip*, vol. 8, no. 2, pp. 198–220, 2008.
- [6] P. Tabeling, “A brief introduction to slippage, droplets and mixing in microfluidic systems,” *Lab Chip*, vol. 9, no. 17, pp. 2428–2436, 2009.
- [7] D. B. Weibel and G. M. Whitesides, “Applications of microfluidics in chemical biology,” *Curr. Opin. Chem. Biol.*, vol. 10, no. 6, pp. 584–91, 2006.
- [8] G. M. Whitesides, “The origins and the future of microfluidics,” *Nature*, vol. 442, no. 7101, pp. 368–73, 2006.
- [9] E. K. Sackmann, A. L. Fulton, and D. J. Beebe, “The present and future role of microfluidics in biomedical research,” *Nature*, vol. 507, no. 7491, pp. 181–189, 2014.
- [10] F. Qian, M. Baum, Q. Gu, and D. E. Morse, “A 1.5 μ l microbial fuel cell for on-chip bioelectricity generation,” *Lab a Chip - Miniaturisation Chem. Biol.*, vol. 9, no. 21, pp. 3076–3081, 2009.
- [11] S. W. Dutse and N. A. Yusof, “Microfluidics-based lab-on-chip systems in

- DNA-based biosensing: an overview.,” *Sensors (Basel)*, vol. 11, no. 6, pp. 5754–68, 2011.
- [12] D. J. Beebe, G. a Mensing, and G. M. Walker, “Physics and applications of microfluidics in biology.,” *Annu. Rev. Biomed. Eng.*, vol. 4, pp. 261–286, 2002.
- [13] C. W. Yung, J. Fiering, A. J. Mueller, and D. E. Ingber, “Micromagnetic-microfluidic blood cleansing device.,” *Lab Chip*, vol. 9, no. 9, pp. 1171–1177, 2009.
- [14] D. Wlodkowic and J. M. Cooper, “Tumors on chips: oncology meets microfluidics.,” *Curr. Opin. Chem. Biol.*, vol. 14, no. 5, pp. 556–67, 2010.
- [15] R. Fan, O. Vermesh, A. Srivastava, B. K. H. Yen, L. Qin, H. Ahmad, G. A. Kwong, C.-C. Liu, J. Gould, L. Hood, and J. R. Heath, “Integrated barcode chips for rapid, multiplexed analysis of proteins in microliter quantities of blood,” *Nat. Biotechnol.*, vol. 26, no. 12, pp. 1373–1378, 2008.
- [16] M. A. Burns, “Analytic chemistry. Everyone’s a (future) chemist.,” *Science*, vol. 296, no. 5574, pp. 1818–9, 2002.
- [17] D. Chen, W. Du, Y. Liu, W. Liu, A. Kuznetsov, F. E. Mendez, L. H. Philipson, and R. F. Ismagilov, “The chemistode: a droplet-based microfluidic device for stimulation and recording with high temporal, spatial, and chemical resolution.,” *Proc. Natl. Acad. Sci. U. S. A.*, vol. 105, no. 44, pp. 16843–16848, 2008.
- [18] R. W. Doebler, B. Erwin, A. Hickerson, B. Irvine, D. Woyski, A. Nadim, and J. D. Sterling, “Continuous-Flow, Rapid Lysis Devices for Biodefense Nucleic Acid Diagnostic Systems,” *JALA - J. Assoc. Lab. Autom.*, vol. 14, no. 3, pp. 119–125, 2009.
- [19] S. Köster, F. E. Angilè, H. Duan, J. J. Agresti, A. Wintner, C. Schmitz, A. C. Rowat, C. a Merten, D. Pisignano, A. D. Griffiths, and D. a Weitz, “Drop-based microfluidic devices for encapsulation of single cells.,” *Lab Chip*, vol. 8, no. 7, pp. 1110–1115, 2008.

- [20] R. S. Ramsey and J. M. Ramsey, "Generating Electrospray from Microchip Devices Using Electroosmotic Pumping," *Anal. Chem.*, vol. 69, no. 6, pp. 1174–1178, 1997.
- [21] A. B. Theberge, F. Courtois, Y. Schaerli, M. Fischlechner, C. Abell, F. Hollfelder, and W. T. S. Huck, "Microdroplets in microfluidics: An evolving platform for discoveries in chemistry and biology," *Angew. Chemie - Int. Ed.*, vol. 49, no. 34, pp. 5846–5868, 2010.
- [22] B. F. Cottam, S. Krishnadasan, a J. deMello, J. C. deMello, and M. S. P. Shaffer, "Accelerated synthesis of titanium oxide nanostructures using microfluidic chips," *Lab Chip*, vol. 7, no. 2, pp. 167–169, 2007.
- [23] Y. Hennequin, N. Pannacci, C. P. De Torres, G. Tetradis-Meris, S. Chapuliot, E. Bouchaud, and P. Tabeling, "Synthesizing microcapsules with controlled geometrical and mechanical properties with microfluidic double emulsion technology," *Langmuir*, vol. 25, no. 14, pp. 7857–7861, 2009.
- [24] J. L. Lubbeck, K. M. Dean, H. Ma, A. E. Palmer, and R. Jimenez, "Microfluidic flow cytometer for quantifying photobleaching of fluorescent proteins in cells," *Anal. Chem.*, vol. 84, no. 9, pp. 3929–3937, 2012.
- [25] S. Marre and K. F. Jensen, "Synthesis of micro and nanostructures in microfluidic systems.," *Chem. Soc. Rev.*, vol. 39, no. 3, pp. 1183–1202, 2010.
- [26] Y. Wang, W.-Y. Lin, K. Liu, R. J. Lin, M. Selke, H. C. Kolb, N. Zhang, X.-Z. Zhao, M. E. Phelps, C. K. F. Shen, K. F. Faull, and H.-R. Tseng, "An integrated microfluidic device for large-scale in situ click chemistry screening.," *Lab Chip*, vol. 9, no. 16, pp. 2281–2285, 2009.
- [27] J. Yue, J. C. Schouten, and T. Alexander Nijhuis, "Integration of microreactors with spectroscopic detection for online reaction monitoring and catalyst characterization," *Ind. Eng. Chem. Res.*, vol. 51, no. 45, pp. 14583–14609, 2012.
- [28] D. Mijatovic, J. C. T. Eijkel, and a van den Berg, "Technologies for nanofluidic

- systems: top-down vs. bottom-up--a review.," *Lab Chip*, vol. 5, no. 5, pp. 492–500, 2005.
- [29] D. a. Czaplewski, J. Kameoka, R. Mathers, G. W. Coates, and H. G. Craighead, "Nanofluidic channels with elliptical cross sections formed using a nonlithographic process," *Appl. Phys. Lett.*, vol. 83, no. 23, p. 4836, 2003.
- [30] A. W. Martinez, S. T. Phillips, M. J. Butte, and G. M. Whitesides, "Patterned paper as a platform for inexpensive, low-volume, portable bioassays," *Angew. Chemie - Int. Ed.*, vol. 46, no. 8, pp. 1318–1320, 2007.
- [31] A. W. Martinez, S. T. Phillips, E. Carrilho, S. W. Thomas III, G. M. Whitesides, S. W. T. Iii, and G. M. Whitesides, "Simple Telemedicine for Developing Regions: Camera Phones and Paper-Based Microfluidic Devices for Real-Time, Off-Site Diagnosis," *Anal. Chem.*, vol. 80, no. 10, pp. 3699–3707, 2008.
- [32] R. Lu, W. Shi, L. Jiang, J. Qin, and B. Lin, "Rapid prototyping of paper-based microfluidics with wax for low-cost, portable bioassay," *Electrophoresis*, vol. 30, no. 9, pp. 1497–1500, 2009.
- [33] A. W. Martinez, S. T. Phillips, Z. Nie, C.-M. Cheng, E. Carrilho, B. J. Wiley, and G. M. Whitesides, "Programmable diagnostic devices made from paper and tape.," *Lab Chip*, vol. 10, no. 19, pp. 2499–504, 2010.
- [34] X. Li, J. Tian, G. Garnier, and W. Shen, "Fabrication of paper-based microfluidic sensors by printing," *Colloids Surfaces B Biointerfaces*, vol. 76, no. 2, pp. 564–570, 2010.
- [35] H. Liu and R. M. Crooks, "Three-dimensional paper microfluidic devices assembled using the principles of origami," *J. Am. Chem. Soc.*, vol. 133, no. 44, pp. 17564–17566, 2011.
- [36] A. W. Martinez, S. T. Phillips, and G. M. Whitesides, "Three-dimensional microfluidic devices fabricated in layered paper and tape.," *Proc. Natl. Acad. Sci. U. S. A.*, vol. 105, no. 50, pp. 19606–19611, 2008.

- [37] G. G. Lewis, M. J. Ditucci, and S. T. Phillips, “Quantifying analytes in paper-based microfluidic devices without using external electronic readers,” *Angew. Chemie - Int. Ed.*, vol. 51, no. 51, pp. 12707–12710, 2012.
- [38] S. T. Phillips and G. G. Lewis, “Advances in materials that enable quantitative point-of-care assays,” *MRS Bull.*, vol. 38, no. 04, pp. 315–319, 2013.
- [39] M. Bayindir, F. Sorin, A. F. Abouraddy, J. Viens, S. D. Hart, J. D. Joannopoulos, and Y. Fink, “Metal-insulator-semiconductor optoelectronic fibres,” *Nature*, vol. 431, no. 7010, pp. 826–9, 2004.
- [40] a F. Abouraddy, M. Bayindir, G. Benoit, S. D. Hart, K. Kuriki, N. Orf, O. Shapira, F. Sorin, B. Temelkuran, and Y. Fink, “Towards multimaterial multifunctional fibres that see, hear, sense and communicate,” *Nat. Mater.*, vol. 6, no. 5, pp. 336–347, 2007.
- [41] M. Yaman, T. Khudiyev, E. Ozgur, M. Kanik, O. Aktas, E. O. Ozgur, H. Deniz, E. Korkut, and M. Bayindir, “Arrays of indefinitely long uniform nanowires and nanotubes,” *Nat. Mater.*, vol. 10, no. 7, pp. 494–501, 2011.
- [42] A. Yildirim, M. Vural, M. Yaman, and M. Bayindir, “Bioinspired optoelectronic nose with nanostructured wavelength-scalable hollow-core infrared fibers,” *Adv. Mater.*, vol. 23, pp. 1263–1267, 2011.
- [43] X. Li, J. Tian, and W. Shen, “Thread as a versatile material for low-cost microfluidic diagnostics,” *ACS Appl. Mater. Interfaces*, vol. 2, no. 1, pp. 1–6, 2010.
- [44] F. Vatansever, R. Burtovyy, B. Zdyrko, K. Ramaratnam, T. Andruk, S. Minko, J. R. Owens, K. G. Kornev, and I. Luzinov, “Toward fabric-based flexible microfluidic devices: Pointed surface modification for pH sensitive liquid transport,” *ACS Appl. Mater. Interfaces*, vol. 4, no. 9, pp. 4541–4548, 2012.
- [45] P. Bhandari, T. Narahari, and D. Dendukuri, “‘Fab-chips’: a versatile, fabric-based platform for low-cost, rapid and multiplexed diagnostics,” *Lab Chip*, vol. 11, no. 15, pp. 2493–2499, 2011.

- [46] R. Safaviieh, G. Z. Zhou, and D. Juncker, “Microfluidics made of yarns and knots: from fundamental properties to simple networks and operations.,” *Lab Chip*, vol. 11, no. 15, pp. 2618–2624, 2011.
- [47] Q. F. Xu, J. N. Wang, I. H. Smith, and K. D. Sanderson, “Directing the transportation of a water droplet on a patterned superhydrophobic surface,” *Appl. Phys. Lett.*, vol. 93, no. 23, pp. 2006–2009, 2008.
- [48] H. Mertaniemi, V. Jokinen, L. Sainiemi, S. Franssila, A. Marmur, O. Ikkala, and R. H. a Ras, “Superhydrophobic tracks for low-friction, guided transport of water droplets,” *Adv. Mater.*, vol. 23, pp. 2911–2914, 2011.
- [49] H. Mertaniemi, R. Forchheimer, O. Ikkala, and R. H. a Ras, “Rebounding droplet-droplet collisions on superhydrophobic surfaces: From the phenomenon to droplet logic,” *Adv. Mater.*, vol. 24, no. 42, pp. 5738–5743, 2012.
- [50] X. Yao, Y. Song, and L. Jiang, “Applications of Bio-Inspired Special Wettable Surfaces,” *Adv. Mater.*, vol. 23, no. 6, pp. 719–734, 2011.
- [51] D. J. Harrison, A. Manz, Z. Fan, H. Luedi, and H. M. Widmer, “Capillary electrophoresis and sample injection systems integrated on a planar glass chip,” *Anal. Chem.*, vol. 64, no. 20, pp. 1926–1932, 1992.
- [52] A. Manz, D. J. Harrison, E. M. J. Verpoorte, J. C. Fettinger, A. Paulus, H. Lüdi, and H. M. Widmer, “Planar chips technology for miniaturization and integration of separation techniques into monitoring systemsCapillary electrophoresis on a chip,” *J. Chromatogr. A*, vol. 593, no. 1–2, pp. 253–258, 1992.
- [53] I. Rodriguez, P. Spicar-Mihalic, C. L. Kuyper, G. S. Fiorini, and D. T. Chiu, “Rapid prototyping of glass microchannels,” *Anal. Chim. Acta*, vol. 496, no. 1–2, pp. 205–215, 2003.
- [54] J. Narasimhan and I. Papautsky, “Rapid fabrication of hot embossing tools using PDMS,” ..., vol. 4982, no. 513, pp. 110–119, 2003.
- [55] Z.-C. Peng, “Interconnected multilevel microfluidic channels fabricated using

- low-temperature bonding of SU-8 and multilayer lithography,” *Proc. SPIE*, vol. 5718, pp. 209–215, 2005.
- [56] M. E. Sandison and H. Morgan, “Rapid fabrication of polymer microfluidic systems for the production of artificial lipid bilayers,” *J. Micromechanics Microengineering*, vol. 15, no. 7, pp. S139–S144, 2005.
- [57] G. M. Whitesides, E. Ostuni, S. Takayama, X. Jiang, and D. E. Ingber, “Soft lithography in biology and biochemistry.,” *Annu. Rev. Biomed. Eng.*, vol. 3, pp. 335–373, 2001.
- [58] J. R. Anderson, D. T. Chiu, R. J. Jackman, O. Chemiavskaya, J. C. McDonald, H. Wu, S. H. Whitesides, and G. M. Whitesides, “Fabrication of topologically complex three-dimensional microfluidic systems in PDMS by rapid prototyping,” *Anal. Chem.*, vol. 72, no. 14, pp. 3158–3164, 2000.
- [59] B. H. Jo, L. M. Van Lerberghe, K. M. Motsegood, and D. J. Beebe, “Three-dimensional micro-channel fabrication in polydimethylsiloxane (PDMS) elastomer,” *J. Microelectromechanical Syst.*, vol. 9, no. 1, pp. 76–81, 2000.
- [60] D. C. Duffy, J. C. McDonald, O. J. a Schueller, and G. M. Whitesides, “Rapid prototyping of microfluidic systems in poly(dimethylsiloxane),” *Anal. Chem.*, vol. 70, no. 23, pp. 4974–4984, 1998.
- [61] J. C. McDonald, D. C. Duffy, J. R. Anderson, D. T. Chiu, H. Wu, O. J. Schueller, and G. M. Whitesides, “Fabrication of microfluidic systems in poly(dimethylsiloxane).,” *Electrophoresis*, vol. 21, no. 1, pp. 27–40, 2000.
- [62] J. C. McDonald and G. M. Whitesides, “Poly (dimethylsiloxane) as a Material for Fabricating Microfluidic Devices,” *Acc. Chem. Res.*, vol. 35, no. 7, pp. 491–499, 2002.
- [63] a Folch and M. Toner, “Microengineering of cellular interactions.,” *Annu. Rev. Biomed. Eng.*, vol. 2, pp. 227–256, 2000.
- [64] M. a Unger, H. P. Chou, T. Thorsen, a Scherer, and S. R. Quake, “Monolithic

- microfabricated valves and pumps by multilayer soft lithography.,” *Science*, vol. 288, no. 5463, pp. 113–116, 2000.
- [65] R. F. Ismagilov, D. Rosmarin, P. J. a Kenis, D. T. Chiu, W. Zhang, H. a. Stone, and G. M. Whitesides, “Pressure-driven laminar flow in tangential microchannels: An elastomeric microfluidic switch,” *Anal. Chem.*, vol. 73, no. 19, pp. 4682–4687, 2001.
- [66] N. L. Jeon, D. T. Chiu, C. J. Wargo, H. Wu, I. S. Choi, J. R. Anderson, and G. M. Whitesides, “Design and fabrication of integrated passive valves and pumps for flexible polymer 3-dimensional microfluidic systems,” *Biomed. Microdevices*, vol. 4, no. 2, pp. 117–121, 2002.
- [67] J. N. Lee, C. Park, and G. M. Whitesides, “Solvent Compatibility of Poly(dimethylsiloxane)-Based Microfluidic Devices,” *Anal. Chem.*, vol. 75, no. 23, pp. 6544–6554, 2003.
- [68] V. Liimatainen, V. Sariola, and Q. Zhou, “Controlling liquid spreading using microfabricated undercut edges,” *Adv. Mater.*, vol. 25, pp. 2275–2278, 2013.
- [69] J. P. Rolland, R. M. Van Dam, D. a Schorzman, S. R. Quake, and J. M. DeSimone, “Solvent-resistant photocurable liquid fluoropolymers for microfluidic device fabrication [corrected].,” *J. Am. Chem. Soc.*, vol. 126, pp. 2322–2323, 2004.
- [70] N. a Malvadkar, M. J. Hancock, K. Sekeroglu, W. J. Dressick, and M. C. Demirel, “An engineered anisotropic nanofilm with unidirectional wetting properties,” *Nat. Mater.*, vol. 9, no. 12, pp. 1023–8, 2010.
- [71] H. Gau, “Liquid Morphologies on Structured Surfaces: From Microchannels to Microchips,” *Science (80-.)*, vol. 283, no. 5398, pp. 46–49, 1999.
- [72] B. Zhao, J. S. Moore, and D. J. Beebe, “Surface-directed liquid flow inside microchannels,” *Science*, vol. 291, no. 5506, pp. 1023–1026, 2001.
- [73] M. Morita, T. Koga, H. Otsuka, and A. Takahara, “Macroscopic-wetting

- anisotropy on the line-patterned surface of fluoroalkylsilane monolayers,” *Langmuir*, vol. 21, no. 3, pp. 911–918, 2005.
- [74] R. N. Wenzel, “Resistance of solid surfaces to wetting by water.,” *J. Ind. Eng. Chem. (Washington, D. C.)*, vol. 28, pp. 988–994, 1936.
- [75] A. B. D. Cassie and S. Baxter, “Wettability of porous surfaces,” *Transactions of the Faraday Society*, vol. 40, no. 5. p. 546, 1944.
- [76] R. Blossey, “Self-cleaning surfaces--virtual realities.,” *Nat. Mater.*, vol. 2, pp. 301–306, 2003.
- [77] K. Koch and W. Barthlott, “Superhydrophobic and superhydrophilic plant surfaces: an inspiration for biomimetic materials.,” *Philos. Trans. A. Math. Phys. Eng. Sci.*, vol. 367, no. 1893, pp. 1487–509, 2009.
- [78] W. Song, D. D. Veiga, C. a. Custódio, and J. F. Mano, “Bioinspired degradable substrates with extreme wettability properties,” *Adv. Mater.*, vol. 21, no. 18, pp. 1830–1834, 2009.
- [79] C. Dorrer and J. Rühle, “Wetting of silicon nanograss: From superhydrophilic to superhydrophobic surfaces,” *Adv. Mater.*, vol. 20, no. 1, pp. 159–163, 2008.
- [80] A. Lee, M. W. Moon, H. Lim, W. D. Kim, and H. Y. Kim, “Water harvest via dewing,” *Langmuir*, vol. 28, pp. 10183–10191, 2012.
- [81] W. Zhong, S. Liu, X. Chen, Y. Wang, and W. Yang, “High-Yield Synthesis of Superhydrophilic Polypyrrole Nanowire Networks,” *Macromolecules*, vol. 39, no. 9, pp. 3224–3230, 2006.
- [82] J. Zhang and S. Seeger, “Superoleophobic coatings with ultralow sliding angles based on silicone nanofilaments,” *Angew. Chemie - Int. Ed.*, vol. 50, no. 29, pp. 6652–6656, 2011.
- [83] D. Xia, L. M. Johnson, and G. P. López, “Anisotropic wetting surfaces with one-dimensional and directional structures: Fabrication approaches, wetting properties and potential applications,” *Adv. Mater.*, vol. 24, no. 10, pp. 1287–

1302, 2012.

- [84] Y. Zheng, X. Gao, and L. Jiang, "Directional adhesion of superhydrophobic butterfly wings," *Soft Matter*, vol. 3, no. 2, p. 178, 2007.
- [85] X. Gao, X. Yan, X. Yao, L. Xu, K. Zhang, J. Zhang, B. Yang, and L. Jiang, "The dry-style antifogging properties of mosquito compound eyes and artificial analogues prepared by soft lithography," *Adv. Mater.*, vol. 19, no. 17, pp. 2213–2217, 2007.
- [86] L. Zhai, M. C. Berg, F. Ç. Cebeci, Y. Kim, J. M. Milwid, M. F. Rubner, and R. E. Cohen, "Patterned superhydrophobic surfaces: Toward a synthetic mimic of the namib desert beetle," *Nano Lett.*, vol. 6, no. 6, pp. 1213–1217, 2006.
- [87] K. Liu, X. Yao, and L. Jiang, "Recent developments in bio-inspired special wettability.," *Chem. Soc. Rev.*, vol. 39, no. 8, pp. 3240–55, 2010.
- [88] M. Callies and D. Quéré, "On water repellency," *Soft Matter*, vol. 1, no. 1, p. 55, 2005.
- [89] D. Öner and T. J. McCarthy, "Ultrahydrophobic surfaces. Effects of topography length scales on wettability," *Langmuir*, vol. 16, no. 20, pp. 7777–7782, 2000.
- [90] L. Gao and T. J. McCarthy, "How Wenzel and Cassie were wrong," *Langmuir*, vol. 23, no. 7, pp. 3762–3765, 2007.
- [91] E. Ueda and P. a. Levkin, "Emerging applications of superhydrophilic-superhydrophobic micropatterns," *Adv. Mater.*, vol. 25, pp. 1234–1247, 2013.
- [92] X. Jiang, Q. Xu, S. K. W. Dertinger, A. D. Stroock, T.-M. Fu, and G. M. Whitesides, "A general method for patterning gradients of biomolecules on surfaces using microfluidic networks.," *Anal. Chem.*, vol. 77, no. 8, pp. 2338–47, 2005.
- [93] H. Wu, B. Huang, and R. N. Zare, "Generation of complex, static solution gradients in microfluidic channels," *J. Am. Chem. Soc.*, vol. 128, no. 13, pp. 4194–4195, 2006.

- [94] H. Lu, L. Y. Koo, W. M. Wang, D. a. Lauffenburger, L. G. Griffith, and K. F. Jensen, "Microfluidic shear devices for quantitative analysis of cell adhesion," *Anal. Chem.*, vol. 76, no. 18, pp. 5257–5264, 2004.
- [95] M. a McClain, C. T. Culbertson, S. C. Jacobson, N. L. Allbritton, C. E. Sims, and J. M. Ramsey, "Microfluidic devices for the high-throughput chemical analysis of cells.," *Anal. Chem.*, vol. 75, no. 21, pp. 5646–55, 2003.
- [96] D. E. Kataoka and S. M. Troian, "Patterning liquid flow on the microscopic scale," *Nature*, vol. 402, no. 6763, pp. 794–797, 1999.
- [97] B. Zhao, J. S. Moore, and D. J. Beebe, "Pressure-sensitive microfluidic gates fabricated by patterning surface free energies inside microchannels," *Langmuir*, vol. 19, no. 5, pp. 1873–1879, 2003.
- [98] D. Juncker, H. Schmid, U. Drechsler, H. Wolf, M. Wolf, B. Michel, N. De Rooij, and E. Delamarche, "Autonomous microfluidic capillary system," *Anal. Chem.*, vol. 74, no. 24, pp. 6139–6144, 2002.
- [99] B. S. Gallardo, "Electrochemical Principles for Active Control of Liquids on Submillimeter Scales," *Science (80-.)*, vol. 283, no. 5398, pp. 57–60, 1999.
- [100] J. El-Ali, P. K. Sorger, and K. F. Jensen, "Cells on chips.," *Nature*, vol. 442, no. 7101, pp. 403–411, 2006.
- [101] J. P. Landers, "Molecular diagnostics on electrophoretic microchips," *Anal. Chem.*, vol. 75, pp. 2919–2927, 2003.
- [102] E. Verpoorte, "Microfluidic chips for clinical and forensic analysis," *Electrophoresis*, vol. 23, no. 5, pp. 677–712, 2002.
- [103] W. T. Hofgartner, A. F. R. Huhmer, J. P. Landers, and J. A. Kant, "Rapid diagnosis of herpes simplex encephalitis using microchip electrophoresis of PCR products," *Clin. Chem.*, vol. 45, no. 12, pp. 2120–2128, 1999.
- [104] P. Wilding, M. a. Shoffner, and L. J. Kricka, "PCR in a silicon microstructure," *Clin. Chem.*, vol. 40, no. 9, pp. 1815–1818, 1994.

- [105] M. U. Kopp, a J. Mello, and a Manz, “Chemical amplification: continuous-flow PCR on a chip.,” *Science*, vol. 280, no. 5366, pp. 1046–1048, 1998.
- [106] M. a Burns, B. N. Johnson, S. N. Brahmasandra, K. Handique, J. R. Webster, M. Krishnan, T. S. Sammarco, P. M. Man, D. Jones, D. Heldsinger, C. H. Mastrangelo, and D. T. Burke, “An integrated nanoliter DNA analysis device.,” *Science*, vol. 282, no. 5388, pp. 484–487, 1998.
- [107] L. C. Waters, S. C. Jacobson, N. Kroutchinina, J. Khandurina, R. S. Foote, and J. M. Ramsey, “Microchip device for cell lysis, multiplex PCR amplification, and electrophoretic sizing.,” *Anal. Chem.*, vol. 70, no. 1, pp. 158–162, 1998.
- [108] P. K. Yuen, L. J. Kricka, P. Fortina, N. J. Panaro, T. Sakazume, and P. Wilding, “Microchip module for blood sample preparation and nucleic acid amplification reactions,” *Genome Res*, vol. 11, no. 3, pp. 405–412, 2001.
- [109] R. H. Liu, J. Yang, R. Lenigk, J. Bonanno, and P. Grodzinski, “Self-Contained, Fully Integrated Biochip for Sample Preparation, Polymerase Chain Reaction Amplification, and DNA Microarray Detection,” *Anal. Chem.*, vol. 76, no. 7, pp. 1824–1831, 2004.
- [110] E. Delamarche, a Bernard, H. Schmid, B. Michel, and H. Biebuyck, “Patterned delivery of immunoglobulins to surfaces using microfluidic networks.,” *Science*, vol. 276, no. 5313, pp. 779–781, 1997.
- [111] D. T. Chiu, N. L. Jeon, S. Huang, R. S. Kane, C. J. Wargo, I. S. Choi, D. E. Ingber, and G. M. Whitesides, “Patterned deposition of cells and proteins onto surfaces by using three-dimensional microfluidic systems.,” *Proc. Natl. Acad. Sci. U. S. A.*, vol. 97, no. 6, pp. 2408–13, 2000.
- [112] A. Tourovskaia, T. Barber, B. T. Wickes, D. Hirdes, B. Grin, D. G. Castner, K. E. Healy, and A. Folch, “Micropatterns of chemisorbed cell adhesion-repellent films using oxygen plasma etching and elastomeric masks,” *Langmuir*, vol. 19, no. 11, pp. 4754–4764, 2003.
- [113] S. Takayama, E. Ostuni, P. LeDuc, K. Naruse, D. E. Ingber, and G. M.

- Whitesides, "Subcellular positioning of small molecules.," *Nature*, vol. 411, no. 6841, p. 1016, 2001.
- [114] A. Sawano, S. Takayama, M. Matsuda, and A. Miyawaki, "Lateral Propagation of EGF Signaling after Local Stimulation Is Dependent on Receptor Density," *Dev. Cell*, vol. 3, no. 2, pp. 245–257, 2002.
- [115] A. R. Wheeler, W. R. Throdsset, R. J. Whelan, A. M. Leach, R. N. Zare, Y. H. Liao, K. Farrell, I. D. Manger, and A. Daridon, "Microfluidic device for single-cell analysis," *Anal. Chem.*, vol. 75, no. 14, pp. 3581–3586, 2003.
- [116] J. Atencia and D. J. Beebe, "Controlled microfluidic interfaces.," *Nature*, vol. 437, no. 7059, pp. 648–655, 2005.
- [117] B. P. Casavant, E. Berthier, A. B. Theberge, J. Berthier, S. I. Montanez-Sauri, L. L. Bischel, K. Brakke, C. J. Hedman, W. Bushman, N. P. Keller, and D. J. Beebe, "Suspended microfluidics.," *Proc. Natl. Acad. Sci.*, vol. 110, no. 25, pp. 10111–10116, 2013.
- [118] T. a. Duncombe, E. Y. Erdem, A. Shastry, R. Baskaran, and K. F. Böhringer, "Controlling liquid drops with texture ratchets," *Adv. Mater.*, vol. 24, no. 12, pp. 1545–1550, 2012.
- [119] S. H. Lee, A. J. Helnz, S. Shln, Y. G. Jung, S. E. Chol, W. Park, J. H. Roe, and S. Kwon, "Capillary based patterning of cellular communities in laterally open channels," *Anal. Chem.*, vol. 82, no. 7, pp. 2900–2906, 2010.
- [120] M. Hitzbleck, R. D. Lovchik, and E. Delamarche, "Flock-based microfluidics.," *Adv. Mater.*, vol. 25, no. 19, pp. 2672–2676, 2013.
- [121] R. Seemann, M. Brinkmann, E. J. Kramer, F. F. Lange, and R. Lipowsky, "Wetting morphologies at microstructured surfaces.," *Proc. Natl. Acad. Sci. U. S. A.*, vol. 102, no. 6, pp. 1848–1852, 2005.
- [122] D. Xia and S. R. J. Brueck, "Strongly anisotropic wetting on one-dimensional nanopatterned surfaces.," *Nano Lett.*, vol. 8, no. 9, pp. 2819–24, 2008.

- [123] J. Y. Chung, J. P. Youngblood, and C. M. Stafford, “Anisotropic wetting on tunable micro-wrinkled surfaces,” *Soft Matter*, vol. 3, no. 9, p. 1163, 2007.
- [124] V. Jokinen, M. Leinikka, and S. Franssila, “Microstructured Surfaces for Directional Wetting,” *Adv. Mater.*, vol. 21, no. 47, pp. 4835–4838, Dec. 2009.
- [125] K. Tsougeni, D. Papageorgiou, A. Tserepi, and E. Gogolides, “‘Smart’ polymeric microfluidics fabricated by plasma processing: controlled wetting, capillary filling and hydrophobic valving.,” *Lab Chip*, vol. 10, no. 4, pp. 462–469, 2010.
- [126] N. M. Oliveira, A. I. Neto, W. Song, and J. F. Mano, “Two-dimensional open microfluidic devices by tuning the wettability on patterned superhydrophobic polymeric surface,” *Appl. Phys. Express*, vol. 3, pp. 6–8, 2010.
- [127] H. Lee, S. M. Dellatore, W. M. Miller, and P. B. Messersmith, “Mussel-inspired surface chemistry for multifunctional coatings.,” *Science*, vol. 318, no. 5849, pp. 426–430, 2007.
- [128] N. F. Della Vecchia, R. Avolio, M. Alfe, M. E. Errico, A. Napolitano, and M. D’Ischia, “Building-Block Diversity in Polydopamine Underpins a Multifunctional Eumelanin-Type Platform Tunable Through a Quinone Control Point,” *Adv. Funct. Mater.*, vol. 23, no. 10, pp. 1331–1340, 2013.
- [129] T. S. Sileika, D. G. Barrett, R. Zhang, K. H. A. Lau, and P. B. Messersmith, “Colorless multifunctional coatings inspired by polyphenols found in tea, chocolate, and wine,” *Angew. Chemie - Int. Ed.*, vol. 52, no. 41, pp. 10766–10770, 2013.
- [130] R. a. Zangmeister, T. a. Morris, and M. J. Tarlov, “Characterization of polydopamine thin films deposited at short times by autoxidation of dopamine,” *Langmuir*, vol. 29, pp. 8619–8628, 2013.
- [131] D. R. Dreyer, D. J. Miller, B. D. Freeman, D. R. Paul, and C. W. Bielawski, “Elucidating the Structure of Poly(dopamine),” *Langmuir*, vol. 28, no. 15, pp. 6428–6435, 2012.

- [132] J. Liebscher, R. Mrówczyński, H. a Scheidt, C. Filip, N. D. Hädade, R. Turcu, A. Bende, and S. Beck, “Structure of polydopamine: a never-ending story?,” *Langmuir*, vol. 29, no. 33, pp. 10539–48, 2013.
- [133] P. B. Warren, “Late stage kinetics for various wicking and spreading problems,” *Phys. Rev. E*, vol. 69, no. 4, p. 041601, 2004.
- [134] J. A. Mann Jr, L. Romero, R. R. Rye, and F. G. Yost, “Flow of simple liquids down narrow ssV grooves,” *Phys. Rev. E*, vol. 52, no. 4, pp. 3967–3972, 1995.
- [135] J. Tian, D. Kannangara, X. Li, and W. Shen, “Capillary driven low-cost V-groove microfluidic device with high sample transport efficiency.,” *Lab Chip*, vol. 10, no. 17, pp. 2258–64, 2010.
- [136] E. W. Washburn, “The dynamics of capillary flow,” *Phys. Rev.*, vol. 17, no. 3, pp. 273–283, 1921.
- [137] X. Gao and L. Jiang, “Biophysics: water-repellent legs of water striders.,” *Nature*, vol. 432, no. November, p. 36, 2004.
- [138] X. Q. Feng, X. Gao, Z. Wu, L. Jiang, and Q. S. Zheng, “Superior water repellency of water strider legs with hierarchical structures: Experiments and analysis,” *Langmuir*, vol. 23, no. 25, pp. 4892–4896, 2007.
- [139] D. Wu, J. N. Wang, S. Z. Wu, Q. D. Chen, S. Zhao, H. Zhang, H. B. Sun, and L. Jiang, “Three-level biomimetic rice-leaf surfaces with controllable anisotropic sliding,” *Adv. Funct. Mater.*, vol. 21, no. 15, pp. 2927–2932, 2011.
- [140] S. G. Lee, H. S. Lim, D. Y. Lee, D. Kwak, and K. Cho, “Tunable Anisotropic Wettability of Rice Leaf-Like Wavy Surfaces,” *Adv. Funct. Mater.*, vol. 23, no. 5, pp. 547–553, Feb. 2013.
- [141] E. Bittoun and A. Marmur, “The role of multiscale roughness in the Lotus effect: is it essential for super-hydrophobicity?,” *Langmuir*, vol. 28, no. 39, pp. 13933–42, 2012.
- [142] S. M. Kang, C. Lee, H. N. Kim, B. J. Lee, J. E. Lee, M. K. Kwak, and K. Y.

- Suh, "Directional oil sliding surfaces with hierarchical anisotropic groove microstructures," *Adv. Mater.*, vol. 25, no. 40, pp. 5756–5761, 2013.
- [143] J. H. Lee, H. W. Ro, R. Huang, P. Lemaillet, T. A. Germer, C. L. Soles, and C. M. Stafford, "Anisotropic, hierarchical surface patterns via surface wrinkling of nanopatterned polymer films," *Nano Lett.*, vol. 12, no. 11, pp. 5995–5999, 2012.
- [144] F. Zhang and H. Y. Low, "Anisotropic wettability on imprinted hierarchical structures," *Langmuir*, vol. 23, no. 14, pp. 7793–7798, 2007.
- [145] D. Xia, X. He, Y. B. Jiang, G. P. Lopez, and S. R. J. Brueck, "Tailoring anisotropic wetting properties on submicrometer-scale periodic grooved surfaces," *Langmuir*, vol. 26, no. 7, pp. 2700–2706, 2010.
- [146] H. Wu, R. Zhang, Y. Sun, D. Lin, Z. Sun, W. Pan, and P. Downs, "Biomimetic nanofiber patterns with controlled wettability," *Soft Matter*, vol. 4, no. 12, p. 2429, 2008.
- [147] J. Yong, Q. Yang, F. Chen, D. Zhang, U. Farooq, G. Du, and X. Hou, "A simple way to achieve superhydrophobicity, controllable water adhesion, anisotropic sliding, and anisotropic wetting based on femtosecond-laser-induced line-patterned surfaces," *J. Mater. Chem. A*, vol. 2, p. 5499, 2014.
- [148] F. Chen, D. Zhang, Q. Yang, X. Wang, B. Dai, X. Li, X. Hao, Y. Ding, J. Si, and X. Hou, "Anisotropic wetting on microstrips surface fabricated by femtosecond laser," *Langmuir*, vol. 27, no. 1, pp. 359–365, 2011.
- [149] D. a. Boyd, A. R. Shields, J. Naciri, and F. S. Ligler, "Hydrodynamic shaping, polymerization, and subsequent modification of thiol click fibers," *ACS Appl. Mater. Interfaces*, vol. 5, no. 1, pp. 114–119, 2013.
- [150] D. a Boyd, A. R. Shields, P. B. Howell, and F. S. Ligler, "Design and fabrication of uniquely shaped thiol-ene microfibers using a two-stage hydrodynamic focusing design.," *Lab on a chip*, vol. 13, no. 15, pp. 3105–10, 2013.
- [151] A. Yildirim, M. Yunusa, F. E. Ozturk, M. Kanik, and M. Bayindir, "Surface

- textured polymer fibers for microfluidics,” *Adv. Funct. Mater.*, vol. 24, no. 29, pp. 4569–4576, 2014.
- [152] A. Yildirim, H. Budunoglu, M. Yaman, M. O. Guler, and M. Bayindir, “Template free preparation of nanoporous organically modified silica thin films on flexible substrates,” *J. Mater. Chem.*, vol. 21, no. 38, p. 14830, 2011.
- [153] M. Kanik, O. Aktas, H. S. Sen, E. Durgun, and M. Bayindir, “Spontaneous High Piezoelectricity in Poly (vinylidene fluoride) Nanoribbons Produced by Iterative Thermal Size Reduction Technique.,” *ACS Nano*, vol. 8, no. 9, pp. 9311–9323, 2014.
- [154] J. R. Vig, “UV/ozone cleaning of surfaces,” *J. Vac. Sci. Technol. A Vacuum, Surfaces, Film.*, vol. 3, no. 3, p. 1027, 1985.
- [155] J. M. Lannon, “Analysis of Polycarbonate (PC) by XPS,” *Surf. Sci. Spectra*, vol. 6, no. 2, p. 75, Apr. 1999.
- [156] C. Borcia, G. Borcia, and N. Dumitrascu, “Surface treatment of polymers by plasma and UV radiation,” *Rom. J. Phys.*, vol. 56, no. 1–2, pp. 224–232, 2011.
- [157] L. D. Tijjing, C. S. Kim, and J. A. E. K. Lim, “Enhanced Wetting and Adhesion of Polycarbonate By,” vol. 8, no. 4, pp. 1415–1421, 2013.
- [158] D. Subedi, R. Tyata, and D. Rimal, “Effect of uv-treatment on the wettability of polycarbonate,” ... *Univ. J. Sci. Eng. ...*, vol. 5, no. Ii, pp. 37–41, 2009.
- [159] N. Moussaif, C. Pagnouille, J. Riga, and R. Jérôme, “XPS analysis of the PC/PVDF interface modified by PMMA. Location of the PMMA at the interface,” *Polymer (Guildf)*, vol. 41, no. 9, pp. 3391–3394, 2000.
- [160] R. O. F. Verkuijlen, M. H. A. van Dongen, A. A. E. Stevens, J. van Geldrop, and J. P. C. Bernardis, “Surface modification of polycarbonate and polyethylene naphthalate foils by UV-ozone treatment and μ Plasma printing,” *Appl. Surf. Sci.*, vol. 290, pp. 381–387, 2014.
- [161] A. Bhurke, P. Askeland, and L. Drzal, “Surface Modification of Polycarbonate

- by Ultraviolet Radiation and Ozone,” *J. Adhes.*, vol. 83, no. 1, pp. 43–66, 2007.
- [162] K. Uosaki, M. E. Quayum, S. Nihonyanagi, and T. Kondo, “Decomposition Processes of an Organic Monolayer Formed on Si(111) via a SiliconCarbon Bond Induced by Exposure to UV Irradiation or Ozone,” *Langmuir*, vol. 20, no. 4, pp. 1207–1212, 2004.
- [163] A. Bhattacharyya and C. M. Klapperich, “Mechanical and chemical analysis of plasma and ultraviolet-ozone surface treatments for thermal bonding of polymeric microfluidic devices,” *Lab Chip*, vol. 7, no. 7, pp. 876–82, 2007.
- [164] Y. G. Lei, K. M. Ng, L. T. Weng, C. M. Chan, and L. Li, “XPS C 1s binding energies for fluorocarbon-hydrocarbon microblock copolymers,” *Surf. Interface Anal.*, vol. 35, no. 10, pp. 852–855, 2003.